4

METAMATERIAL TRANSMISSION LINES: RF/MICROWAVE APPLICATIONS

4.1 INTRODUCTION

This chapter is entirely focused on the RF/microwave applications of the artificial lines considered in Chapter 3, that is, composite right-/left-handed (CRLH) transmission lines, and also on the applications of transmission lines with metamaterial loading, that is, transmission lines loaded with electrically small resonators, formerly used for the implementation of effective media metamaterials.

The applications of CRLH transmission lines are mainly based on the controllability of the dispersion and characteristic impedance of the lines. Thus, impedance and dispersion engineering, which represents a genuine metamaterial-related design approach, allow us to implement RF/microwave devices with superior performance (as compared to devices based on ordinary lines and stubs), or with novel functionalities. Moreover, since the unit cells of metamaterial transmission lines are electrically small at the frequencies of interest, device dimensions can be made very small as compared to the typical sizes of ordinary distributed circuits. The implementation of dual-band and multiband devices, where the characteristic impedance and electrical length of the constitutive artificial lines must be set to certain values at the operating frequencies, is a clear application (among many others) where impedance and dispersion engineering apply. On the other hand, as anticipated in the introductory section of Chapter 3, the functionality of transmission lines with metamaterial loading is mainly based on particle resonance, rather than on dispersion and impedance engineering. Examples of applications of transmission lines with metamaterial loading are the multiband printed dipole and monopole antennas based on the concept of trap antennas, where

Artificial Transmission Lines for RF and Microwave Applications, First Edition. Ferran Martín.

the multiband functionality is achieved by loading the dipole, or the monopole, with SRRs or with other electrically small resonators.

The RF/microwave applications considered in this chapter are grouped into two categories: applications of CRLH transmission lines, mainly, although not exclusively, based on impedance and dispersion engineering, and applications of transmission lines with metamaterial loading. The reported applications of this chapter are necessarily influenced by the own experience of the author. Thus, most of these applications have been proposed by the author's Group, although there are many others proposed by other active researchers in the field. Nevertheless, it is impossible to cover all the applications of metamaterial transmission lines reported in the literature in a single chapter. Hence, many applications not considered here are quoted in the reference list. The author also recommends several reference books on the topic [1–6], as complementary and excellent lectures to the present book.

4.2 APPLICATIONS OF CRLH TRANSMISSION LINES

Dispersion and impedance engineering is a design process that consists of tailoring the dispersion and characteristic impedance of metamaterial transmission lines in order to achieve certain functionalities, which are normally not achievable by means of conventional lines. Dispersion and impedance engineering can be applied to the design of enhanced bandwidth components, multiband components, filters and diplexers, leaky wave antennas (LWAs), couplers, distributed amplifiers and mixers, and sensors, among others. Let us now study the principles behind these applications or the advantages of using CRLH lines and some illustrative results.

4.2.1 Enhanced Bandwidth Components

Metamaterial transmission lines can be applied to the design of microwave components with a broad operation bandwidth as compared to those bandwidths achievable in devices implemented by means of ordinary transmission lines and stubs. We will start this subsection by studying the principles behind bandwidth enhancement and by discussing their fundamental limitations, and then several enhanced bandwidth components will be reported as illustrative examples.

4.2.1.1 Principle and Limitations The operative bandwidth of microwave components is given by that frequency interval where the required characteristics are satisfied within certain limits. In distributed circuits, bandwidth is limited by the phase shift experienced by transmission lines and stubs when frequency is varied from the nominal operating value. In a conventional transmission line of length l, the electrical length, or phase shift,[1] of the line at a certain angular frequency ω_o is given by

[1] In this discussion, by phase shift we refer to the electrical length of the line, and hence it has the same sign as the phase constant β. The phase shift is thus positive for ordinary lines, and it is negative/positive in the left/right handed transmission bands of CRLH metamaterial transmission lines.

$$\phi_o = \beta l = \frac{l}{v_p}\omega_o \tag{4.1}$$

where v_p is the phase velocity of the line. According to the previous comment, bandwidth is intimately related to the derivative of ϕ with frequency, also known as group delay. From this, it follows that the shorter the line is, the broader the bandwidth becomes. In other words, bandwidth is inversely proportional to the required phase of the line, which is dictated by the design. This means that the operative bandwidth is not an easily controllable parameter in conventional distributed circuits.[2] The reason is the limited number of degrees of freedom of conventional transmission lines. However, in metamaterial transmission lines, the loading elements provide additional parameters, and certain control over the phase response is possible. Namely, one expects that the required phase does not dictate the bandwidth. The key question is: Is it possible to improve the bandwidth (or decrease the group delay) of conventional lines by means of metamaterial transmission lines regardless of the required phase shift? Let us discuss now this aspect (a detailed analysis is given in Ref. [7]).

Assuming that for a certain transmission line the required phase and characteristic impedance at the operating frequency are ϕ_o and Z_o (where Z_o is considered to be a real number), expressions (2.30) and (2.33) can be inverted, and the series and shunt impedances must take the following values at the design frequency (a T-circuit model—single stage—has been assumed for the artificial transmission line under consideration):[3]

$$Z_s = Z_o\sqrt{\frac{\cos\phi_o - 1}{\cos\phi_o + 1}} \tag{4.2}$$

$$Z_p = \frac{Z_o}{\sqrt{\cos^2\phi_o - 1}} \tag{4.3}$$

The derivative of the phase shift with frequency is given by

$$\left.\frac{d\phi}{d\omega}\right|_{\omega_o} = \frac{1}{\sin\phi}\frac{1}{\chi_p^2}\left(-\chi_p\left.\frac{d\chi_s}{d\omega}\right|_{\omega_o} + \chi_s\left.\frac{d\chi_p}{d\omega}\right|_{\omega_o}\right) \tag{4.4}$$

where χ_s and χ_p are the reactances of the series and shunt branch of the T-circuit, respectively ($Z_s = j\chi_s$ and $Z_p = j\chi_p$). By introducing (4.2) and (4.3) in (4.4), and after

[2] Nevertheless, bandwidth in distributed circuits can be enhanced by increasing the number of elements. An example is the multisection branch line coupler, which can be found in many general textbooks devoted to microwave engineering.

[3] To obtain (4.2) and (4.3), the impedance of the series branch of the T-model (basic cell) has been considered to be Z_s, rather than $Z_s/2$.

some simple calculation, the derivative of the phase at the operating frequency is found to be:

$$\left.\frac{d\phi}{d\omega}\right|_{\omega_o} = \frac{1}{Z_o}\left(\left.\frac{d\chi_s}{d\omega}\right|_{\omega_o} - (\cos\phi_o - 1)\left.\frac{d\chi_p}{d\omega}\right|_{\omega_o}\right) \tag{4.5}$$

The two right-hand side terms in (4.5) are effectively positive since according to the Foster reactance theorem [8], the derivative of the reactance (or susceptance) of a passive and lossless network with frequency is always positive, and $\cos\phi_o \leq 1$. To enhance bandwidth, we must force the derivative of ϕ with frequency to be as small as possible. Thus, according to (4.5), the frequency derivatives of the series and shunt reactances must be both as small as possible. From the Foster theorem, it follows that the optimum metamaterial transmission line model to minimize expression (4.5) is the canonical dual transmission line (see the appendix of Ref. [7]). Hence, it is convenient to calculate expression (4.5) for this particular case. By introducing

$$\chi_s = -\frac{1}{2C_L\omega} \tag{4.6}$$

$$\chi_p = L_L\omega \tag{4.7}$$

in (4.5), one obtains, after some straightforward calculation:

$$\left.\frac{d\phi}{d\omega}\right|_{\omega_o} = \frac{2}{\omega_o}\sqrt{\frac{1-\cos\phi_o}{1+\cos\phi_o}} = \frac{2}{\omega_o}\tan\frac{|\phi_o|}{2} \tag{4.8}$$

Thus, for the optimum transmission line model (in terms of the operative bandwidth) the derivative of phase with frequency does not depend on the required characteristic impedance. It is simply determined by the operating frequency and phase.

It is important to take into account that expression (4.8) is the derivative of the phase with frequency corresponding to a single-unit cell. If a number N of cells is used to obtain the nominal phase shift, ϕ_o, then the phase shift of either cell is ϕ_o/N, and expression (4.8) rewrites as follows:

$$\left.\frac{d\phi}{d\omega}\right|_{\omega_o} = \frac{2}{\omega_o}N\tan\frac{|\phi_o|}{2N} \tag{4.9}$$

A simple analysis of expression (4.9) reveals that $d\phi/d\omega$ decreases as N increases, namely,

$$\frac{2}{\omega_o}N\tan\frac{|\phi_o|}{2N} > \frac{2}{\omega_o}(N+1)\tan\frac{|\phi_o|}{2(N+1)} \tag{4.10}$$

for $N = 1, 2\ldots, \infty$. Therefore, in terms of bandwidth, the optimum solution is an N-stage artificial transmission line with $N \to \infty$. In this case, (4.9) can be expressed as follows:

$$\left.\frac{d\phi}{d\omega}\right|_{\omega_o} = \frac{|\phi_o|}{\omega_o} \tag{4.11}$$

According to (4.11), the derivative of phase with frequency for a dual transmission line in the considered limiting case ($N \to \infty$) is identical to that of a conventional line with identical phase (but different sign) at the same frequency. Therefore, from this result we may conclude that in those applications where the sign of the phase shift is irrelevant (e.g., in 90° impedance inverters and many microwave components based on them [9]), it is not possible to enhance the bandwidth by using artificial lines.[4] If the number of cells is limited to a finite number, the derivative of phase with frequency increases, and the operative bandwidth is degraded, as compared to that of a conventional transmission line.

Bandwidth improvement can be obtained if the sign of the phase is relevant. In this case, we have to compare the dual transmission line with phase ϕ_o (ϕ_o being negative) with a conventional transmission line with equivalent phase shift, that is, $2\pi + \phi_o$. From this comparison, it is obvious (from 4.11) that as long as the required phase shift is higher than π (i.e., $\pi < 2\pi + \phi_o < 2\pi$), the dual transmission line exhibits smaller phase dependence with frequency, and hence it exhibits a better solution in terms of bandwidth. If the number of stages is limited to a finite number, then the limiting phase above which the artificial lines exhibit a better phase response (lower derivative) is no longer π. For a single-stage dual transmission line, such limiting phase can be inferred by simply forcing (4.8) to be $(2\pi + \phi_o)/\omega_o$. It gives $\phi_o = -0.7\pi$, or a positive phase (conventional line of 1.3π). It means that in applications where the sign of the phase shift is fundamental, by using a single-stage dual transmission line bandwidth can be improved if the required (positive) phase shift is comprised between 1.3π and 2π. Let us consider, for instance, a required phase shift of 1.5π, equivalent to $-\pi/2$, to be achieved with an N-stage dual transmission line at the angular frequency ω_o. If N is high enough, the derivative of the phase shift with frequency can be approximated by (4.11),

$$\left.\frac{d\phi}{d\omega}\right|_{\omega_o} = \frac{\pi}{2\omega_o} \tag{4.12}$$

whereas the derivative of the phase with frequency for the ordinary line is

$$\left.\frac{d\phi}{d\omega}\right|_{\omega_o} = \frac{3\pi}{2\omega_o} \tag{4.13}$$

[4] However, device size can be substantially reduced by virtue of the small electrical size of the unit cell of LH or CRLH lines, as can be seen in the power dividers reported in Ref. [9].

Therefore, it is clear that the bandwidth is superior by using a dual transmission line. It should be noted that if the number of stages, N, of the dual transmission line is high, the long wavelength approximation can be applied, and the characteristic impedance is roughly constant with frequency (i.e., 3.38 can be approximated by 3.42). However, if the number of stages is small, or if only one stage is considered, the characteristic impedance will no longer be constant with frequency in the vicinity of the operating frequency. Under these conditions, the functionality of the device may also be limited by the variation of the characteristic impedance.

As highlighted earlier, the optimum metamaterial transmission line for bandwidth enhancement is the dual transmission line. Thus, the phase shifts (π for the infinite stage structure and 1.3π for the one-stage transmission line) below which the dual transmission line is not able to provide an improved bandwidth are fundamental limits. Namely, with CRLH transmission lines (either CL-loaded or resonant type) this limits are even lower. However, despite this, bandwidth enhancement is possible since many microwave components are based on phase differences between transmission lines. To enhance bandwidth, it is necessary that the dispersion characteristics exhibit similar slopes in the vicinity of the operating frequency, and this can be achieved through the considered artificial CRLH lines, as will be shown in the next subsection (see Fig. 4.1). On the other hand, in certain applications, transmission lines with electrical lengths higher than π are required. Under these conditions, the ordinary lines can be replaced with metamaterial transmission lines, with the corresponding bandwidth improvement, as anticipated above and as it will be shown at the beginning of the next subsection.

4.2.1.2 Illustrative Examples

Broadband Series Power Divider The first considered example is a series power divider. Such devices can be of interest to feed an array of antennas, where in-phase signals at either radiating element may be required. Therefore, series power dividers

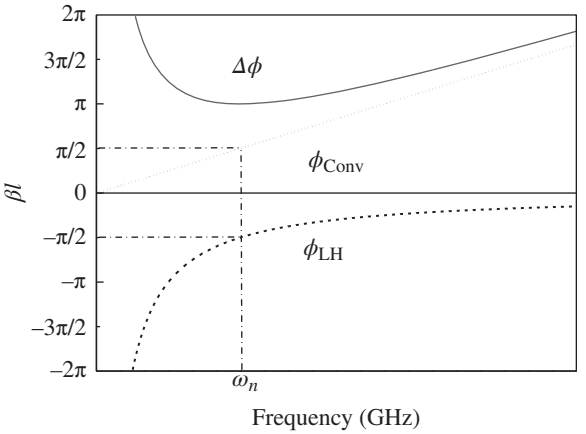

FIGURE 4.1 Illustration of bandwidth enhancement by using a conventional and an LH transmission line. At the design frequency, ω_n, the phase difference, $\Delta\phi$, between the two lines is π, and this difference is roughly preserved in a wide band.

are implemented by means of transmission lines with in-phase input and output signals. If ordinary lines are considered, the required phase shift is 2π at the operating frequency.[5] Alternatively, a balanced CRLH line operating at the transition frequency can be designed to actually achieve zero-phase shift at that frequency. The group delay for the conventional line is $\tau_C = 2\pi/\omega_o$. Therefore, to enhance bandwidth by means of the CRLH line, it is necessary that the group delay at the transition frequency satisfies $\tau_{CRLH} < \tau_C$. In reference to CL-loaded balanced CRLH lines, the phase shift in the vicinity of the transition frequency can be inferred by forcing $\omega_s = \omega_p = \omega_o$ in Equation 3.59. It gives

$$\phi = \beta l = \frac{N\omega}{\omega_R}\left(1 - \frac{\omega_o^2}{\omega^2}\right) \tag{4.14}$$

where we have added N to account for the number of stages (not necessarily one). The group delay at ω_o is simply:

$$\tau_{CRLH} = \left.\frac{d\phi}{d\omega}\right|_{\omega_o} = \frac{2N}{\omega_R} \tag{4.15}$$

By forcing (4.15) to be smaller than τ_C, the following inequality results:

$$\frac{N}{\omega_R} < \frac{\pi}{\omega_o} \tag{4.16}$$

which leads to

$$N\sqrt{\frac{L_R}{C_L}} < \pi Z_o \tag{4.17}$$

with

$$Z_o = \sqrt{\frac{L_R}{C_R}} = \sqrt{\frac{L_L}{C_L}} \tag{4.18}$$

From (4.17), it follows that to obtain a significant bandwidth enhancement, L_R must be small and C_L must be high. This leads also to a small value of C_R and a high value of L_L since (4.18) must be satisfied. Consequently, ω_R must be high and ω_L must be small (see expressions (3.53) and (3.54)).

As an alternative to CRLH lines, enhanced bandwidth series power dividers can be implemented by replacing the 2π ordinary lines with artificial lines consisting of purely left-handed (PLH) line sections alternating with conventional line sections providing exactly the same phase shift but with opposite sign (i.e., a 0° phase shifting

[5] Transmission lines with a phase of $2\pi n$ (n being a positive integer) can also be considered, but bandwidth is optimized by considering $n = 1$ for the reasons explained in Section 4.2.1.1.

line). Let us consider that the 0° line is implemented by combining a conventional line with phase shift $\phi_{CONV} = \phi_C$ at the design frequency, with a PLH line with $\phi_{LH} = -\phi_C$ at that frequency (so that $\phi = \phi_{CONV} + \phi_{LH} = 0$). The derivative of the line phase with frequency at ω_o is

$$\left.\frac{d\phi}{d\omega}\right|_{\omega_o} = \frac{\phi_C}{\omega_o} + \frac{2}{\omega_o}\tan\frac{\phi_C}{2} \tag{4.19}$$

From (4.19), it follows that to maximize the bandwidth it is convenient to choose ϕ_C as small as possible. From this, one concludes that the conventional line must be as short as possible, and C_L and L_L (see expression 3.37) as high as possible. Notice that these conditions are equivalent to those inferred in the previous paragraph in reference to CRLH lines. In practice, ϕ_C is limited since excessive large values for C_L and L_L should be avoided, and a minimum size for the conventional line sections is required.

Following the previous idea, bandwidth improvement was experimentally demonstrated in a 1:4 series power divider operative at 1.92 GHz, where 0° phase shifting lines were used [10]. In-phase signals at the input of either divider branch were achieved through the designed 0° metamaterial transmission lines, placed between the different output branches of the divider. As compared to the conventional device, the metamaterial-based power divider exhibits an improved bandwidth. The conventional and the metamaterial-based series power dividers are compared in Figure 4.2. It is worth mentioning that a significant area reduction is achieved in the divider based on metalines, since these lines are substantially shorter than the conventional 2π transmission lines. This example demonstrates that in applications where line phases larger than π are required, bandwidth can be enhanced by replacing these lines with CRLH lines.[6]

Broadband Rat-Race Hybrid Coupler The second illustrative example is a broadband rat-race hybrid coupler where bandwidth enhancement is obtained by engineering the dispersion of the constitutive transmission lines, with an eye toward achieving similar phase slopes at the design frequencies, following the principle illustrated in Figure 4.1. By using this concept, a rat-race hybrid coupler where the phase balance for the Δ and Σ ports exhibits broader bandwidth, as compared to the conventional counterpart, was demonstrated by Okabe *et al.* [11]. The topology of the conventional rat-race hybrid coupler is depicted in Figure 4.3a. It is essentially a four-port device consisting of a 1.5λ ring structure (where λ is the guided wavelength at the design frequency, ω_o) with the ports equally spaced in the upper half of the ring. In the coupler reported in Ref. [11], the +270° (0.75λ) line section was replaced with a −90° LH line designed to provide the required characteristic impedance (70.7 Ω) and phase (−90°) at the operating frequency. The LH line was implemented by loading a host line with lumped inductors and capacitors in shunt and series connection, respectively. The performance and size of the device is good, with a wide bandwidth for the coupling coefficient and phase balance (see Ref. [11] for more details).

[6] Since the combination of a PLH line and an ordinary line provides a backward and a forward transmission band, the structure can be considered to belong to the category of CRLH lines.

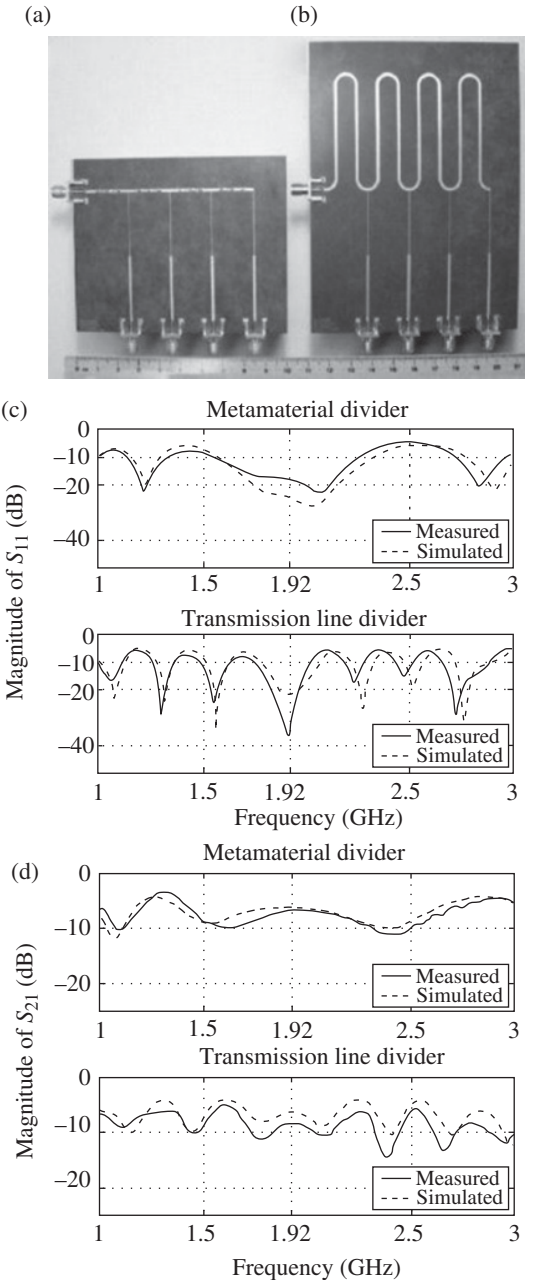

FIGURE 4.2 Metamaterial-based (a) and conventional (b) 1:4 series power dividers with their corresponding measured and simulated frequency responses (only S_{11} (c) and S_{21} (d) are depicted). Reprinted with permission from Ref. [10]; copyright 2005 IEEE.

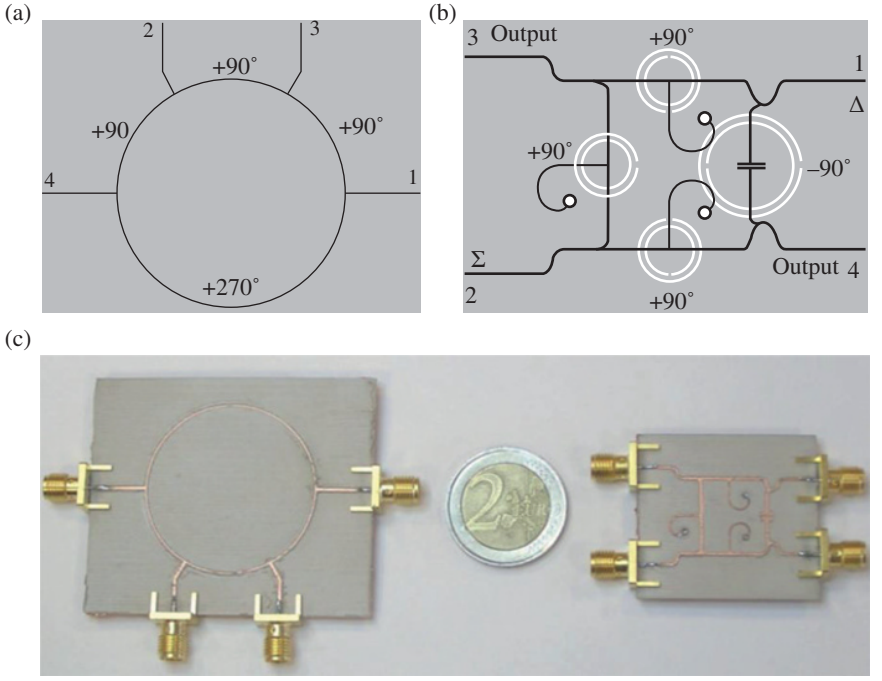

FIGURE 4.3 Layout of the conventional (a) and fully artificial (b) rat-race hybrid couplers. A comparative photograph of both devices can be seen in (c). The devices were fabricated on the *Rogers RO3010* substrate with dielectric constant $\varepsilon_r = 10.2$ and thickness $h = 635$ μm. The active area (excluding access lines) of the CSRR-based hybrid coupler is 3.62 cm^2, whereas the conventional one occupies an area of 10.33 cm^2. Reprinted with permission from Ref. [12], copyright 2007 IEEE.

Alternatively, the metamaterial rat-race hybrid coupler can be implemented by means of the resonant type approach [12]. In this case, not only the 270° line is replaced with an artificial −90° LH line but also the three +90° (right handed – RH) transmission lines are implemented as artificial lines based on CSRRs (the characteristic impedance of these artificial lines is set to 70.7 Ω). Such artificial RH lines are implemented by combining CSRRs with shunt stubs, as Figure 4.4 illustrates. As discussed in Ref. [13], by means of this fully artificial structure (all the lines are artificial) a further controllability on the frequency dependence of the phase of the lines can be achieved, as compared to the structure with only one artificial line (i.e., the LH line providing −90° phase shift, in substitution of the +270° conventional line). Indeed, it is not possible to achieve similar phase slopes between the conventional +90° lines and the −90° LH line in the vicinity of the design frequencies [13] for the structure with only one artificial line. The +90° and −90° CSRR-based lines were optimized in order to exhibit similar phase slopes at the design frequency (notice that expressions 4.4 and 4.5 are valid for the structure of Fig. 4.4). Nevertheless, it should be mentioned that the characteristic impedance of these lines is frequency dependent,

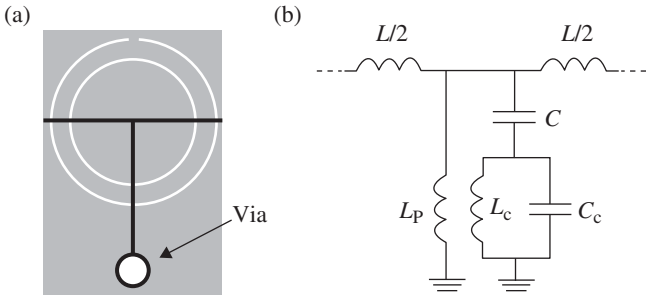

FIGURE 4.4 Typical topology (a) and circuit model (b) of the CSRR-based RH line unit cell. L_p models the shunt stub, grounded by means of a via, whereas the other circuit parameters were described in reference to Figure 3.38. The ground plane, where the CSRRs are etched, is depicted in gray.

and therefore its frequency derivative must be minimized as much as possible for bandwidth optimization. The design equations for both lines are (4.2) and (4.3), subjected to equal phase slopes (expression 4.5) and minimum variation of the characteristic impedance with frequency for both lines. In practice, however, optimization at the layout level is required since the design equations are complex, involve many parameters, and they are difficult to solve analytically.

Figure 4.5 depicts the phase difference between the designed artificial lines, where it can be appreciated that it experiences less variation with frequency as compared with the phase difference of conventional lines or with the phase difference resulting by using a conventional line and a LH line (the design frequency is 1.6 GHz). The layout of the fully artificial rat-race hybrid coupler is also depicted in Figure 4.3 (also in this figure are included the photographs of the conventional and the metamaterial rat-race hybrid couplers, in order to appreciate the achievable size reduction by using metamaterial transmission lines). The simulated and measured impedance matching, coupling and isolation for both structures are depicted in Figure 4.6. In Figure 4.7, the phase balance for the Σ and Δ ports, namely $\phi(S_{42}) - \phi(S_{32})$ and $\phi(S_{41}) - \phi(S_{31})$, respectively, are depicted. In terms of flatness, the phase balance of the fully artificial rat-race exhibits superior performance. Power splitting for both the Δ and the Σ ports exhibits similar characteristics to those measured in the conventional implementation. A comparison between the fully artificial and the conventional rat-race hybrid coupler in terms of bandwidth is represented in Table 4.1. Isolation is comparable in both couplers, although matching is better in the conventional implementation. However, as has been mentioned, phase balance is substantially improved by using metamaterial transmission lines.

The design of the fully artificial rat-race is compatible with planar technology since no lumped elements are used, and size reduction by a factor of 3 is achieved as compared to the conventional implementation. There are other means to achieve size reduction in rat-race hybrid couplers. For instance, small-size devices have been achieved by using folded lines [14], periodically loaded lines [15], synthetic meander lines [16], and stepped impedance resonators [17]. However, in general, these

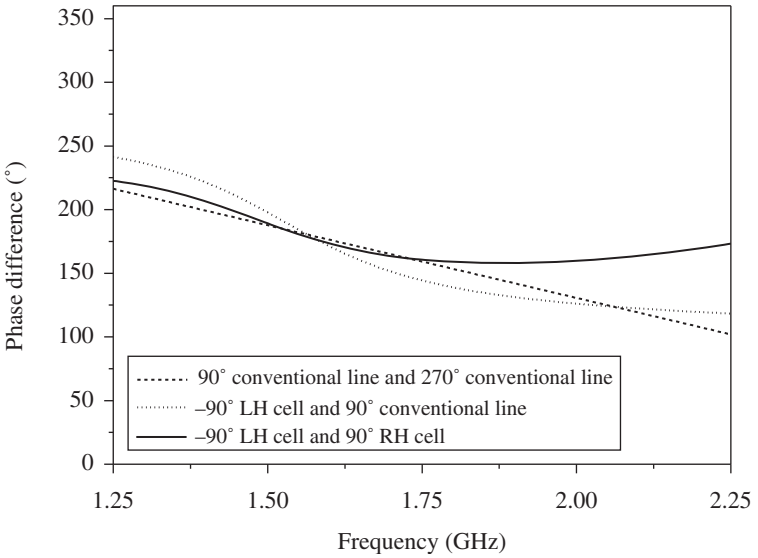

FIGURE 4.5 Representation of the phase difference $\Delta\phi_{S21}$ between the conventional +90° and +270° lines (dashed line), the conventional +90° and LH −90° lines (dotted line) and the artificial RH +90° and LH −90° lines (solid line). The phase difference is roughly 180° at the design frequency (1.6 GHz). Reprinted with permission from Ref. [13], copyright 2008 John Wiley.

techniques do not provide a comparable performance, in terms of bandwidth, as compared to the devices based on metamaterial transmission lines [11, 12]. An exception to this is the rat-race hybrid presented in Ref. [18], where the 270° branch is replaced by a −90° branch realized by a +90° microstrip line and a CPW phase inverter. However the design requires a CPW-to-microstrip transition and fabrication is more complex.

The technique for bandwidth enhancement based on metamaterial transmission lines has been applied to other microwave components, such as phase shifters [19, 20], Wilkinson baluns [21], and T-junction power splitters with balanced [22] or quadrature phase [23] outputs over a broad band, among others.

4.2.2 Dual-Band and Multiband Components

Dual-band components exhibit certain functionality at two arbitrary frequencies (the concept can be extended to tri-band, quad-band and, in general, to *n*-band components by satisfying the required functionality at three, four, or *n* controllable frequencies, respectively).[7] Conventional distributed microwave components typically exhibit a

[7] These microwave components exhibiting multiple band functionality at controllable frequencies (i.e., those dictated by design requirements) are designated as multiband devices. By contrast, devices operative at a single frequency are called single-band or mono-band components.

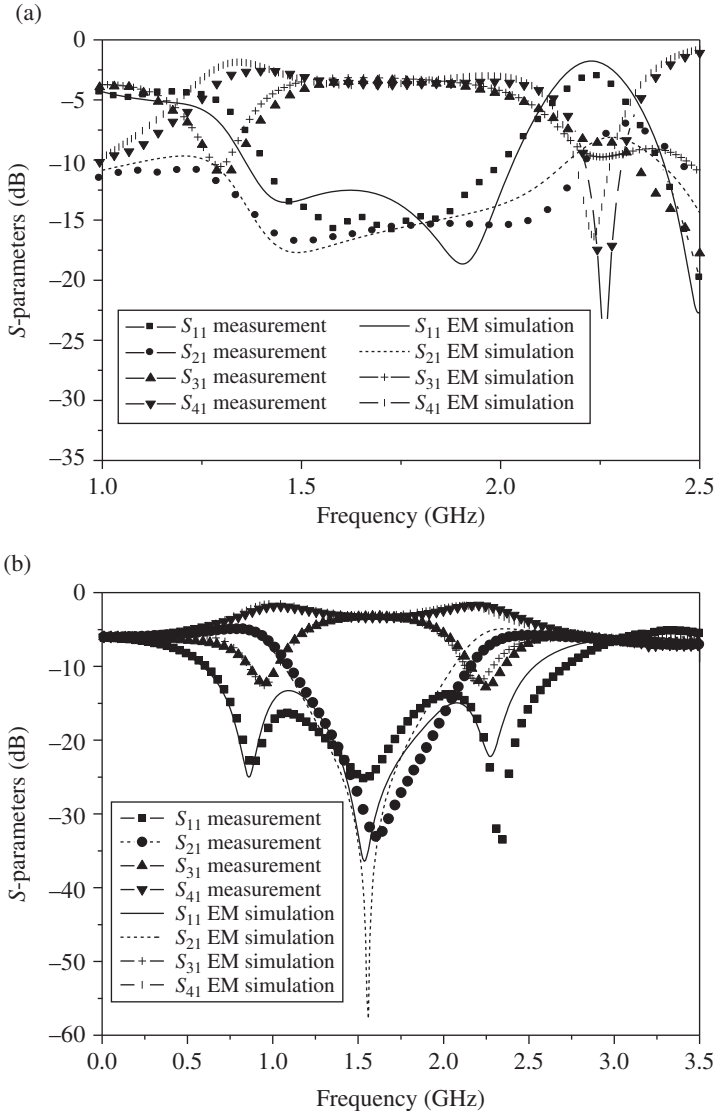

FIGURE 4.6 Impedance matching (S_{11}), coupling, (S_{31}, S_{41}) and isolation (S_{21}) for the CSRR-based hybrid coupler (a) and conventional coupler (b). Reprinted with permission from Ref. [12]; copyright 2007 IEEE.

periodic response and hence exhibit the required functionality at the design frequency and at its odd harmonics. However, such devices cannot be considered multiband components since the operating frequencies cannot be set to those values corresponding to system requirements. They are thus single-band components, that is, their functionality can only be satisfied at a single-design frequency.

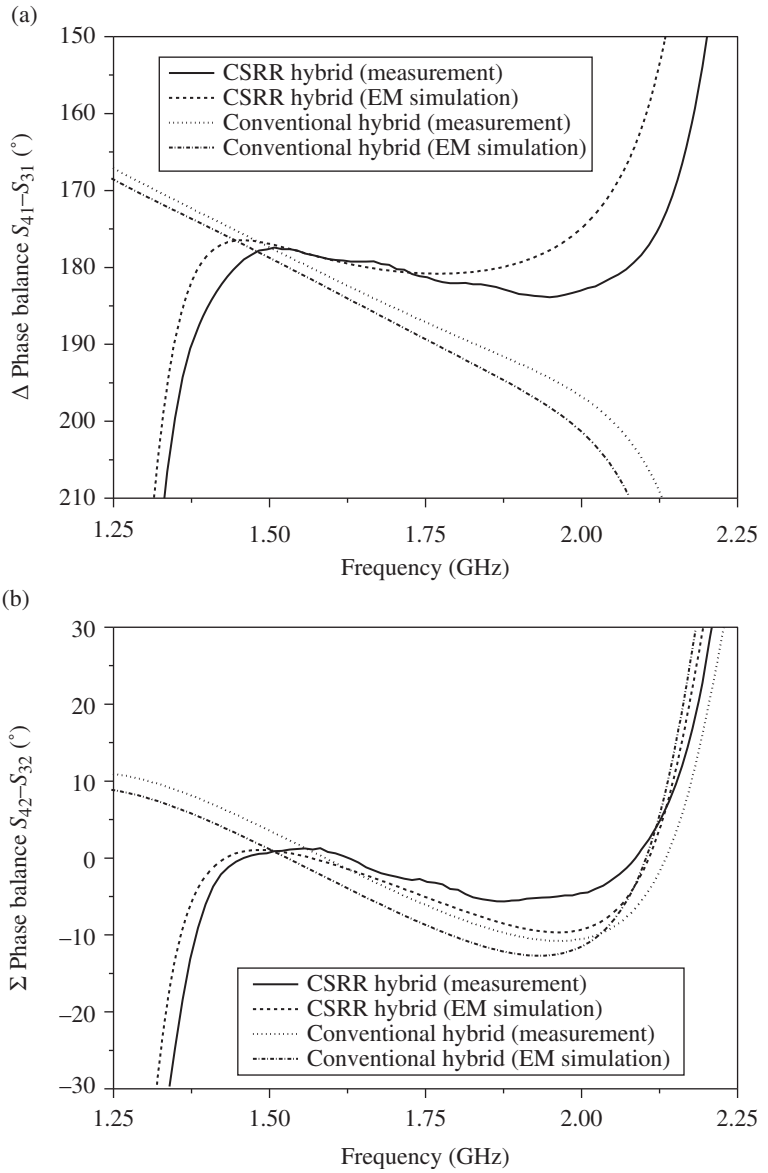

FIGURE 4.7 Phase balance for the Δ (a) and Σ (b) ports. Reprinted with permission from Ref. [12], copyright 2007 IEEE.

4.2.2.1 Principle for Dual-Band and Multiband Operation The larger number of free parameters of CRLH transmission lines (as compared to conventional lines) is useful for the design of dual-band and multiband components through dispersion and impedance engineering. To achieve dual-band operation, it is necessary to satisfy

TABLE 4.1 Bandwidth characteristics in the conventional and artificial rat-race couplers

	Conventional		Fully artificial	
	Σ Input	Δ Input	Σ Input	Δ Input
Output (dB)	**3.10 ± 0.25**	**3.10 ± 0.25**	**3.5 ± 0.25**	**3.38 ± 0.25**
Range (GHz)	1.38–1.70	1.40–1.72	1.55–1.89	1.54–1.89
Bandwidth (%)	20	20	20	20
Phase balance (degrees)	**0 ± 5**	**180 ± 5**	**0 ± 5**	**180 ± 5**
Range (GHz)	1.40–1.65	1.40–1.65	1.40–2.10	1.40–2.10
Bandwidth (%)	16	16	40	40
Isolation (dB)	**< −15**		**< −15**	
Range (GHz)	1.20–1.90		1.35–2.10	
Bandwidth (%)	45		44	
Return loss (dB)	**< −10**		**< −10**	
Range (GHz)	1.13–1.99	0.59–2.50	1.41–2.26	1.40–2.01
Bandwidth (%)	55	123	46	36

Bold indicates the main characteristics of the rat-race couplers.

the phase and impedance requirements (for the transmission lines and stubs of the circuit) at the two design frequencies, f_1 and f_2. Let us consider that the required phases are ϕ_1 and ϕ_2 at the design frequencies. As can be seen in Figure 4.8, in general, such phase values cannot simultaneously be satisfied by means of ordinary lines. However, by using artificial lines, we can tailor the dispersion diagram to set the phases to the required values at the two operating frequencies (i.e., Fig. 4.8 illustrates). One important aspect is that, contrary to conventional lines, metamaterial transmission lines exhibit frequency-dependent characteristic impedance. Thus, such artificial lines must be designed to satisfy also the impedance requirements at the design frequencies. For multiband functionality, the idea is to increase the number of elements of the artificial lines in order to enhance the degrees of freedom, and thus be able to satisfy the phase and impedance requirements at more than two frequencies, as will be shown later.

4.2.2.2 Main Approaches for Dual-Band Device Design and Illustrative Examples Practical dual-band components have been implemented either by using artificial lines that combine ordinary (RH) lines with PLH lines[8] made of SMT components, or by means of fully planar CRLH transmission lines.

Dual-Band Devices Based on a Combination of Ordinary and PLH Lines: Application to a Dual-Band Branch Line Hybrid Coupler For the implementation of dual-band metamaterial transmission lines, one approach is to cascade multiple

[8] Although PLH lines do not exist in practice, as discussed in Chapter 3, we intentionally use this terminology to emphasize the fact that the considered SMT-based LH lines roughly behave as PLH lines in the frequency region of interest. This means that the parameters of the host line can be neglected in such region.

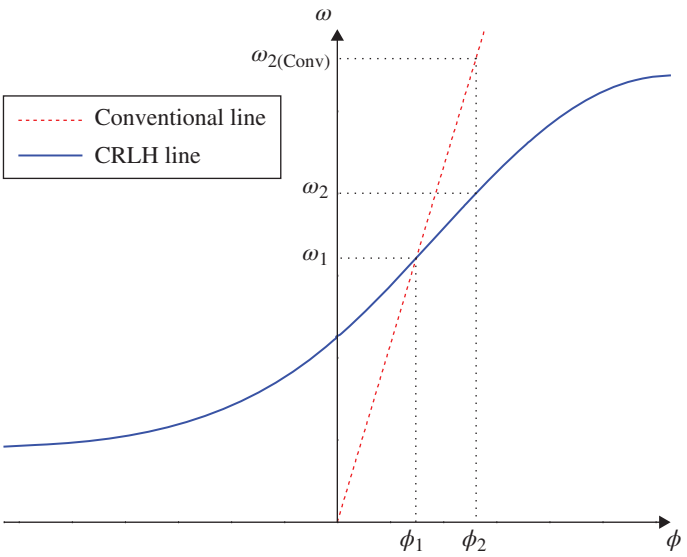

FIGURE 4.8 Illustration of the single-band operation of conventional lines, as compared to the possibility of designing dual-band metamaterial transmission lines, with the required phase at arbitrary frequencies.

(N) effectively homogeneous unit cells. For instance, a balanced line in the vicinity of the transition frequency exhibits roughly constant (i.e., frequency independent) characteristic impedance. Thus, by setting this impedance to the required value and adjusting the slope of the dispersion diagram so that the phases of the unit cells are ϕ_1/N and ϕ_2/N at the design frequencies, dual-band operation can be achieved. Practical dual-band components have indeed been implemented by cascading conventional lines (with positive phase shift) and backward (i.e., PLH) lines implemented by means of lumped elements [2]. As long as the phase shift per unit cell in the backward lines is small, the phase can be approximated by

$$\phi_{CRLH} = \phi_R - \frac{N}{\omega\sqrt{L_L C_L}} \tag{4.20}$$

where the subindex *CRLH* denotes the phase of the composite structure, N is the number of unit cells of the backward wave transmission line, and $\phi_R = \beta_R l = (\omega/v_p)l$, where v_p is the phase velocity of the conventional line and l its length. By forcing the phase of the composite structure to be $\phi_{CRLH} = \phi_1$ at $\omega_1 = 2\pi f_1$ and $\phi_{CRLH} = \phi_2$ at $\omega_2 = 2\pi f_2$ (with $\omega_2 > \omega_1$), and the characteristic impedance of both lines to Z_o, the length of the line and the reactive elements of the PLH line are found to be[9]

[9] Since the PLH line is considered to satisfy the homogeneity condition, the characteristic impedance of this line is simply given by $Z_o = (L_L/C_L)^{1/2}$.

$$l = \frac{v_p(\phi_2\omega_2 - \phi_1\omega_1)}{\omega_2^2 - \omega_1^2} \tag{4.21}$$

$$C_L = \frac{N}{Z_o}\frac{\omega_2^2 - \omega_1^2}{\omega_1\omega_2(\phi_2\omega_1 - \phi_1\omega_2)} \tag{4.22}$$

$$L_L = Z_o N\frac{\omega_2^2 - \omega_1^2}{\omega_1\omega_2(\phi_2\omega_1 - \phi_1\omega_2)} \tag{4.23}$$

and the transverse dimensions of the conventional line must be adjusted to provide the required characteristic impedance, Z_o. Notice that, depending on the required phases, the conventional line length and/or the elements of the PLH line, L_L and C_L, may be negative. For instance, if $\phi_1 = \phi_2 > 0$, l is positive, but L_L and C_L take negative values. Although this negative element values cannot be implemented (unless non-Foster active components are used, as discussed in the last chapter of this book), from a mathematical viewpoint the negative phase of the PLH line reverses its sign and for this reason a mathematical solution exists for negative values of L_L and C_L. In order to have positive values of L_L and C_L, the following condition must be satisfied:

$$\phi_2\omega_1 - \phi_1\omega_2 > 0 \tag{4.24}$$

Notice that this condition forces $\phi_2 > \phi_1$, and hence it leads also to a positive value of l.

If both phases are positive, it is necessary that $\phi_2/\phi_1 > \omega_2/\omega_1$ in order to satisfy (4.24). Thus, the relative values of the operating frequencies dictate the minimum ratio between the (positive) phases at these frequencies. Let us consider, for instance, that $\phi_1 = +90°$ and $\phi_2 = +270°$. This is an interesting case because such phases are equivalent (hence providing the same functionality) for many applications (i.e., the implementation of impedance inverters). According to (4.24), the ratio of the operating frequencies is limited to 3. If $\phi_2 > 0$ and $\phi_1 < 0$, expression (4.24) is always satisfied, and a solution always exists regardless of the values of ω_1 and ω_2 (with $\omega_2 > \omega_1$). Let us consider, for instance, that $\phi_2 = -\phi_1 = 90°$. Introducing these phase values in (4.21)–(4.23), the following results are obtained:

$$l = \frac{\pi v_p}{2(\omega_2 - \omega_1)} \tag{4.25}$$

$$C_L = \frac{2N}{\pi Z_o}\frac{(\omega_2 - \omega_1)}{\omega_1\omega_2} \tag{4.26}$$

$$L_L = \frac{2NZ_o}{\pi}\frac{(\omega_2 - \omega_1)}{\omega_1\omega_2} \tag{4.27}$$

Thus, expressions (4.25)–(4.27) are simple design equations for the implementation of dual-band impedance inverters exploiting the LH and the RH band of the CRLH artificial transmission line.

Following the previous strategy, several dual-band components have been implemented. For instance, a dual-band Wilkinson power divider is reported in Ref. [2], where the phases of the two impedance inverters of the divider are set to $\phi_1 = -90^\circ$ and $\phi_2 = +90^\circ$ at the operating frequencies $f_1 = 1$ GHz and $f_2 = 3.1$ GHz, respectively (Eqs. 4.25–4.27 apply in this case). As an illustrative result of the dual-band approach based on the combination of ordinary and PLH line sections, a dual-band branch line hybrid coupler is reported here [24] (the lumped elements are implemented by means of SMT chip components). The design frequencies are $f_1 = 0.93$ GHz and $f_2 = 1.78$ GHz, and the electrical lengths of the four coupler branches are set to $\phi_1 = +90^\circ$ and $\phi_2 = +270^\circ$ at those frequencies. The design equations are thus given by (4.21)–(4.23), with the required values of the phases. The fabricated prototype device is depicted in Figure 4.9, where matching, coupling, and isolation are also depicted. The characterization results reveal that the dual-band functionality is satisfied at the desired frequencies, with near −3 dB transmission between the input port and the coupled and through ports. Other devices based on this approach are reported in Ref. [25–27], including an active device (i.e., a dual-band Class-E power amplifier [27]).

Dual-Band Devices based on Fully Planar CRLH Lines: Application to Power Dividers and Branch Line Hybrid Couplers Although the size of the dual-band components considered in the previous subsection is moderately small, the use of SMT components may represent a severe limitation in certain applications, and inaccuracies may appear due to the limited number of available reactive element values. The use of lumped elements can be avoided by implementing the CRLH lines with semilumped (i.e., fully planar) components. Typically, the size of semilumped elements is larger than the size of lumped components. For this reason, dual-band devices based on semilumped CRLH lines are typically implemented by means of a single unit cell.

Let us consider the implementation of dual-band ±90° transmission lines by means of fully planar CRLH lines based on the canonical T-circuit model of Figure 3.20. The line must be designed so that the first and second operating frequencies lie in the LH and RH bands, respectively. According to this, the electrical length and characteristic impedance must be set to $\phi = \phi_1 = -90^\circ$ and $Z_o = Z_1$ at the lower frequency, and $\phi = \phi_2 = +90^\circ$ and $Z_o = Z_2$ at the upper frequency (typically $Z_1 = Z_2$, but at the moment this condition is relaxed). By forcing the above phases and characteristic impedances at the design frequencies, the following conditions result:

$$\chi_s(\omega_1) = -Z_1 \tag{4.28a}$$

$$\chi_p(\omega_1) = +Z_1 \tag{4.28b}$$

$$\chi_s(\omega_2) = +Z_2 \tag{4.28c}$$

$$\chi_p(\omega_2) = -Z_2 \tag{4.28d}$$

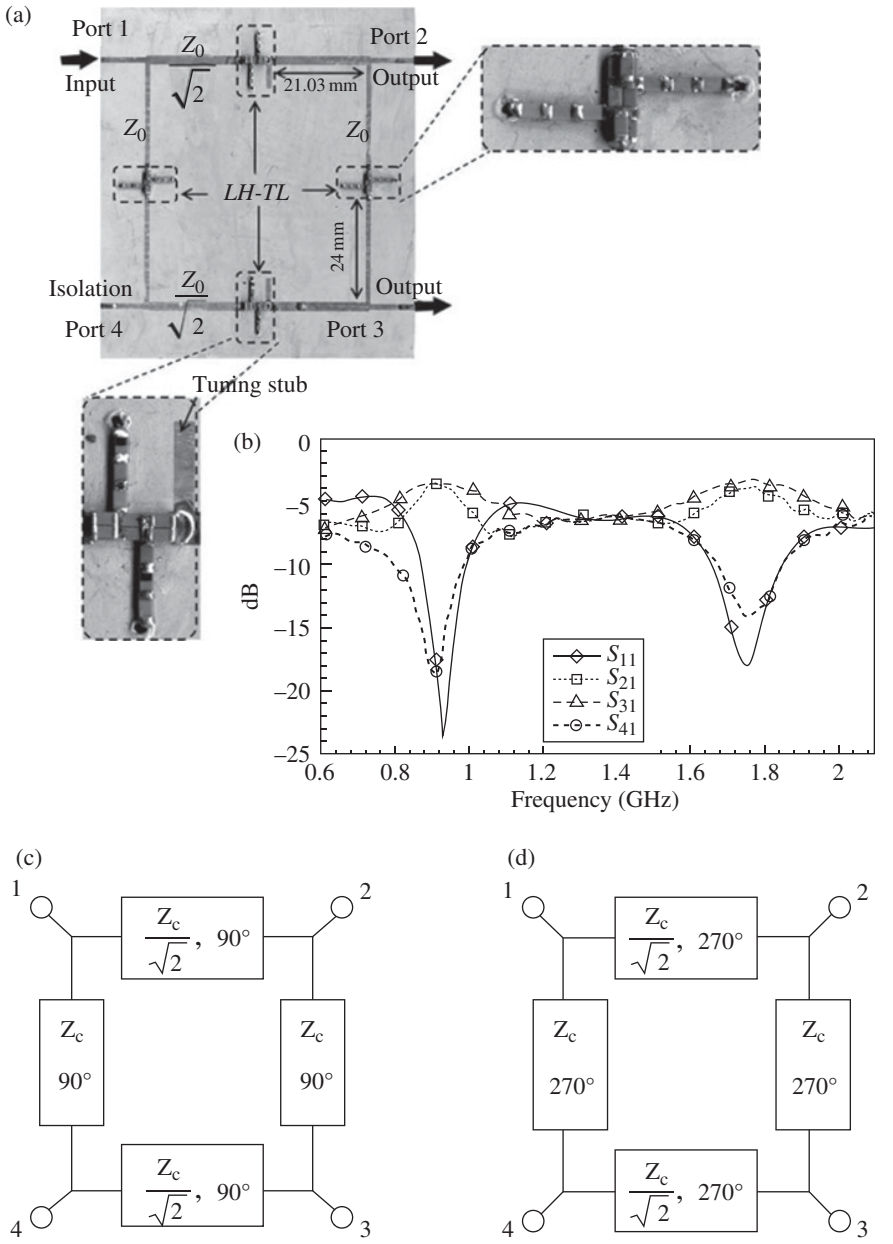

FIGURE 4.9 Dual-band branch line coupler (a), measured frequency response (b), and schematics of the coupler for the two operating frequencies f_1 (c) and f_2 (d). Reprinted with permission from Ref. [24]; copyright 2004 IEEE.

as it is derived from (2.30) and (2.33), χ_s and χ_p being the series and shunt reactance, respectively, of the T-circuit model of the unit cell. Since the circuit model has four reactive elements, they are univocally determined from Equations 4.28, that is,

$$L_R = \frac{2(Z_1\omega_1 + Z_2\omega_2)}{\omega_2^2 - \omega_1^2} \tag{4.29a}$$

$$C_L = \frac{\omega_2^2 - \omega_1^2}{2\omega_1\omega_2(Z_1\omega_2 + Z_2\omega_1)} \tag{4.29b}$$

$$L_L = \frac{(\omega_2^2 - \omega_1^2)Z_1Z_2}{\omega_1\omega_2(Z_1\omega_1 + Z_2\omega_2)} \tag{4.29c}$$

$$C_R = \frac{Z_1\omega_2 + Z_2\omega_1}{(\omega_2^2 - \omega_1^2)Z_1Z_2} \tag{4.29d}$$

It is interesting to mention that the series, ω_s, and shunt, ω_p, resonance frequencies satisfy the following condition:

$$\omega_s\omega_p = \omega_1\omega_2 \tag{4.30}$$

In general, the elements given by (4.29) do not correspond to a balanced CRLH unit cell. However, if the characteristic impedances at both design frequencies are forced to take the same value ($Z_1 = Z_2$),[10] the resulting line is balanced and

$$\omega_s = \omega_p = \sqrt{\omega_1\omega_2} \tag{4.31}$$

In this case ($Z_1 = Z_2 = Z_o$), the elements are simplified to

$$L_R = \frac{2Z_o}{\omega_2 - \omega_1} \tag{4.32a}$$

$$C_L = \frac{\omega_2 - \omega_1}{2\omega_1\omega_2 Z_o} \tag{4.32b}$$

[10] In most dual-band applications, the devices must exhibit the same functionality at the design frequencies and, therefore, $Z_1 = Z_2$. Nevertheless, since the considered artificial lines allow us to implement dual-band impedance inverters with different impedance value at each frequency, the analysis of the more general case with $Z_1 \neq Z_2$ is also of interest.

$$L_{\mathrm{L}} = \frac{(\omega_2 - \omega_1) Z_{\mathrm{o}}}{\omega_1 \omega_2} \tag{4.32c}$$

$$C_{\mathrm{R}} = \frac{1}{(\omega_2 - \omega_1) Z_{\mathrm{o}}} \tag{4.32d}$$

and (4.32) can be used for design purposes.

In practice, fully planar dual-band components based on dual-band impedance inverters can be implemented by means of OSRR/OCSRR loaded lines. Certainly, the circuit model of these lines (see Fig. 3.58) is not exactly the canonical circuit model of a CRLH line, due to the presence of the parasitic elements (L and C). Nevertheless, the previous analysis can be applied for design purposes. To clarify the design process, let us consider the implementation of a dual-band impedance inverter functional at $f_1 =$ 2.4 GHz and $f_2 = 3.75$ GHz, with $Z_{\mathrm{o}} = 35.35\ \Omega$ and electrical length of $\phi_1 = -90^\circ$ at f_1 and $\phi_2 = +90^\circ$ at f_2, (this inverter will be applied to the design of a power divider) [28]. According to the circuit model of Figure 3.58c, the design equations are those given by (4.28) with $Z_1 = Z_2 = Z_{\mathrm{o}} = 35.35\ \Omega$ and χ_{s} and χ_{p} given by (3.99). However, there are six unknowns (the six reactive elements of the circuit of Fig. 3.58c). The procedure to determine the element values is as follows: in a first step, L and C (the parasitics in the model of Fig. 3.58c) are neglected, and the other four element values are inferred from the four equations (4.32) (with $L'_{\mathrm{p}} = L_{\mathrm{L}}$, $C'_{\mathrm{p}} = C_{\mathrm{R}}$, $L'_{\mathrm{s}} = L_{\mathrm{R}}/2$, and $C_{\mathrm{s}} = 2C_{\mathrm{L}}$). Then a layout for the OSRR and OCSRR stages is generated so that the extracted parameters for the resonators (see Appendix G) are identical to those inferred in the first step. This gives also the parasitic values, which are introduced in (3.99). Finally, the other element values (L'_{p}, C'_{p}, L'_{s}, and C_{s}) are recalculated in order to satisfy (4.28). Obviously, the layout must also be readjusted in order to be in coherence with the recalculated reactive elements (the parasitics do not experience a significant variation). By considering the *Rogers RO3010* substrate with thickness $h = 0.635$ mm and dielectric constant $\varepsilon_{\mathrm{r}} = 10.2$; and by applying the previous procedure, the elements of the circuit model of Figure 3.58c were found to be $C = 0.2$ pF, $L = 0.25$nH, $C_{\mathrm{s}} = 0.66$ pF, $L'_{\mathrm{s}} =$ 3.74 nH, $C'_{\mathrm{p}} = 2.99$ pF, and $L'_{\mathrm{p}} = 0.83$ nH. The layout of the dual-band impedance inverter is depicted in Figure 4.10, with the circuit and electromagnetic (EM) simulation of the phase and characteristic impedance. These results reveal that the required characteristics are satisfied. By cascading a 50 Ω input (access) line and two 50 Ω output lines, the dual-band power splitter results. The photograph of this device and the simulated and measured power splitting and matching are depicted in Figure 4.11. The required functionality at the two operating frequencies is clearly achieved.

Let us now consider the implementation of dual-band ±90° transmission lines by means of CSRR/gap-loaded CRLH microstrip lines. The lumped-element equivalent circuit model of the unit cell of the CSRR/gap-loaded line (depicted in Fig. 3.38b) is described by means of five independent parameters, whereas the phase and impedance requirements represent only four conditions (expressions 4.28). Thus, the circuit parameters of the unit cell cannot be univocally determined, unless an additional condition is imposed. If the structure is forced to be balanced, the series and shunt resonance

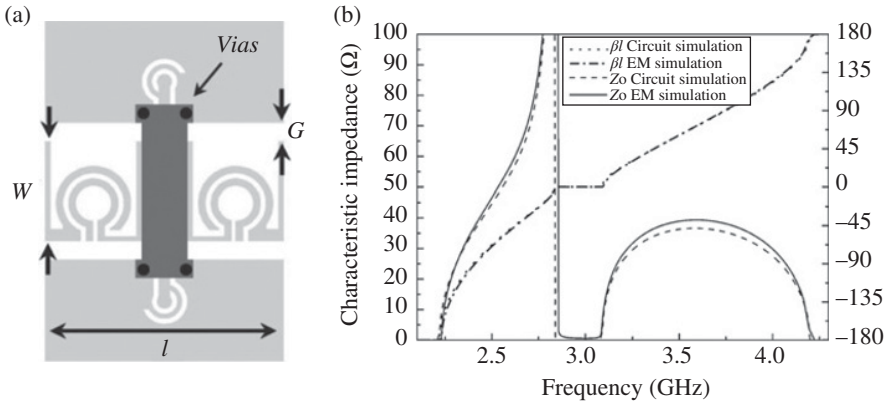

FIGURE 4.10 Layout (a) and circuit and EM simulation (b) of the OSRR/OCSRR-based dual-band impedance inverter. Dimensions are $l = 9$ mm, $W = 4$ mm, and $G = 0.74$ mm. For the OCSRRs $r_{ext} = 0.9$ mm, $c = 0.2$ mm, and $d = 0.2$ mm. For the OSRRs, $r_{ext} = 1.5$ mm, $c = 0.3$ mm, and $d = 0.2$ mm. The wide metallic strip in the back substrate side was added in order to enhance the shunt capacitance of the OCSRR stage, as required to achieve the electrical characteristics of the device. Reprinted with permission from Ref. [28]; copyright 2009 IEEE.

frequencies must be identical. This additional condition leads to the following element values:

$$L = \frac{2(Z_1\omega_1 + Z_2\omega_2)}{\omega_2^2 - \omega_1^2} \tag{4.33a}$$

$$C_g = \frac{\omega_2^2 - \omega_1^2}{2\omega_1\omega_2(Z_1\omega_2 + Z_2\omega_1)} \tag{4.33b}$$

$$C = \frac{Z_1\omega_2 + Z_2\omega_1}{(Z_2^2 - Z_1^2)\omega_1\omega_2} \tag{4.33c}$$

$$C_c = \frac{Z_1\omega_2 + Z_2\omega_1}{(\omega_2^2 - \omega_1^2)Z_1Z_2} \tag{4.33d}$$

$$L_c = \frac{(Z_1\omega_1 + Z_2\omega_2)(\omega_2^2 - \omega_1^2)Z_1Z_2}{\omega_1\omega_2(Z_1\omega_2 + Z_2\omega_1)^2} \tag{4.33e}$$

where Z_1 and Z_2 are the inverter impedances at the operating frequencies. Inspection of Equations 4.33 reveals that L, C_g, C_c, and L_c are always positive (notice that $\omega_2 > \omega_1$). However, C may be negative (for $Z_1 > Z_2$), or $C = \infty$ (for a dual-band impedance inverter with identical impedances $Z_1 = Z_2$). If $Z_1 > Z_2$ ($C < 0$), the inverter cannot be synthesized by means of a balanced cell described by the model of Figure 3.38b.

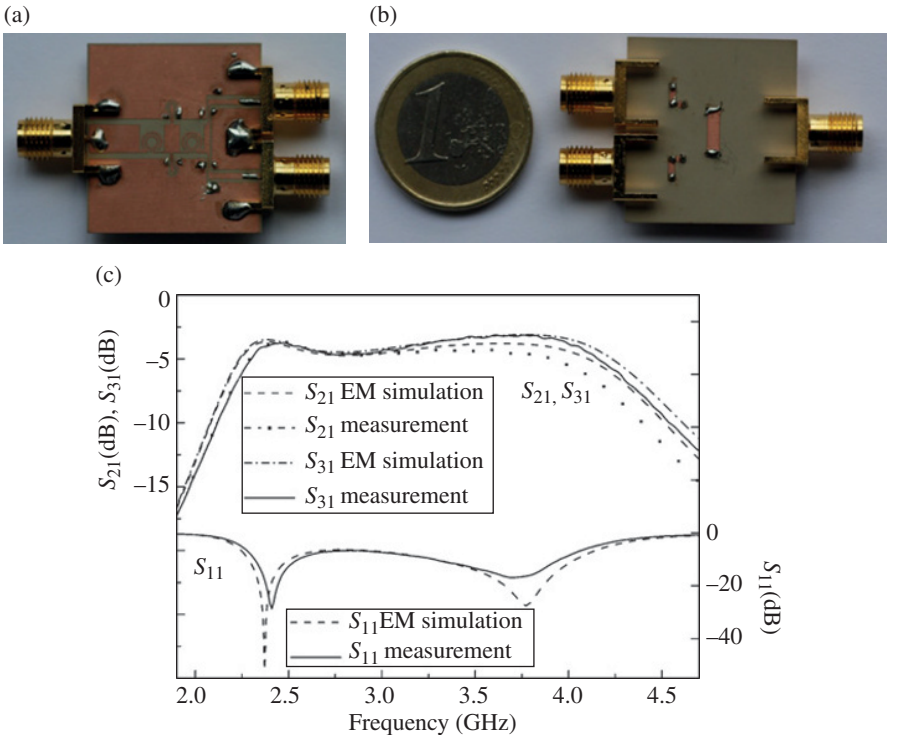

FIGURE 4.11 Photograph of the fabricated dual-band power splitter based on the inverter of Figure 4.10. (a) Top, (b) bottom, and (c) frequency response. Reprinted with permission from Ref. [28]; copyright 2009 IEEE.

If $Z_1 = Z_2 = Z_o$, as most applications require, the inverter can be synthesized by balancing the line, but substituting the capacitance C with an electrical short. In practice, this is not possible by using the cell topology shown in Figure 3.38b. Notice, however, that this case corresponds to the balanced CRLH line based on the canonical circuit model of Figure 3.20, discussed in the previous paragraph. In other words, expressions (4.33) with $Z_1 = Z_2 = Z_o$ provide element values identical to those given by (4.32). Hence, in order to implement dual-band quarter wavelength impedance inverters with identical impedances (at the frequencies of interest) by means of CSRR/gap-loaded CRLH unit cells, such cells must be designed without the restriction of being balanced. Nevertheless, the circuit parameters of the series branch, L and C_g are still univocally determined (and given by expressions 4.33a and 4.33b) under the unbalance condition.[11] The elements C, L_c, and C_c must be chosen in order to satisfy (4.28b) and (4.28d). This gives certain flexibility in the determination of such elements that

[11] Notice that according to (4.28), the elements of the series (L, C_g) and shunt (C, L_c, C_c) branches are independently determined. Thus, introduction of an additional element (the coupling capacitance C) in the shunt branch does not modify the equations giving the elements of the series branch.

can be of interest to ease their physical implementation. However, as discussed in Chapter 3, CSRR/gap-loaded lines exhibit a transmission zero to the left of the first (LH) band (expression 3.86). By considering the position of this transmission zero as an additional condition to be satisfied by the elements of the shunt branch, such elements are univocally determined and given by[12]

$$\frac{L_c\omega_1}{1-L_cC_c\omega_1^2}-\frac{1}{C\omega_1}=Z_o \tag{4.34a}$$

$$\frac{L_c\omega_2}{1-L_cC_c\omega_2^2}-\frac{1}{C\omega_2}=-Z_o \tag{4.34b}$$

$$\frac{1}{\sqrt{L_c(C+C_c)}}=\omega_z \tag{4.34c}$$

where $\omega_z = 2\pi f_z$ is the angular frequency of the transmission zero.

Depending on the specific values of the characteristic impedance of the inverter, the design frequencies (including the transmission zero frequency) and the parameters of the substrate, it may be difficult to synthesize the element values with an implementable layout. Let us consider this situation by means of a specific example and the proposed solution [29]. The objective is again to design a dual-band power divider by means of a $Z_o = 35.35\ \Omega$ quarter wavelength impedance inverter. The operating frequencies are set to to $f_1 = 0.9$ GHz and $f_2 = 1.8$ GHz and the transmission zero to $f_z = 0.5$ GHz. The resulting element values are $L = 12.5$ nH, $C = 24.9$ pF, $C_g = 1.25$ pF, $L_c = 3.38$ nH, and $C_c = 5.10$ pF. With the element values of L, C, and C_g, the convergence region in the L_c–C_c plane was obtained according to the method reported in Appendix H,[13] and the target values of L_c and C_c do not belong to such region (the considered substrate is the *Rogers RO3010*, with thickness $h = 0.635$ mm and dielectric constant $\varepsilon_r = 10.2$). This means that it is not possible to implement the dual-band impedance inverter in that substrate by merely considering the CSRR/gap-loaded line (some element values are too extreme). However, it is expected that by cascading transmission line sections at both sides of the CSRR/gap-loaded line, the element values of the cell are relaxed, and a solution within the convergence region arises. Therefore, two identical 35.35 Ω transmission line sections are cascaded at both sides of the CSRR/gap-loaded line. The width of these line sections is 1.127 mm, corresponding to the indicated characteristic impedance in the considered substrate. Notice that by cascading such 35.35 Ω lines, the electrical length at the operating frequencies is the sum of the electrical lengths of the lines plus the electrical length

[12] Isolation of C, L_c, and C_c from expressions (4.34) is cumbersome and gives huge analytical expressions to be included.

[13] Actually, the method given in Appendix H is for CSRR-loaded lines, but the procedure to determine the convergence region in the L_c–C_c subspace for CSRR/gap-loaded lines is very similar (see Ref. [29] for further details).

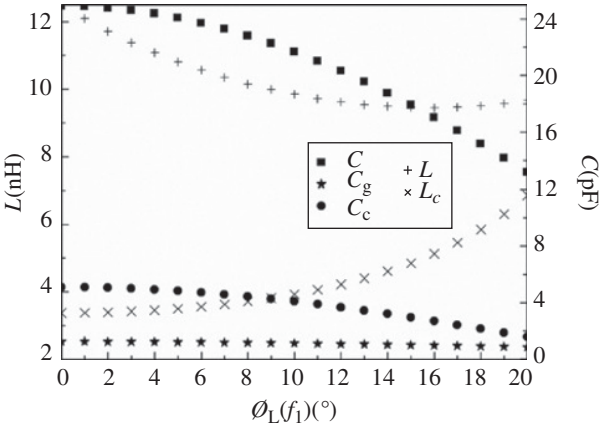

FIGURE 4.12 Dependence of the element values of the CSRR/gap-loaded line with the phase of each cascaded transmission line section at f_1. Reprinted with permission from Ref. [29]; copyright 2013 IEEE.

of the CSRR-based cell. Thus, the phase condition that must satisfy the CSRR/gap-loaded line can be expressed as $\phi_1 = -90^\circ - 2\phi_L(f_1)$ and $\phi_2 = +90^\circ - 2\phi_L(f_2)$, where ϕ_1 and ϕ_2 are the electrical lengths of the CSRR-based cell at the design frequencies f_1 and f_2, and ϕ_L is the phase introduced by the line at the indicated frequency.

A parametric analysis, consisting of obtaining the element values of the CSRR-based cell for different values of the length of the cascaded transmission line sections (and hence $\phi_L(f_1)$ and $\phi_L(f_2)$), was made. The results are depicted in Figure 4.12. It can be observed that for small values of $\phi_L(f_1)$, L and C are too large for being implemented. Large L means a small value of the strip width, W, of the host line, but this is not compatible with a large C value. On the other hand, the values of L_c and C_c without cascaded line sections, that is, $\phi_L(f_1) = 0^\circ$, give extreme values of d and c, that is, large value of d and small value of c. However, by increasing $\phi_L(f_1)$ (or the length of the cascaded lines), the variation of the elements of the central CSRR-gap-based cell goes in the correct direction for their implementation. Specifically, a pair of transmission line sections with $\phi_L(f_1) = 15^\circ$ was considered. With this phase, the required electrical lengths for the CSRR-based cell at the operating frequencies are $\phi_1 = -120^\circ$ and $\phi_2 = +30^\circ$. The element values providing these phases and the required characteristic impedance are $L = 9.45$ nH and $C = 17.9$ pF, $C_g = 1.01$ pF, $L_c = 4.85$ nH, and $C_c = 2.95$ pF, and these values lead us to an implementable layout.[14] The reason of choosing this phase shift for the lines is that it gives the minimum value of L (see Fig. 4.12) and a reasonable small value of C, with L_c not so small and C_c not so large. Notice that C_g does not experience significant variations with $\phi_L(f_1)$.

[14] These element values were derived from (2.30) and (2.33) by forcing the phases and characteristic impedance to the required values at the operating frequencies, and by means of (3.86). Expressions (4.34) only apply if $\phi_1 = -90^\circ$ and $\phi_2 = +90^\circ$.

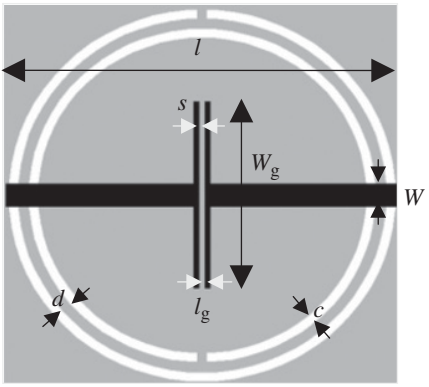

FIGURE 4.13 CSRR/gap-loaded microstrip line with T-shaped gap, and relevant dimensions.

The layout of the CSRR/gap-loaded line was inferred from the ASM-based synthesis method reported in Appendix H, where a T-shaped geometry for the gap was considered.[15] The geometrical parameters of the synthesized structure are (see Fig. 4.13) $l = 14.42$ mm, $W = 0.87$ mm, $c = 0.34$ mm, $d = 0.40$ mm, $W_g = 7.13$ mm, and convergence (with a relative error of 0.012—see Appendix H for more details) was obtained after six iterations. The comparison of the electrical length and characteristic impedance inferred from EM simulation of the synthesized impedance inverter (the CSRR-based cell plus the cascaded 35.35 Ω transmission line sections), and the ones inferred from circuit simulation are shown in Figure 4.14. The agreement is excellent in the LH region, where the model describes the structure to a very good approximation, and progressively degrades as frequency increases, as it is well known and expected. Nevertheless, the phase shift and the characteristic impedance at f_2 are reasonably close to the nominal values, and hence we do expect that the functionality of the power divider at f_2 is preserved. Figure 4.15 depicts the schematic and photograph of the divider (fabricated after cascading two output 50 Ω access lines for connector soldering) and the frequency response. It can be appreciated that optimum matching occurs at f_1 and slightly below f_2, for the reasons explained. Nevertheless, the functionality of the power divider covers both design frequencies. The discrepancy between the measured response and the target is not due to a failure of the ASM-based synthesis method, but it is due to the fact that the circuit model of the CSRR/gap-loaded line does not accurately describe the structure at high frequencies, including part of the RH band (notice that this does not occur with OSRR/OCSRR-based CRLH lines, where the model accurately describes the structure up to frequencies including the second −RH−band).

Since the use of the synthesis method tends to underestimate the upper matching frequency, one possibility to improve the power divider response is to design it by increasing the upper operating frequency with regard to the nominal value. Alternatively, optimization at the layout level can be carried out. Various additional examples

[15] This geometry may be used in applications where a relatively large gap capacitance is required.

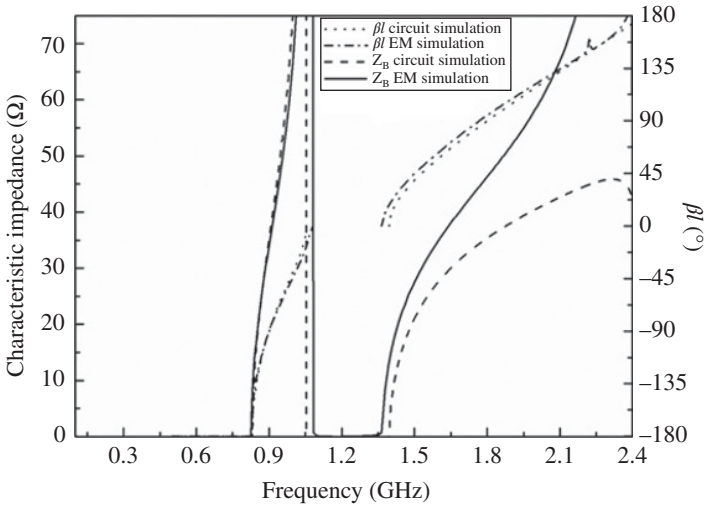

FIGURE 4.14 Comparison between the EM and circuit simulation corresponding to the characteristic impedance and electrical length of the designed dual-band impedance inverter described in the text. Reprinted with permission from Ref. [29]; copyright 2013 IEEE.

of power dividers based on the CSRR/gap-loaded lines can be found in Ref. [30]. In one of those dividers, a complementary spiral resonator (CSR) was used in order to reduce device size.

In both dual-band dividers, depicted in Figures 4.11 and 4.15, the upper band exhibits a wider bandwidth as compared to the first one. This is due to the softer variation of phase and characteristic impedance with frequency at the second design frequency. If both dividers are compared, the matching level and insertion loss at the design frequencies are of the same order. The OSRR/OCSRR-based divider exhibits broader bands, but splitters implemented with CSRRs exhibit a transmission zero that can be interesting for filtering purposes. Concerning size, despite that OSRRs and OCSRRs are electrically smaller than SRRs and CSRRs (this aspect was discussed in Chapter 3), the unit cell of the CSRR/gap-loaded CRLH line requires only one resonator, whereas three resonator stages are needed for the CRLH line based on the combination of OSRRs and OCSRRs. For this reason, dual-band components based on quarter wavelength impedance inverters implemented by means of CSRRs are typically electrically smaller as compared to those based on OSRR/OCSRR-based lines. On the other hand, the circuit model of OSRR/OCSRR provides very accurate results in a broader bandwidth as compared to the model of CSRR/gap-loaded lines. This eases circuit design for OSRR/OCSRR based CRLH lines. Nevertheless, a synthesis method has been developed to aid the design process in devices based on CSRRs, as detailed in Appendix H.

A dual-band branch line hybrid coupler based on CSRR/gap-loaded microstrip lines acting as quarter wavelength transmission lines was reported in Ref. [31].

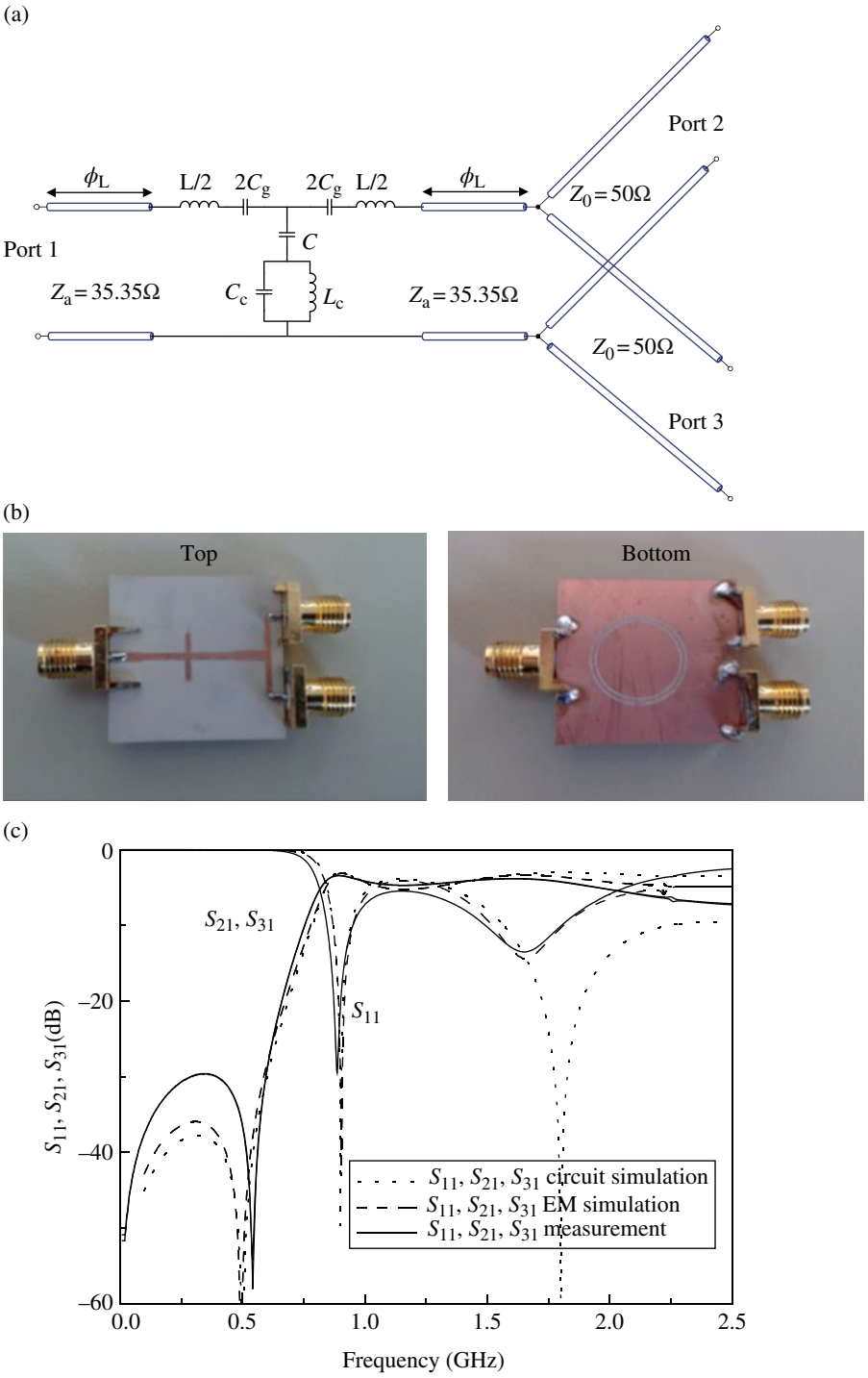

FIGURE 4.15 Schematic (a); photograph (b); and frequency response including circuit simulation, EM simulation, and measurement (c) of the designed and fabricated dual-band power divider. Reprinted with permission from Ref. [29]; copyright 2013 IEEE.

It is depicted in Figure 4.16 for completeness (the details of the design are given in Ref. [31]). The measured results show the dual-band performance around 0.90 GHz and 1.81 GHz (minimum return loss). The return loss, coupling, transmission, and isolation are 25.8 dB, 4.19 dB, 4.31 dB, and 21.5 dB at the first band, and 30.5 dB, 4.43 dB, 4.72 dB, and 17.69 dB at the second band. The measured phase balance is −93° and +92° at 0.90 GHz and 1.81 GHz, respectively. In terms of bandwidth and coupling at both operating frequencies, the device depicted in Figure 4.9 exhibits better performance. However, the coupler of Figure 4.16 is fully planar and electrically smaller (the size of the square is $0.19\lambda \times 0.20\lambda$, where λ is the guided wavelength at f_1).

Dual-Band Diplexer based on Branch Line Hybrid Couplers Although filters and diplexers will be considered in Section 4.2.3, an interesting application of dual-band hybrid couplers is reported here: the realization of a dual-band microwave diplexer operative at the mobile GSM frequency bands (GSM-850, DCS-1800) [32]. The schematic diagram of the dual-band diplexer is sketched in Figure 4.17 (the diplexer principle for single-band operation is reported in Ref. [33]). The port 1 of hybrid A is the transmitter (Tx) port, whereas ports 2 and 3 of the hybrid B are the receiver (Rx) and antenna ports, respectively. For dual-band operation, the hybrids and the band-stop filters must be designed to operate at the desired frequency bands. Indeed, the hybrids must cover both the transmitter and receiver frequencies at both bands, whereas the band-stop filters must be designed to efficiently reject the Rx signal and transmit the Tx signal for both GSM bands. Filters A and B have been designed to provide the central rejection frequencies at 0.89 and 1.73 GHz, respectively, that is the receiver signal frequencies. Transmitter frequencies are centered at 0.83 GHz for the lower band, and at 1.80 GHz for the upper band.

From the scattering matrix of the quadrature hybrid coupler (assuming that the pairs of isolated ports are ports 1–4 and 2–3), and considering that ports 1 and 4 of hybrid B are terminated by loads with identical reflection coefficient (the reflection coefficients of the two bandstop filters, Γ), it follows that the transmission from the antenna port to the receiver port is given by

$$S_{\text{antenna}-\text{Rx}} = j\Gamma \tag{4.35}$$

From (4.35), it is clear that if $|\Gamma| = 1$, the received signal at the antenna will be transmitted to the Rx port without any loss. This requires band-stop filters with high rejection and very low loss in the reflected signals at the two receiver band frequencies. From the analysis of the scattering matrix of the hybrids, and assuming that the filters only provide a certain phase shift at the transmit frequencies (which will be different for each frequency band), it follows that the power transmitted from the Tx port to the Rx port is null (isolated ports), whereas the injected power in the Tx port is totally transmitted to the antenna port according to:

$$S_{\text{Tx}-\text{antenna}} = e^{-j\left(\theta_{1,2}-\pi/2\right)} \tag{4.36}$$

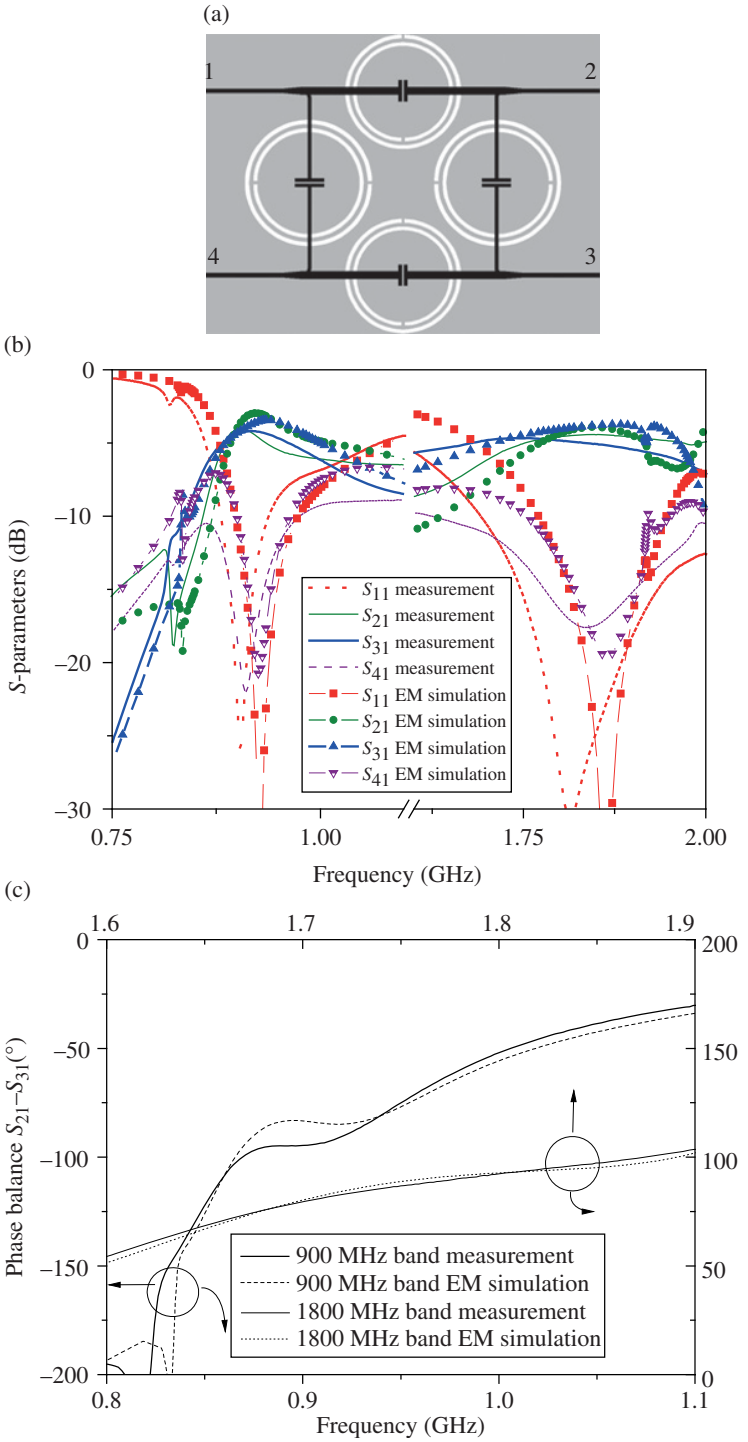

FIGURE 4.16 (a) Topology of a dual-band branch line hybrid coupler operating at the GSM frequencies $f_1 = 0.9$ GHz and $f_2 = 1.8$ GHz; (b) simulated and measured power splitting (S_{21}, S_{31}), matching (S_{11}) and isolation (S_{41}); and (c) simulated and measured phase response. For

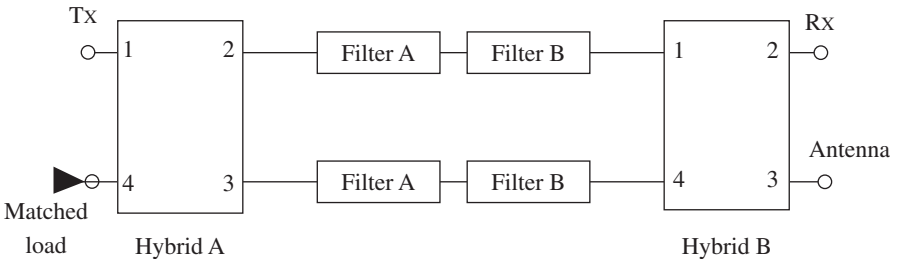

FIGURE 4.17 Schematic diagram of the dual-band diplexer.

It is clear that the signals at the antenna and Tx ports are identical except by certain phase shift, which depends on the phase shift introduced by the filters at the transmit frequencies of the two operating bands, θ_1 and θ_2.

The design of the dual-band branch-line hybrid couplers (implemented by means of CSRR/gap loaded lines) is described in Ref. [31]. The resulting devices are similar to that depicted in Figure 4.16. The dual-band band-stop filters were implemented by means of spiral resonators (SRs) coupled to the microstrip line connecting both hybrid couplers. To achieve dual-band operation, a pair of SRs was designed to provide rejection at the reception frequency of the lower band, whereas a second pair was tuned at the reception frequency of the upper band. The rejection filters could have been implemented by coupling other resonators to the line, but spirals provide small size and narrow band, as is required in this application (due to the proximity of the transmit frequencies). A photograph of the fabricated diplexer, including the dual-band hybrid couplers, the filters and the access lines, is depicted in Figure 4.18a.

The simulated and measured transmission coefficients between the different ports of the diplexer are depicted in Figure 4.18b and c. The simulated and experimental data are in good agreement, laying the receiver and transmitter frequencies within the desired GSM frequency bands. Concerning dimensions, the side length of the hybrids is as small as $\lambda/7$, λ being the guided wavelength at the lower frequency band (which is the limiting one in terms of size). Thanks to the small size of the hybrids, plus the miniature spirals used as rejection filters, the overall dimensions of the proposed prototype dual-band diplexer are small.

FIGURE 4.16 (*Continued*) the 35.35 Ω impedance inverters (lines between ports 1–2 and 3–4), the dimensions are internal radius $r = 7.53$ mm, ring width $c = 0.42$ mm, separation between rings $d = 0.55$ mm, width of the host line $W = 1.00$ mm, gap separation $s = 0.27$ mm, and gap width $W_g = 2.77$ mm. For the 50 Ω impedance inverters (lines between ports 1–4 and 2–3) $r = 8.27$ mm, $c = 0.46$ mm, $d = 0.60$ mm, $W = 0.46$ mm, $s = 0.27$ mm, and $W_g = 3.77$ mm. The device was fabricated on the *Rogers RO3010* substrate with thickness $h = 0.635$ mm and dielectric constant $\varepsilon_r = 10.2$. Reprinted with permission from Ref. [31]; copyright 2008 IEEE.

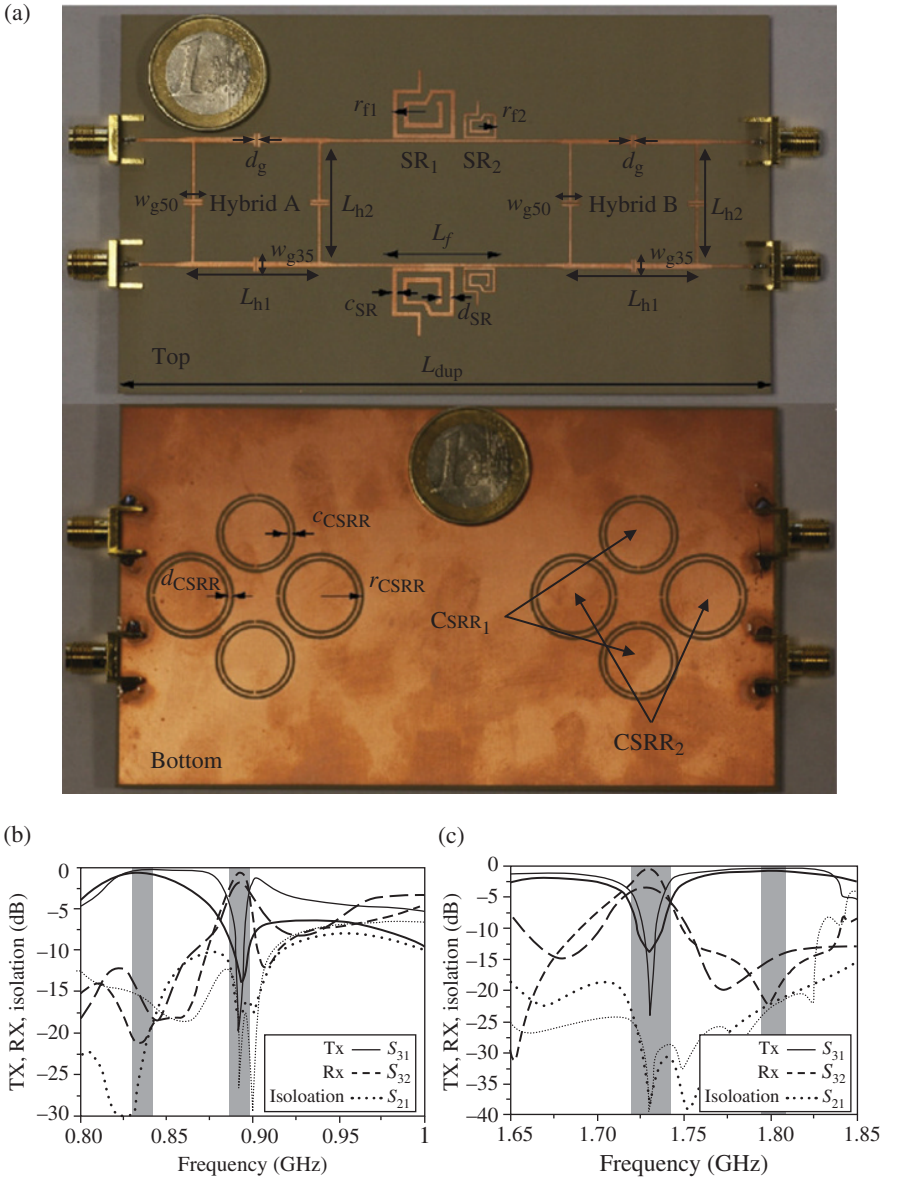

FIGURE 4.18 Photograph of the fabricated diplexer (a) and comparison between simulated (thin line) and measured (thick line) transmission characteristics for the fabricated diplexer at the lower (b) and upper (c) GSM bands. Dimensions are $L_{dup} = 124$ mm, $L_f = 21.44$ mm, $r_{CSRR1} = 7.4$ mm, $r_{CSRR2} = 7.9$ mm (external radius of the CSRR), $c_{CSRR1} = c_{CSRR2} = 0.5$ mm (width of the rings), $d_{CSRR1} = d_{CSRR2} = 0.5$ mm (distance between rings), $r_{f1} = 6$ mm, $r_{f2} = 3$ mm, $c_{SR1} = 0.9$ mm, $c_{SR2} = 0.5$ mm (width of the spirals), $d_{SR1} = 1.1$ mm, and $d_{SR2} = 0.6$ mm (distance between loops of the spiral). The gap separation is $d_g = 0.27$ mm and gap widths are $w_{35} = 2.77$ mm and $w_{50} = 3.77$ mm. Length (L_{h1}, L_{h2}) of the artificial lines constituting the hybrids are 18 mm and 17.6 mm for the 35 Ω impedance and 50 Ω impedance lines, respectively. The considered substrate is the *Rogers RO3010* substrate with measured dielectric constant $\varepsilon_r = 11.2$ and thickness $h = 635$ μm. Reprinted with permission from Ref. [32]; copyright 2011 Springer.

4.2.2.3 Quad-Band Devices based on Extended CRLH Transmission Lines The order-4 CRLH transmission line T-circuit model depicted in Figure 3.25c (also known as extended CRLH—E-CRLH—line) is useful for the implementation of quad-band components based on quarter wavelength transmission lines. For multiband functionality Equations 4.28 can be generalized as

$$\chi_{\mathrm{s}}(\omega_n) = (-1)^n Z_{\mathrm{A}} \tag{4.37a}$$

$$\chi_{\mathrm{p}}(\omega_n) = (-1)^{n+1} Z_{\mathrm{A}} \tag{4.37b}$$

where n is the frequency index (i.e., $n = 1, 2, 3, 4$ for a quad-band device). In (4.37), it has been assumed that the characteristic impedance of the quarter wavelength transmission lines is identical at all the operating frequencies and given by Z_{A}. For quad-band functionality, expressions (4.37) provide eight equations that univocally determine the eight independent reactive elements of the circuit model of Figure 3.25c.

For the synthesis of the extended CRLH line model of Figure 3.25c in fully planar technology, both CPW [34] and microstrip [35] host lines have been considered. Let us consider the implementation of a quad-band impedance inverter at the GSM ($f_1 = 0.9$ GHz, $f_4 = 1.8$ GHz) and GPS ($f_2 = 1.17$ GHz, $f_3 = 1.57$ GHz) frequency bands in CPW technology by using OSRRs and OCSRRs. The characteristic impedance is forced to be $Z_{\mathrm{A}} = 35.35\ \Omega$ at these frequencies in order to subsequently implement a quad-band Y-junction power divider. The electrical length of the structure is set to $-90°$ (LH bands) at the odd frequencies and to $+90°$ (RH bands) at the even frequencies. The values of the circuit model corresponding to Figure 3.25c that satisfy these conditions are $L_{\mathrm{hs}} = 22.458$ nH, $C_{\mathrm{hs}} = 0.766$ pF, $L_{\mathrm{hp}} = 0.883$ nH, $C_{\mathrm{hp}} = 14.06$ pF, $L_{\mathrm{vs}} = 8.785$ nH, $C_{\mathrm{vs}} = 1.414$ pF, $L_{\mathrm{vp}} = 1.915$ nH, and $C_{\mathrm{vp}} = 8.986$ pF. With these line parameters and frequencies, the resulting reactive element values are reasonable for their implementation by means of OSRRs or OCSRRs, with exception of the parallel resonators of the series branch, that are realized by parallel connecting a capacitive patch and a meander inductor (the topology of the final quad-band impedance inverter is depicted in Fig. 4.19a).

To a first-order approximation, the structure of Figure 4.19a can be described by the canonical order-4 E-CRLH model shown in Figure 3.25c. However, for an accurate description, line parasitics must be taken into account, as it was done in Section "Dual-Band Devices Based on Fully Planar CRLH Lines" for the description of dual-band impedance inverters implemented by means of OSRRs and OCSRRs. Thus, a more accurate circuit model of the quad-band CRLH line of Figure 4.19a is depicted in Figure 4.19b. For the determination of the layout, a procedure similar to that reported in Section "Dual-Band Devices Based on Fully Planar CRLH Lines" in reference to dual-band CRLH lines is applied. Once the element values of the canonical circuit model (Fig. 3.25c) are known, the layout of each section is determined so that the element parameters (inferred from curve fitting) of the resonators coincide with those of the E-CRLH model of Figure 3.25c. This procedure also provides the values of the parasitic elements.

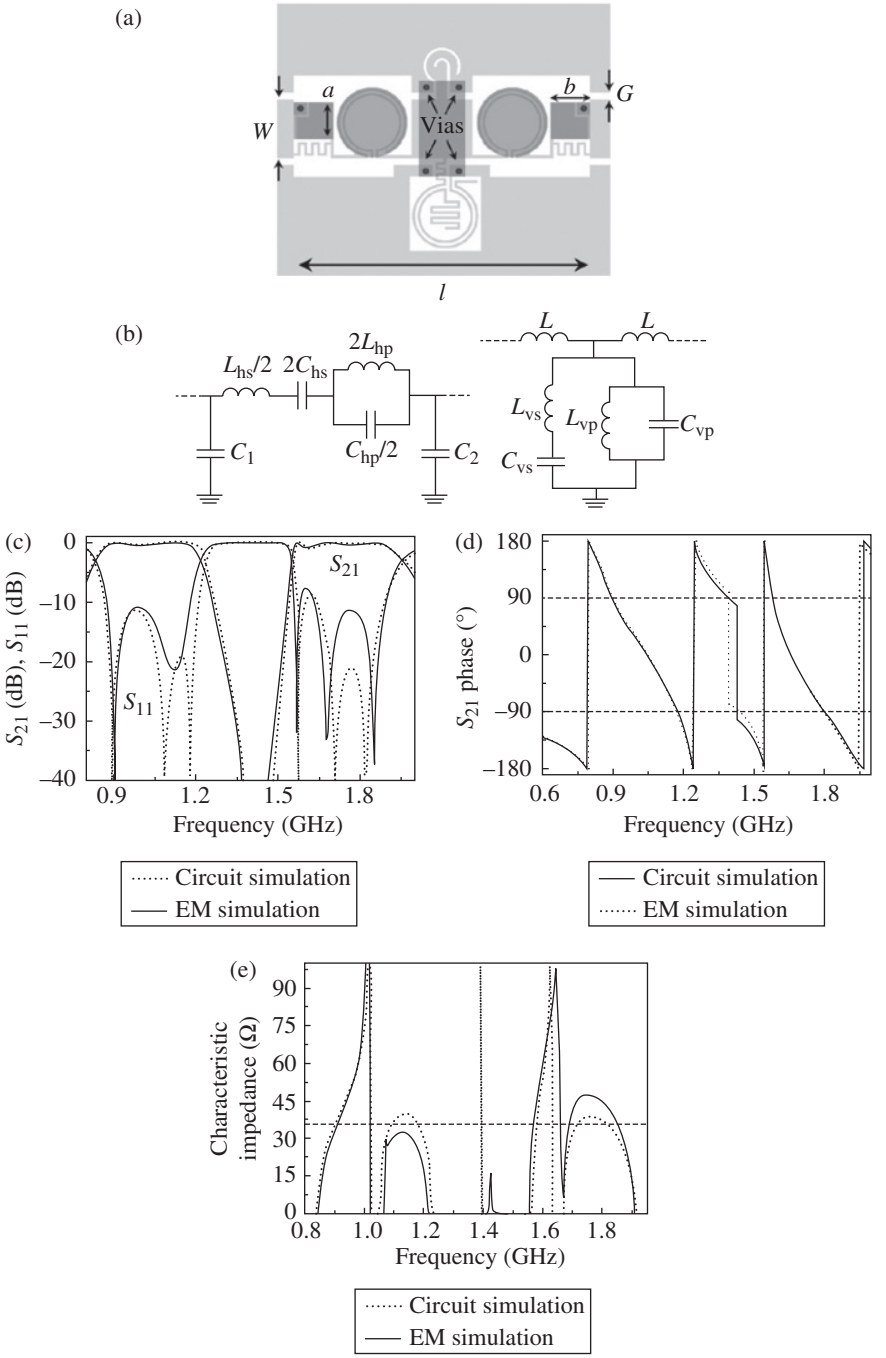

FIGURE 4.19 Topology (a), circuit models of the series and shunt branches including parasitics (b), magnitude of the frequency response (c), phase response (d), and characteristic impedance (e) of the designed quad-band CPW impedance inverter. The dimensions are

The next step is to tune the resonator values in the circuit model of Figure 4.19b until the required values of impedance and phase at the operating frequencies are obtained (this is simple and fast because this is done at the circuit level). Finally, the topology of the different resonators is modified at the layout level in order to fit the EM simulation of each section of the structure to the circuit simulation. This is simple because the variation of the element values in the tuning procedure of the previous step gives us the guide to modify the geometry of the different resonators (tuning the layout does not affect substantially the effects of the parasitics). With this procedure, the layout of the whole structure that provides the required values of characteristic impedance and phase at the operating frequencies is directly obtained (additional tuning or optimization is not required). The layout of the quad-band impedance inverter obtained by this procedure is the one depicted in Figure 4.19a. The electrical size of the device is $0.105\lambda \times 0.074\lambda$, λ being the guided wavelength at the lower frequency band (900 MHz), and the considered substrate is the *Rogers RO3010* with thickness $h = 0.254$ mm, and measured dielectric constant $\varepsilon_r = 11.2$.

The simulated S-parameters of the designed impedance inverter, using port impedances of 35.35 Ω, are depicted in Figure 4.19c. Both the EM (without losses) and circuit simulation are included in the figure. The simulated phase response and characteristic impedance of the designed quad-band impedance inverter are depicted in Figure 4.19d and e, respectively. The agreement between the EM and circuit simulation is good, and the required functionality of the impedance inverter is achieved at the whole operating frequencies to a good approximation. This validates the model of the quad-band CRLH structure implemented by means of OSRRs and OCSRR in CPW technology that includes parasitic elements (Fig. 4.19b).

In order to implement a Y-junction power divider, two 50 Ω access lines are cascaded to the output port of the impedance inverter and a 50 Ω access line is cascaded to the input port. The fabricated quad-band power divider is shown in Figure 4.20. The simulated and measured power division and matching, also depicted in the figure, indicate that the desired functionality at the design frequencies is achieved, with a matching level better than −10 dB at the whole frequencies.

FIGURE 4.19 (*Continued*) $W = 4.5$ mm, $G = 0.524$ mm, and $b = 3$ mm. The width and separation of all the meanders is of 0.2 mm, $a = 2.8$ mm, and $l = 22.5$ mm; for the series connected OSRRs, $r_{ext} = 2.6$ mm, $c = 0.2$ mm, and $d = 0.15$ mm; for the shunt connected OSRR, $r_{ext} = 2.5$ mm, $c = 0.2$ mm, and $d = 0.2$ mm; for the OCSRR, $r_{ext} = 1.4$ mm, $c = 0.2$ mm, and $d = 0.6$ mm. r_{ext}, c, and d are the external radius, width, and separation of the rings, respectively. The element values corresponding to the circuit model shown in (b) are $L_{hs} = 21$ nH, $C_{hs} = 0.775$ pF, $L_{hp} = 0.88$ nH, $C_{hp} = 13.96$ pF, $L_{vs} = 8.8$ nH, $C_{vs} = 1.41$ pF, $L_{vp} = 1.95$ nH, $C_{vp} = 8.3$ pF, $C_1 = 0.41$ pF, $C_2 = 0.22$ pF, and $L = 0.4$ nH. Notice that the phase of S_{21} exhibits opposite sign to the electrical length. Reprinted with permission from Ref. [34]; copyright 2010 IEEE.

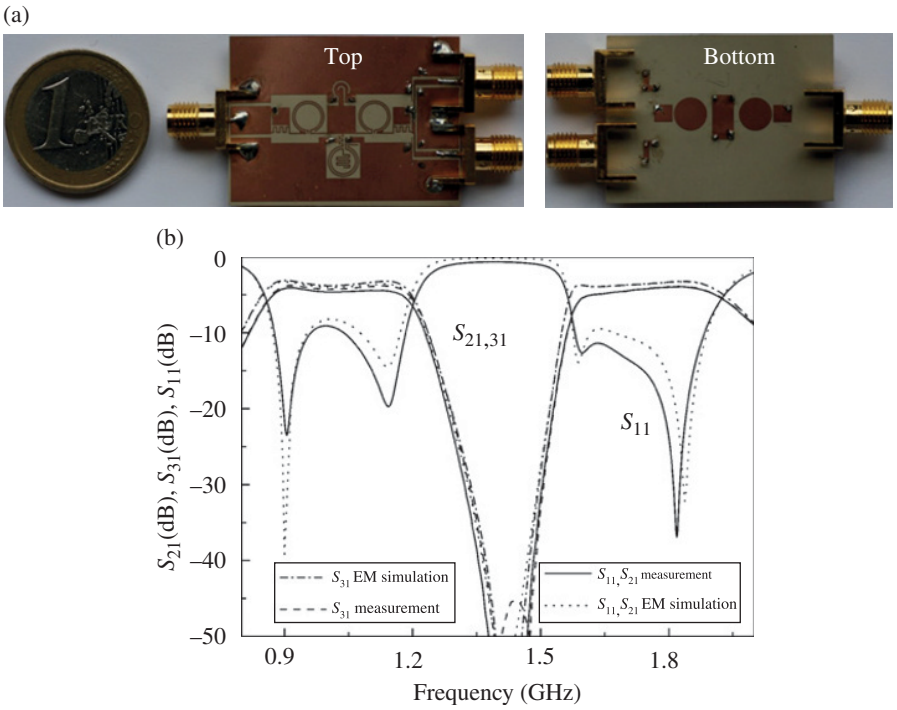

FIGURE 4.20 Photograph of the fabricated quad-band Y-junction power divider implemented by means of the inverter of Figure 4.19 (a), and simulated and measured power division and matching (b). Reprinted with permission from Ref. [34]; copyright 2010 IEEE.

The implementation of fully planar quad-band CRLH transmission lines in microstrip technology is reported in Ref. [35], and applied to the design of power splitters and branch-line hybrid couplers. However, in microstrip technology the series-connected OSRRs can no longer be described by a simple model (as it was shown in Chapter 3). Moreover, the typical required values of resonator inductances and capacitances further limit the implementation of such resonators by means of OSRRs and OCSRRs, as compared to CPW technology. Thus, the microstrip quad-band CRLH lines of Ref. [35] are implemented through a combination of OCSRRs (for the parallel resonator of the shunt branch), meander inductors, patch capacitances and interdigital capacitances. The quad-band power divider reported in Ref. [35] exhibits comparable performance to that of Figure 4.20. The quad-band branch line hybrid coupler also reported in Ref. [35] is a complex structure with tiny details at the layout level. Thus, losses degrade somehow device performance, especially at the third operating frequency, where the insertion loss is substantially higher than the ideal value (3 dB). Nevertheless, the measured matching, isolation, and phase balance are reasonable considering the complexity of the circuit layout (see Ref. [35] for further details).

Fully planar order-4 E-CRLH microstrip lines were also reported in Ref. [36], but the agreement between the circuit model and the EM response of the designed structure is very limited. On the other hand, quad-band Wilkinson power dividers have been implemented in microstrip technology by combining semilumped and lumped elements [37]. It is also remarkable that order-4 CRLH lines can also be applied to the implementation of triband components. However, in this case there is an excess of elements, and such triband components are preferably implemented by means of order-3 CRLH transmission lines, such as the double-Lorentz metamaterial transmission line reported in Ref. [38].

To end this subsection, it is important to clarify that dual-band and multiband components are not exclusive products of CRLH transmission lines. There are many other approaches that either exploit transmission line loading (this also enhances the number of parameters of the constitutive transmission lines) or make use of complex structures combining transmission line and stubs in order to satisfy the required functionality at several frequencies simultaneously. In many of the reported multiband devices, the performance is very satisfactory, but device dimensions are usually relatively large, as compared to the typical dimensions resulting by applying the CRLH transmission line concept. As illustrative examples of dual-band components based on other approaches, the author suggests the papers [39, 40] and references therein (a complete list would be too large for inclusion in this book).

4.2.3 Filters and Diplexers

Metamaterial transmission lines exhibit pass bands and stop bands, and therefore they are filtering structures by nature. The purpose of this subsection is to present some of the main approaches for the implementation of different type of filters (narrowband, wideband, etc.) and filter responses (stopband, bandpass, lowpass, and highpass), including those strategies that lead to small filter size and spurious suppression. Several examples will be reported, including narrow and wideband filters, microwave diplexers, and multifunctional filters, among others. It is impossible to provide a wide overview of metamaterial-based filters in this subsection. Therefore, an extensive list of references on this topic is provided. This includes a review paper [41], where some of the approaches reported here are succinctly considered. The topic of tunable and reconfigurable filters will be studied in Chapter 5, devoted to reconfigurable, tunable, and nonlinear artificial transmission lines.

4.2.3.1 Stopband Filters based on SRR- and CSRR-Loaded Lines[16] Stopband filters are of interest in RF/microwave engineering for the suppression of undesired responses or interfering signals. As it was studied in Chapter 3, SRR-loaded CPWs and CSRR-loaded microstrip lines are single negative artificial transmission lines

[16] The filters reported in this subsection are indeed based on transmission lines with metamaterial loading. Namely, the functionality of these filters is based on a resonance phenomenon (rather than on dispersion and impedance engineering), and the considered structures are not based on CRLH lines. However, such filters are included here (rather than in Section 4.3) for thematic coherence. This also applies to Section 4.2.3.2.

able to inhibit signal propagation in the vicinity of particle resonance. In periodic structures, strong rejection can be achieved if a sufficient number of cascaded resonators is considered. However, the typical rejection bandwidths of these filtering structures are small due to the typical quality factors of SRRs and CSRRs. Bandwidth can be enhanced by cascading tightly coupled SRRs or CSRRs, as it was discussed in Chapter 3. However this approach is not very effective since the coupling level is limited in practice. To overcome this limitation, we may take advantage of the high reflectivity of the considered particles, and cascade several resonators tuned at slightly different frequencies over the frequency band of interest. The resulting non-periodic structures may provide wide stop bands if the number of cascaded resonators is high enough.

Frequency tuning can be achieved either by scaling up (or down) the dimensions of the SRRs (or CSRRs) or by increasing (or decreasing) their radius. This approach has been driven to practice in microstrip and CPW technology using CSRRs and SRRs [42–44]. As illustrative examples, two stopband filters are reported. The first one is a multiple tuned SRR-loaded CPW stopband filter with five SRR pairs (Fig. 4.21). Tuning was implemented by increasing the inner radius of the SRRs in 0.05 mm step increments and leaving unaltered c and d (as compared to the SRR geometry of Fig 3.31). The simulated and measured frequency responses (also depicted in Fig. 4.21) show that the rejected band broadens toward lower frequencies. This is expected since an increment of r has the effect of decreasing the resonant frequency of SRRs. The second example is a multiple tuned CSRR-loaded microstrip line (Fig. 4.22), where rectangular-shaped resonators are etched in the ground plane (they can also be etched in the central strip [45]). The measured frequency response of this structure, which is also depicted in Figure 4.22, reveals that rejection above 20 dB can be achieved within a 25% fractional bandwidth.

4.2.3.2 Spurious Suppression in Distributed Filters The filtering structures of the previous subsection can be applied to the elimination of spurious bands in distributed filters. Such undesired bands can seriously degrade filter performance, and may be critical in several applications where high rejection bandwidths are required. For instance, in parallel-coupled line bandpass filters, the first spurious band appears at twice the filter central frequency as consequence of the different phase velocities of the even and odd modes of the coupled-line sections. The rejection of spurious bands has been a subject of interest in microwave engineering for years. Specifically, in coupled line filters, several approaches based on modified structures, aimed to obtain equal modal phase velocities, have been proposed as a means to improve the out-of-band filter performance [46–49]. It was also reported in Chapter 2 that EBG-based structures embedded in the coupled line sections efficiently suppress the spurious bands in coupled line bandpass filters. This approach is very effective and can be applied to many other filter types (see, e.g., the filter depicted in Fig. 2.36). However, EBG structures scale with frequency and may be excessively large for the suppression of spurious bands in compact planar filters.

An alternative approach for the elimination of spurious frequency bands in distributed filters is the use of SRRs or CSRRs. Their small electrical size, rejection

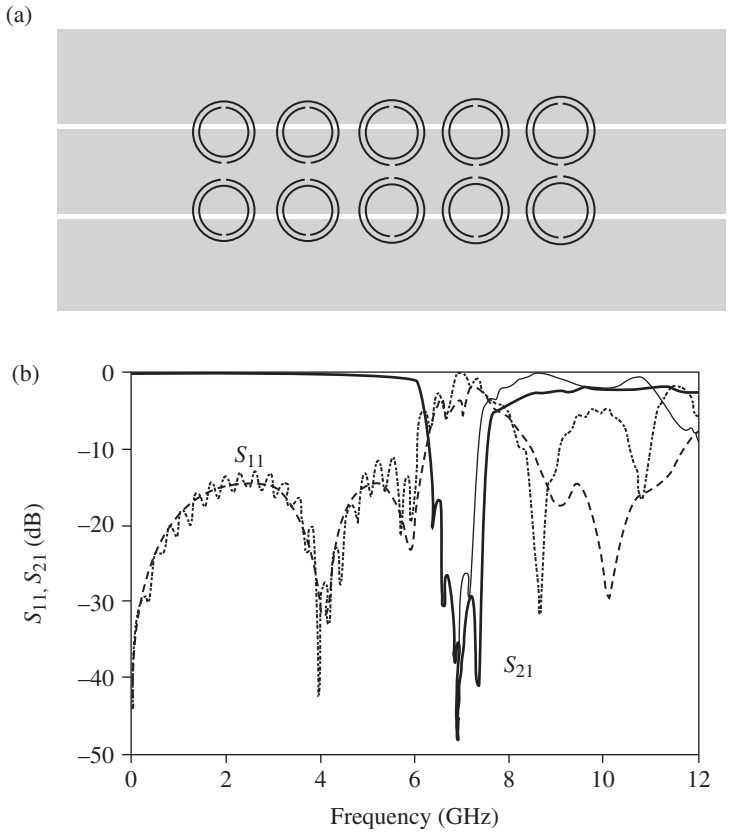

FIGURE 4.21 Layout (a), simulated (thin line) and measured (bold line) frequency responses (b) of the multituned SRR-based CPW stopband filter. The length of the active region is 4 cm. The dimensions of the smallest SRRs are $c = d = 0.2$ mm and internal radius $r = 1.3$ mm. For the other SRRs, r was incremented in 0.05 mm steps, whilst c and d were left unaltered. The structure was fabricated on the *Arlon* 250-LX-0193-43-11 substrate ($\varepsilon_r = 2.43$, thickness $h =$ 0.49 mm). Reprinted with permission from Ref. [42]; copyright 2003 IEEE.

efficiency, and versatility (stopband filters based on these particles have been demonstrated in both microstrip and CPW technology [42–44]) make these resonant elements very attractive to achieve effective spurious suppression with minimum area increase. As occurs with EBGs, the main advantage of the approach is the fact that SRRs and CSRRs can be embedded within the filter active region. Namely, it is not necessary to cascade the SRRs or the CSRRs at the input or output access lines (as it was done in the first reported structure using this concept [50]). This represents an optimum design in terms of area saving. To illustrate the efficiency of SRRs and CSRRs for the elimination of spurious bands and its versatility, a parallel coupled line bandpass filter implemented in microstrip technology is reported [44]. The layout of the device, a third-order Butterworth bandpass filter with a central frequency

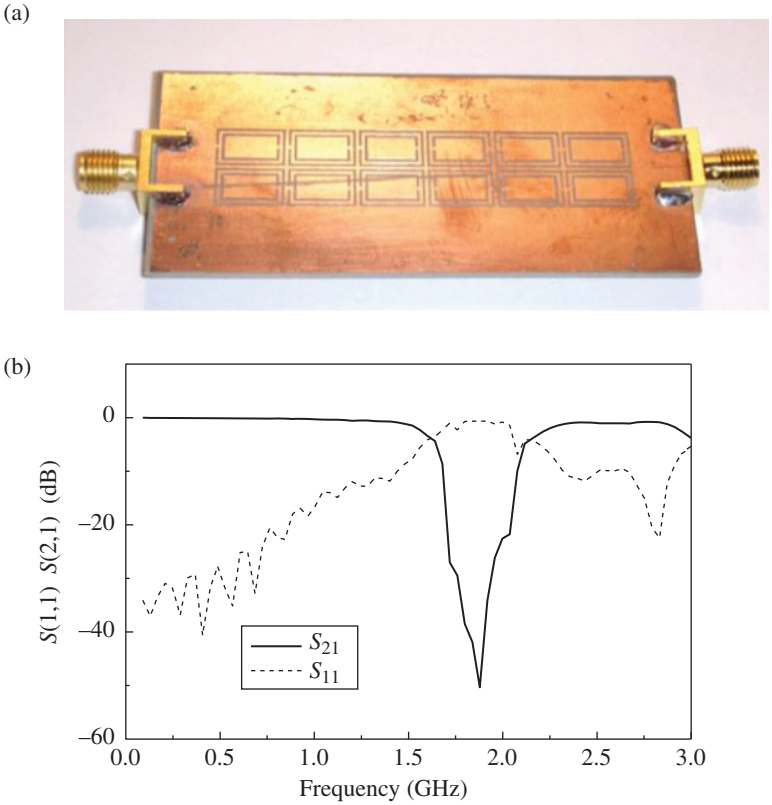

FIGURE 4.22 Microstrip line with square-shaped CSRR etched in the ground plane (a) and measured frequency response (b). $c = d = 0.4$ mm while the external edges of the CSRRs were tuned in the vicinity of 9.4 mm × 5.8 mm. The structure was fabricated on the *Rogers RO3010* substrate ($\varepsilon_r = 10.2$, $h = 1.27$ mm). Reprinted with permission from Ref. [44]; copyright 2005 IEEE.

of $f_o = 2.4$ GHz and 10% fractional bandwidth, is depicted in Figure 4.23. Rectangular SRRs are etched adjacent to the coupled lines in order to reject the first and second spurious bands. The multiple tuning procedure explained in the previous subsection was used. The smaller rings (etched in the central stages) are responsible for the rejection of the second spurious band, whereas the first undesired band is rejected by the action of the larger SRRs, which are allocated in the first and forth filter stages. The simulated and measured frequency responses of this device are also represented in Figure 4.23. In comparison to the conventional filter, the first spurious band is rejected with attenuation levels near 40 dB, while insertion losses in the second band are clearly above 20 dB. This efficiency can be attributed to the significant number of SRRs pairs distributed along the device, which is possible by virtue of their small electrical size. It is also worth mentioning that the use of square or rectangular-shaped SRRs enhances the coupling between line and rings, and this allows for further

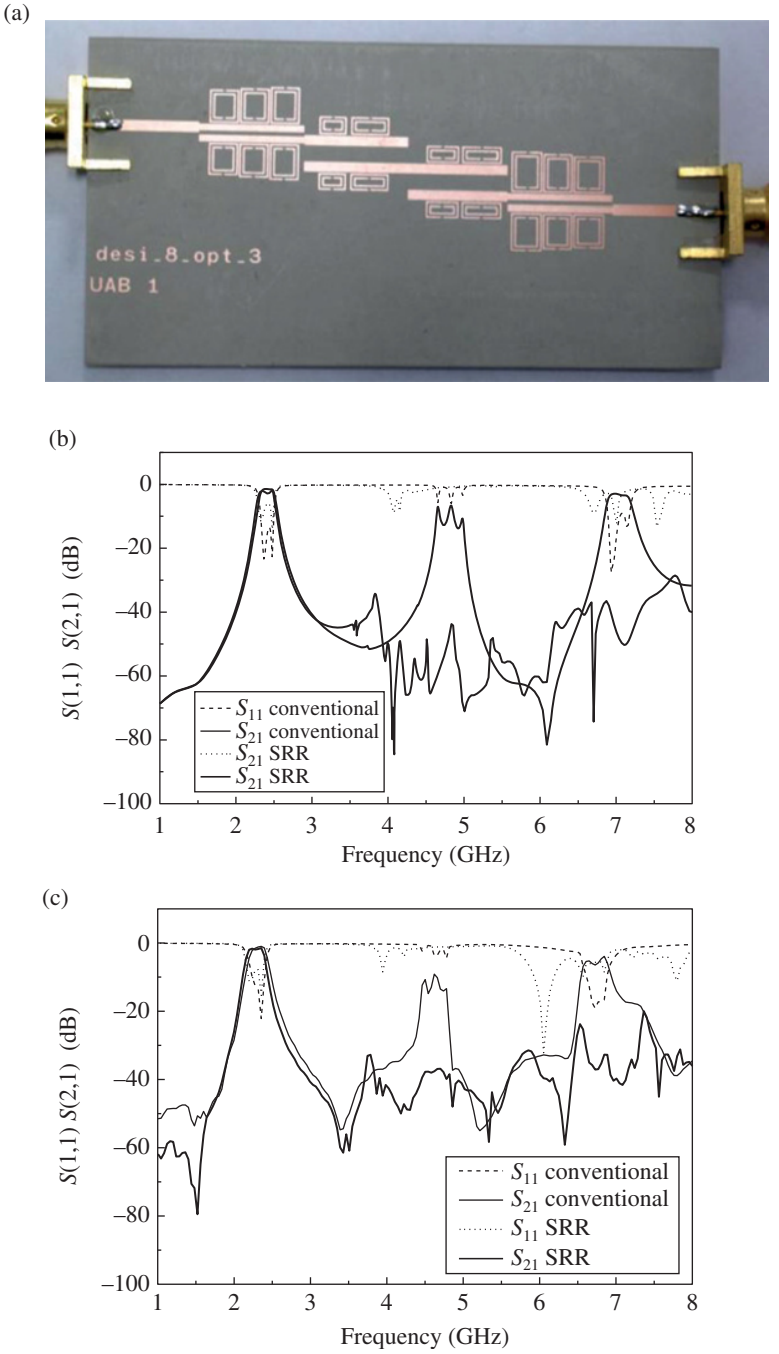

FIGURE 4.23 (a) Coupled-line microstrip bandpass filter loaded with SRRs for spurious suppression, (b) simulated frequency response compared to that obtained in the device without SRRs, and (c) measured frequency responses. The device was fabricated on the *Rogers RO3010* substrate (thickness $h = 1.27$ mm, dielectric constant $\varepsilon_r = 10.2$). Reprinted with permission from Ref. [44]; copyright 2005 IEEE.

rejection levels, as compared to circular SRRs. This strategy has also been applied (using CSRRs) to the elimination of spurious bands in CPW coupled line bandpass filters [44] and stepped impedance lowpass filters [51].

4.2.3.3 Narrow Band Bandpass Filters and Diplexers Based on Alternate Right-/Left-Handed Unit Cells The SRR/strip-loaded CPW transmission lines and the CSRR/gap-loaded microstrip CRLH transmission lines discussed in Chapter 3 can be used for the implementation of compact bandpass filters. By balancing these lines, filters with wide bands result, as will be discussed later. Conversely, if these structures are unbalanced the first, and narrow, LH band can in principle be exploited for narrow band filtering applications. The presence of a transmission zero to the left of the LH band provides good frequency selectivity at the lower edge of the transmission band. However, the frequency selectivity at the upper stop band is poor. To overcome this limitation, one strategy is to combine the LH structures based on SRRs or CSRRs with RH cells (also based on SRRs or CSRRs), the latter exhibiting a transmission zero above the RH band. Obviously, it is necessary to tune the cells in order to exhibit the same transmission band. This approach has been demonstrated to be useful for the implementation of very compact narrow band bandpass filters and diplexers in CPW and microstrip technology [52–56].

In CPW technology, an RH transmission band with a transmission zero to the right of this band can be achieved by combing the pairs of SRRs with series gaps. The equivalent circuit model of such cell is depicted in Figure 4.24a. According to this model, signal transmission occurs in that frequency region where the reactance of the series branch is positive (inductive), and this takes place in a narrow band before the resonance frequency of the SRRs (transmission zero frequency).

In microstrip technology, narrow RH transmission bands are expected in structures where the CSRRs are combined with shunt connected inductors. According to the model of this RH cell (Fig. 4.24b), the shunt reactance must be negative (capacitive) in the transmission bands, and this occurs to the left of the transmission zero frequency.

As illustrative examples of this alternate right-/left-handed (ARLH) approach, a narrow band CPW bandpass filter at S-band and a microstrip diplexer are reported.

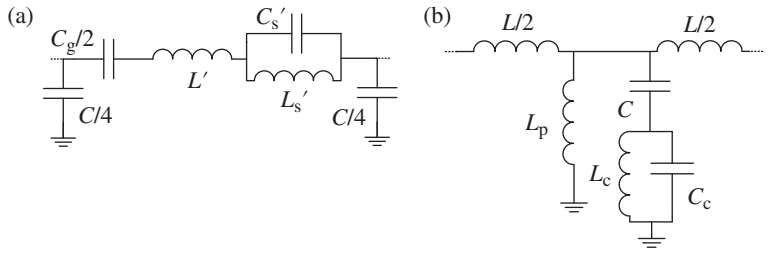

FIGURE 4.24 Lumped-element equivalent circuit for the SRR/gap-loaded CPW (a) and CSRR/strip-loaded microstrip line. C_g is the capacitance of the series gap and L_p is the inductance of the grounded strip. In (a), the magnetic wall concept is applied.

The S-band filter [55], inspired by the first implementation of the ARLH concept [52], was designed by cascading two unit cells: an LH SRR/strip and an RH SRR/gap combination (Fig. 4.25). The central filter frequency is $f_o = 2.4$ GHz. Filter length (active region) is as small as 22.5 mm, that is, five times smaller than the wavelength at f_o. The frequency response of the filter exhibits good frequency selectivity by virtue of the transmission zeros present at both sides of the pass band. The measured average

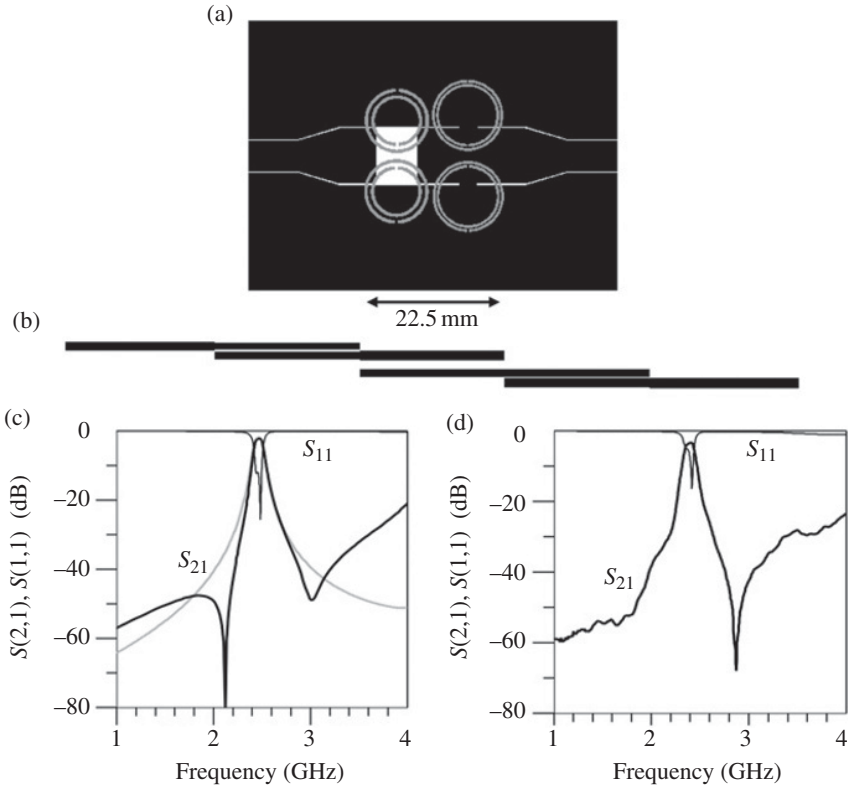

FIGURE 4.25 (a) Layout of the S-band filter based on the ARLH concept. The dimensions of the SRRs pairs corresponding to the strip and gap stages are $r = 5.2$ mm, $c = 0.44$ mm, $d = 0.22$ mm, and $r = 4.1$ mm, $c = d = 0.55$ mm, respectively. Strip and gap dimensions have been set to $w_w = 2.8$ mm and $l_g = 6.6$ mm, respectively. The host CPW is a 50 Ω line with a wide strip ($W = 10$mm) in order to accommodate the rings. Since the separation between ground planes is wider than the dimensions of the connectors in use, it was necessary to cascade taper transitions at the input and output ports to allow for connectors insertion. The length of the active device region is 22.5 mm. The considered substrate is the *Arlon 250-LX-0193-43-11* with dielectric constant $\varepsilon_r = 2.43$, and thickness $h = 0.49$ mm. (b) Layout of a conventional microstrip parallel-coupled line bandpass filter with comparable performance, drawn to scale. (c) Simulated frequency response for the S-band filter compared to that of the coupled line bandpass filter (insertion loss in gray line). (d) Measured frequency response of the S-band filter. Reprinted with permission from Ref. [55]; copyright 2005 John Wiley.

slope of the upper and lower transition bands is 150 dB/GHz and 125 dB/GHz, respectively. A conventional coupled line bandpass filter (in microstrip technology) exhibiting similar central frequency, bandwidth, and selectivity is also depicted in Figure 4.25 for comparison purposes. The active region of the coupled line bandpass filter is substantially longer (63.6 mm). Thus, the ARLH transmission line concept has been revealed to be an efficient approach for size reduction in narrow band bandpass filter. Limitations of this approach are the difficulty in controlling bandwidth and selectivity, and the sensitivity of the filter response with SRR dimensions (it was found that variations of the SRR geometry due to fabrication related tolerances degrade in-band losses).

For the implementation of the microwave diplexer an Rx and a Tx filter is required. The configuration of the considered diplexer is shown in Figure 4.26, where the Rx and Tx filters are cascaded at the output ports of a Y-junction. The main relevant parameters representative of diplexer performance are in-band looses for the Tx and Rx channels (which should be as small as possible) and Rx/Tx isolation (which should be high to avoid interfering signals between the Rx and Tx channels). A prototype device operative in the 2.4–3.0 GHz frequency band is depicted in Figure 4.27a [56]. The Tx and Rx filters (implemented by means of CSRR-based ARLH microstrip lines[17]) have been designed to provide pass bands centered at 2.4 and 3.0 GHz, respectively, with absolute bandwidths of 0.25 GHz (namely 10.3% and 8% fractional bandwidths for transmission and reception). Figure 4.27b depicts the measured transmission coefficient for the Tx and Rx filters (i.e., S_{21} and S_{31}, respectively), as well as the measured Rx/Tx isolation (S_{32}). In-band losses lower than 2 dB are measured for each filter, while return losses (also represented in Fig. 4.27b) are better than 10 dB. The frequency response of the filters is quite symmetric and the measured isolation between ports 2 and 3 is in the vicinity of 40 dB. Remarkable are also the dimensions of the diplexer (see the region indicated in Fig. 4.27a), which are as small as 29.8 mm × 16.3 mm (namely $0.63\lambda \times 0.34\lambda$, λ being the signal wavelength at the Tx frequency) thanks to the compact resonators employed (more details on diplexer design are given in Ref. [56]).

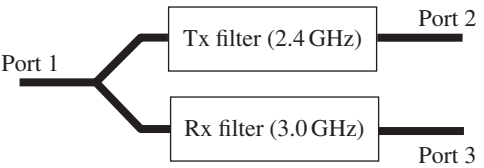

FIGURE 4.26 Structure of the diplexer.

[17] Notice that in the RH sections of the Rx and Tx filters, two CSRRs are used. The reason is the moderate bandwidth required for each filter. To achieve such bandwidths, it is necessary to implement unit cells also with moderate bandwidths. For the forward sections, this is more easily achieved by using two CSRRs, rather than only one, as it was pointed out in Ref. [53].

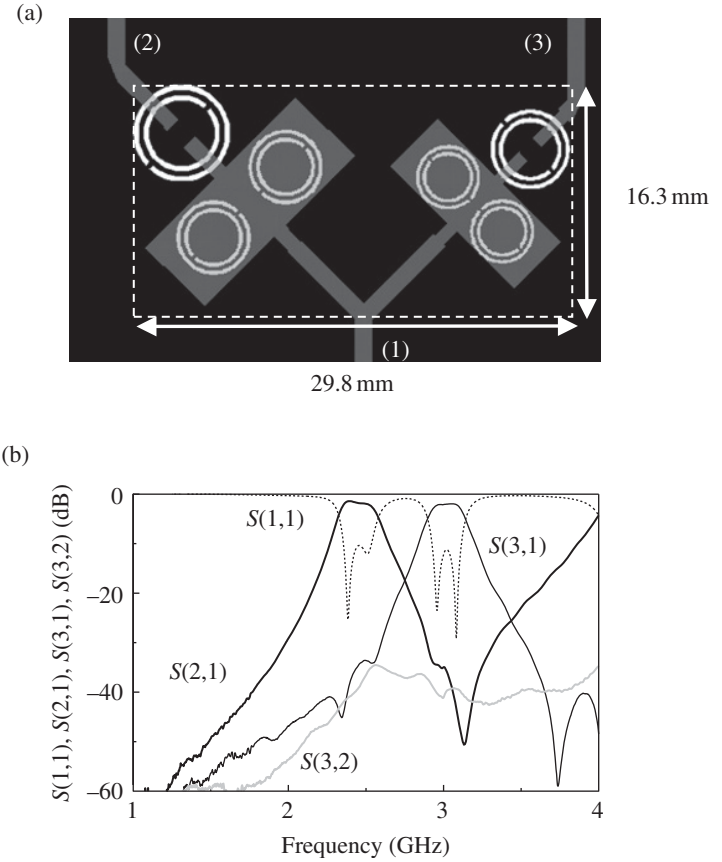

FIGURE 4.27 (a) Topology of the fabricated ARLH microstrip diplexer and (b) measured frequency response. The upper metal level is depicted in gray, whereas the lower metal is drawn in black. Gap spacing is 1.33 mm and 1.67 mm for the Rx and Tx filters respectively, whereas shunt strip dimensions are 4.54 mm × 11.9 mm and 5.70 mm × 14.48 mm. External CSRR radius are 2.18 mm, 2.73 mm, 2.56 mm, and 3.27 mm for the Rx (first stage), Rx (second stage), Tx (first stage), and Tx (second stage), respectively. The shunt strips are grounded through vias. The structure was implemented on the *Rogers RO3010* substrate (thickness $h = 1.27$ mm, dielectric constant $\varepsilon_r = 10.2$). Reprinted with permission from Ref. [56]; copyright 2005 IET.

4.2.3.4 Compact Bandpass Filters based on the Hybrid Approach Although the filters based on the ARLH transmission line concept are electrically small and provide moderate or narrow bands with symmetric responses and high selectivity, the controllability of the filter response is not simple. In this subsection, a methodology for the design of moderate and narrow band bandpass filters subjected to specifications (with the possibility to synthesize standard filter responses such as Butterworth and

Chebyshev[18]) is presented [57]. Such filters are based on the hybrid model of metamaterial transmission lines presented in Chapter 3. Since these structures can be designed to exhibit a transmission zero above the first LH band, the out-of-band performance of the filters can be improved through the suppression of undesired harmonic bands.

Design Methodology The microstrip filters proposed in this subsection are planar structures that can be modeled by the circuit of Figure 4.28a, which consists of a cascade of admittance inverters (with normalized admittance $\bar{J} = 1$) alternating with shunt connected resonators tuned at the central frequency of the filter band, f_o [33, 58]. This circuit is inferred from the lowpass filter prototype by the well-known frequency and element transformations that can be found in any microwave textbook [59] or in books devoted to microwave filters [33, 58].[19] By properly designing the shunt resonators, the synthesis of standard frequency approximations is potentially possible. Actually, the transformation from the lowpass filter prototype leads to the structure of Figure 4.28b, with parallel *LC* resonant tanks. Thus, as long as resonator's admittances fit to those of the *LC* tanks (which depend on the *L* and *C* values inferred from circuit transformation), the targeted approximation (Butterworth, Chebyshev, etc.) can be achieved in the vicinity of resonance.

The elemental cell and circuit model of the proposed filters is depicted in Figure 3.60. Following Ref. [57], in the present study the series inductance of the line, *L*, is neglected since it is assumed that the region of interest lies in that frequency band where the series reactance is capacitive. The design methodology of the filters is a two-step process: first, the electrical parameters of the equivalent circuit model for each filter section (provided the filter is not periodic) are determined from specifications (central frequency, fractional bandwidth and filter order); then, the layout of the

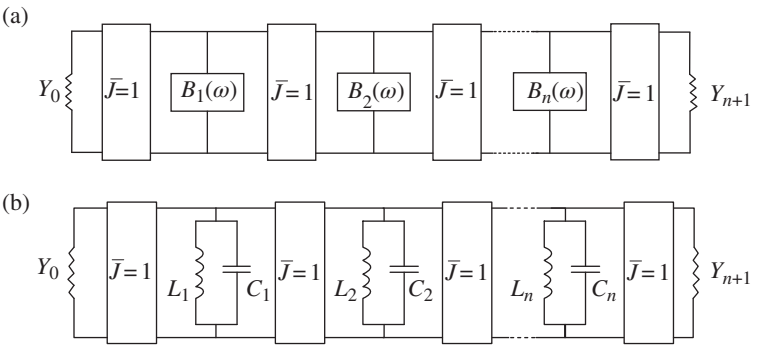

FIGURE 4.28 Generalized bandpass filter network with admittance inverters and shunt resonators (a). In (b), the resonators are *LC* resonant tanks.

[18] For that purpose, periodicity must be generally sacrificed.

[19] Alternatively, bandpass filters can be synthesized by alternating impedance inverters and series-connected resonators.

structure is synthesized. Let us consider the first aspect. In the circuit of Figure 4.28b, the filter central frequency, f_o, is determined by the resonance frequency of the shunt *LC* tanks, which nulls their admittance. However, this is not exactly the case for the filter implemented by cascading the elemental cells depicted in Figure 3.60, since resonators and admittance inverters are intermixed. Specifically, neither f_o coincides with the intrinsic resonance of CSRRs, nor it nulls the admittance of the shunt branch, $Y_p(\omega) = Z_p^{-1}(\omega)$. Nevertheless, at f_o the phase shift and transmission coefficient between the input and output ports of the basic cell should be $\phi = -90°$ (corresponding to backward wave propagation) and $|S_{21}| = 1$, respectively. This means that at f_o the characteristic impedance, Z_B, should coincide with the reference impedance of the ports, which is usually set to $Z_o = 50\ \Omega$. Thus, the series and shunt reactances of the T-circuit model of Figure 3.60 must satisfy: $Z_s(\omega_o) = -jZ_o$ and $Z_p(\omega_o) = jZ_o$. Actually, the dual solution ($Z_s(\omega_o) = jZ_o$ and $Z_p(\omega_o) = -jZ_o$) satisfies also the previous conditions on phase shift and impedance matching, but this solution is not compatible with the circuit of Figure 3.60 if *L* is neglected (i.e., with LH wave propagation). The above condition for Z_s and Z_p does not univocally determine the element values of the shunt impedance. These values are also determined by the 3 dB bandwidth of the resonators,

$$\Delta = \frac{\omega_2 - \omega_1}{\omega_o} \tag{4.38}$$

(where ω_o, ω_1, and ω_2 are the central—angular—frequency and 3 dB frequencies, respectively), and by the transmission zero, which occurs at that frequency where the shunt impedance reduces to zero (expression 3.86)

For a *LC* parallel resonant tank, with inductance and capacitance L_{eq} and C_{eq}, respectively, we have

$$\Delta = \frac{2}{Z_o}\sqrt{\frac{L_{eq}}{C_{eq}}} \tag{4.39}$$

If we consider the filter structure of Figure 4.28b, where the *L* and *C* values come from the lowpass filter prototype by frequency and element transformation according to [33]

$$C_{eq} = \left[\frac{1}{\mathrm{FWB}\cdot\omega_o\cdot Z_o}\right] g_i \tag{4.40}$$

$$L_{eq} = \frac{1}{\omega_o^2 C_{eq}} \tag{4.41}$$

and (4.40) and (4.41) are introduced in (4.39), the following expression for resonator bandwidths results:

$$\Delta_i = \frac{2\mathrm{FBW}}{g_i} \tag{4.42}$$

where g_i's are the element values of the lowpass filter prototype (which depend on the specific filter approximation and can be inferred from published tables) and Δ_i is the 3 dB bandwidth of the resonators. According to expression (4.42), Δ_i is proportional to the fractional bandwidth, FBW, and hence it is determined from the required filter bandwidth. Obviously, Δ_i is also dependent on g_i and it is therefore determined by the type of response and order. Once Δ_i are known, we can force the frequencies ω_1 and ω_2 to be equidistant from the central filter frequency. At these frequencies, under the assumption that $Z_s(\omega)$ does not substantially vary along the pass band, the shunt impedance of the unit cell satisfies: $Z_p(\omega_1) = jZ_o/2$ and $Z_p(\omega_2) = \infty$. These conditions plus $Z_p(\omega_o) = jZ_o$ give

$$\frac{L_d L_c \omega_1^3 (C + C_c) - L_d \omega_1}{L_c \omega_1^2 (C + C_c) - C\omega_1^2 L_d \left(L_c C_c \omega_1^2 - 1\right) - 1} = \frac{Z_o}{2} \tag{4.43}$$

$$L_c \omega_2^2 (C + C_c) - C\omega_2^2 L_d \left(L_c C_c \omega_2^2 - 1\right) - 1 = 0 \tag{4.44}$$

$$\frac{L_d L_c \omega_o^3 (C + C_c) - L_d \omega_o}{L_c \omega_o^2 (C + C_c) - C\omega_o^2 L_d \left(L_c C_c \omega_o^2 - 1\right) - 1} = Z_o \tag{4.45}$$

The previous approximation (which is valid for narrow and moderate bandwidths) leads us to simple analytical expressions (Eqs. 4.43 and 4.44). If this approximation is not applied, then the conditions arising from the 3 dB frequencies are not mathematically simple. Solution of Eqs. (3.86) and (4.43)–(4.45) leads us to the parameters of the shunt reactance, while the series capacitance is given by

$$C_g = \frac{1}{2Z_o \omega_o} \tag{4.46}$$

The criterion to set the transmission zero frequency, f_z, obeys to a compromise between the need to obtain a sharp transition in the upper band edge, and the convenience to far the spurious responses as much as possible, and thus optimize the out-of-band performance of the filter. Namely, a narrow spurious band above the pass band of interest arises. By adjusting f_z, this spurious can be minimized, and the filter frequency response can be significantly improved. Since the position of the spurious is not known a priori, the transmission zero frequency is tentatively set to $f_z = 2f_o$.[20] From the previous equations, the parameters of Figure 3.60b are inferred (except L,

[20] There is not a physical reason that justifies this choice. However, in practice, the spurious band lies in the vicinity of the first harmonic of the filter central frequency. This has been corroborated from several examples.

which is neglected, as mentioned before), and the topology of each filter cell (Fig. 3.60a) can be obtained.

For the synthesis of the layout, the method reported in Appendix H cannot be applied (this is of application in CSRR/gap-loaded lines but not in hybrid unit cells). Nevertheless, the model described in Ref. [60] can be used to obtain an initial guess for CSRR dimensions (the validity of the model is subjected to conditions that do not exactly apply in the considered filter cells [60]). The coupling capacitance, C, can be adjusted by partially removing the metal delimited by the CSRR contour. The length and width of the grounded metal strips (stubs) can be determined from independent full-wave EM simulations carried out in microstrip transmission lines loaded with these elements, or by using standard formulas [59]. A similar procedure can be used to determine the geometry of the series capacitances. From this initial layout, the frequency response of the complete filter is then simulated by means of a full wave EM solver, thus being visible the position of the spurious band. To eliminate this band, f_z is adjusted, and the model parameters are then recalculated. To determine the final layout, cell dimensions should be adjusted (starting from the seeding topology) in order to fit the electrical response obtained from the latter model parameters as much as possible. In practice, this is simple since cell bandwidth is mainly controlled by L_d and C (provided f_z and f_o are distant enough). Therefore, stub dimensions and the etched area inside the CSRRs can be adjusted to match to the required bandwidth, while the transmission zero frequency can be tailored by scaling CSRR dimensions. The parameter extraction method for CSRR-based lines, conveniently modified, can also be of help for the synthesis of the circuit layout.

Illustrative Examples Let us now consider the design of a bandpass filter with moderate bandwidth following this approach. In this example, a periodic structure is considered, although periodicity is not a necessary condition. The specifications are order 3, central frequency $f_o = 1$ GHz and fractional bandwidth FBW = 10%. This filter does not obey any standard approximation; therefore, we cannot directly determine g_i from table values, as usual. Obviously, due to periodicity, all resonators must have the same Δ and, accordingly, the same g. To obtain the value of g, an order-3 lowpass filter prototype with identical element values has been considered, and it has been forced to exhibit the 3 dB cutoff at the normalized $\omega = 1$ rad/s angular frequency. From this, it is obtained $g = 1.521$; hence, the 3 dB bandwidth of the resonators, Δ, is perfectly determined. From the previously explained procedure, the element values of the equivalent circuit model were obtained. They are identical for the three filter cells and are depicted in Table 4.2. Layout dimensions for the basic cell are indicated in

TABLE 4.2 Element values of the equivalent circuit model for the filter of Figure 4.30

C_g(pF)	L_d(nH)	C(pF)	C_c(pF)	L_c(nH)
1.59	1.33	12.33	21.7	0.23

Figure 4.29 (the parameters of the *Rogers RO3010* substrate with thickness $h = 1.27$ mm and dielectric constant $\varepsilon_r = 10.2$ have been used).

The EM simulation of the frequency response (amplitude and phase) of the single-cell structure is represented in Figure 4.29 and compared to that obtained from the circuit simulation (insertion loss only) of the equivalent circuit model (with the parameters indicated in Table 4.2). Reasonable agreement between the circuit and EM simulations is obtained. The simulated and measured insertion and return loss for the fabricated three-stage filter are depicted in Figure 4.30. Thanks to the transmission zero, the frequency response is spurious free up to approximately $3f_o$. In-band insertion and return losses are good (i.e., $IL < 1.5$ dB and $RL > 17$ dB) and frequency selectivity at both band edges is high, with near symmetric transition bands. The measured fractional bandwidth is FBW = 8%, which coincides to a good approximation with the nominal value. Cell dimensions (length) are small as compared to signal wavelength at f_o (i.e., $l_c \sim \lambda/7$). Further miniaturization can be achieved with the penalty of critical (smaller) dimensions being closer to the limits imposed by the fabrication technology (typically ≈ 100 μm). To avoid problems related to fabrication tolerances, critical dimensions substantially larger than 100 μm were considered in this design, with the result of a moderately small cell size. In Figure 4.30b, the simulated frequency response (insertion loss) obtained on a conventional microstrip coupled line bandpass filter with similar performance is also included (layout comparison is shown in the inset of Fig 4.30b). As compared to the conventional response, where a spurious band is present at $2f_o$, the CSRR-based prototype device filter exhibits near 40 dB rejection at that frequency, and device length, excluding access lines, is 2.4 times shorter. This prototype device, published in Ref. [57], was the first LH transmission line based on CSRRs (hybrid approach) employed for the design of a bandpass filter following a methodology able to provide the element values of the equivalent circuit model. Another interesting example of the approach is the design of an order-3 Chebyshev (i.e., nonperiodic) bandpass filter with 9% fractional bandwidth, 0.3 dB ripple, centered at $f_o = 2.5$ GHz (see Ref. [57] for details). Following this design methodology, an ultracompact bandpass filter at K-band, implemented in MCM-D technology, was reported in Ref. [61].

Alternatively to the unit cell of Figure 3.60 (hybrid cell), the shunt resonators (composed of the CSRRs plus the shunt inductive strip) may be coupled through quarter wavelength transmission lines or by means of inductive elements. The design approach, summarized in Ref. [4], is similar to that reported before and has been applied to the design of bandpass filters with moderate bandwidths [62–64]. It is also possible to achieve wide band filter responses by considering balanced hybrid cells, as discussed in Ref. [65, 66]. Figure 4.31 depicts a bandpass filter based on a periodic structure consisting of four balanced hybrid cells, and subjected to the following specifications: bandwidth covering the 4–6 GHz range or wider, at least 80 dB rejection at 2 GHz, in-band insertion losses lower than 1 dB, and group-delay variation smaller than 1 ns. The simulated frequency response and group delay satisfy these requirements, although due to the critical dimensions of some geometry parameters (and fabrication related tolerances), the measured response exhibits higher in-band losses. It is

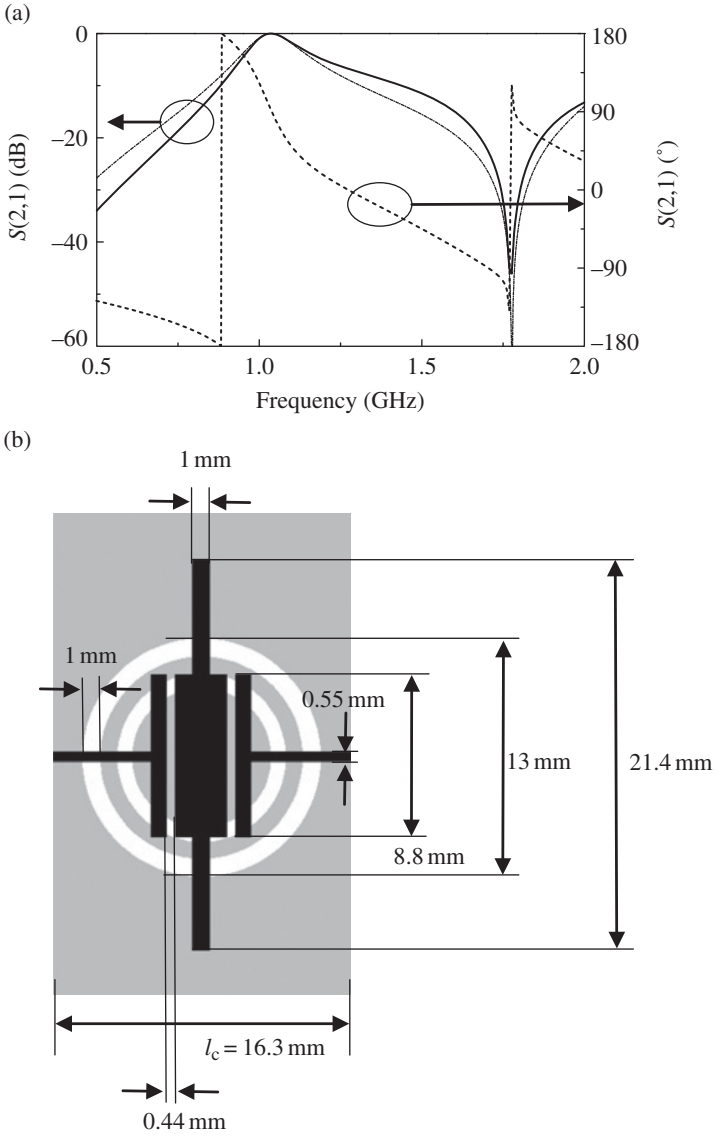

FIGURE 4.29 Simulated frequency response (amplitude and phase) corresponding to the basic filter cell of the designed filter, depicted in (b). The insertion loss obtained by circuit simulation of the equivalent circuit model is also depicted (thin line). The positive phase (+90°) of S_{21} (negative electrical length), obtained at f_o, clearly points out the LH nature of the structure. Reprinted with permission from Ref. [57]; copyright 2006 IEEE.

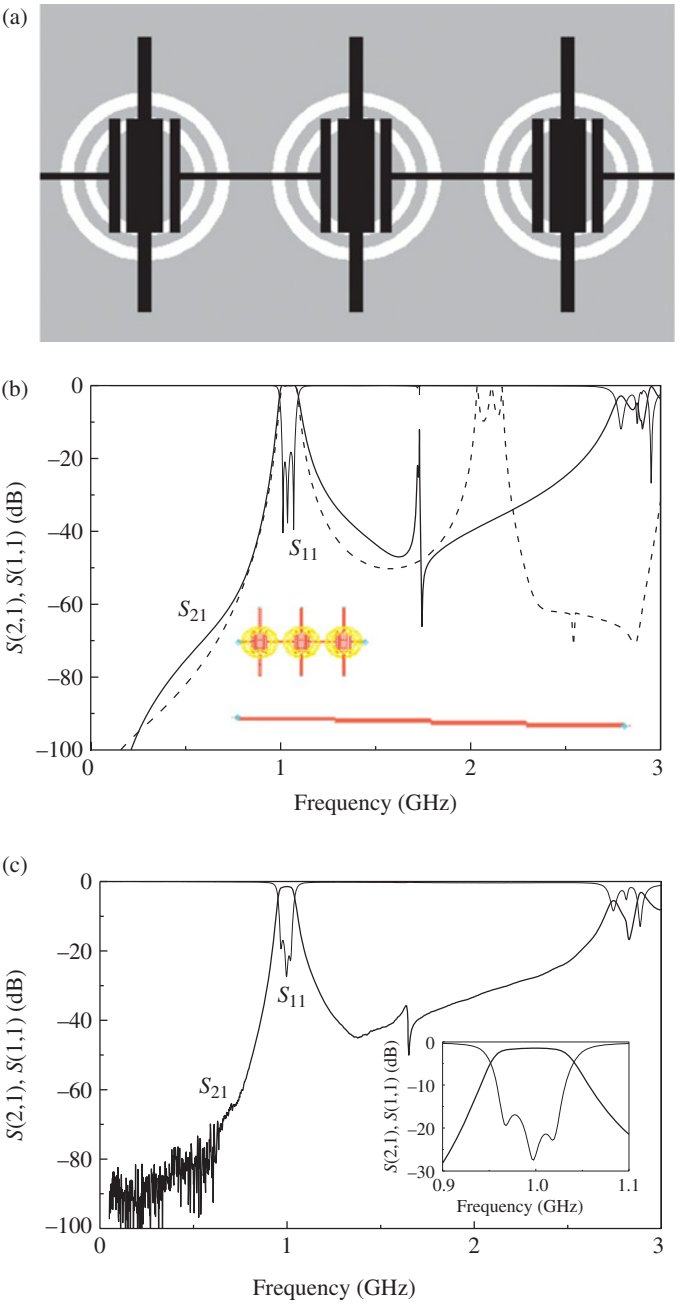

FIGURE 4.30 Layout of the fabricated periodic filter (a), simulated (b), and measured (c) insertion and return loss. Total device length excluding access lines is 4.56 cm. In (b), the simulated insertion loss for a conventional order-3 coupled line filter with similar performance is depicted (dashed line). Reprinted with permission from Ref. [57]; copyright 2006 IEEE.

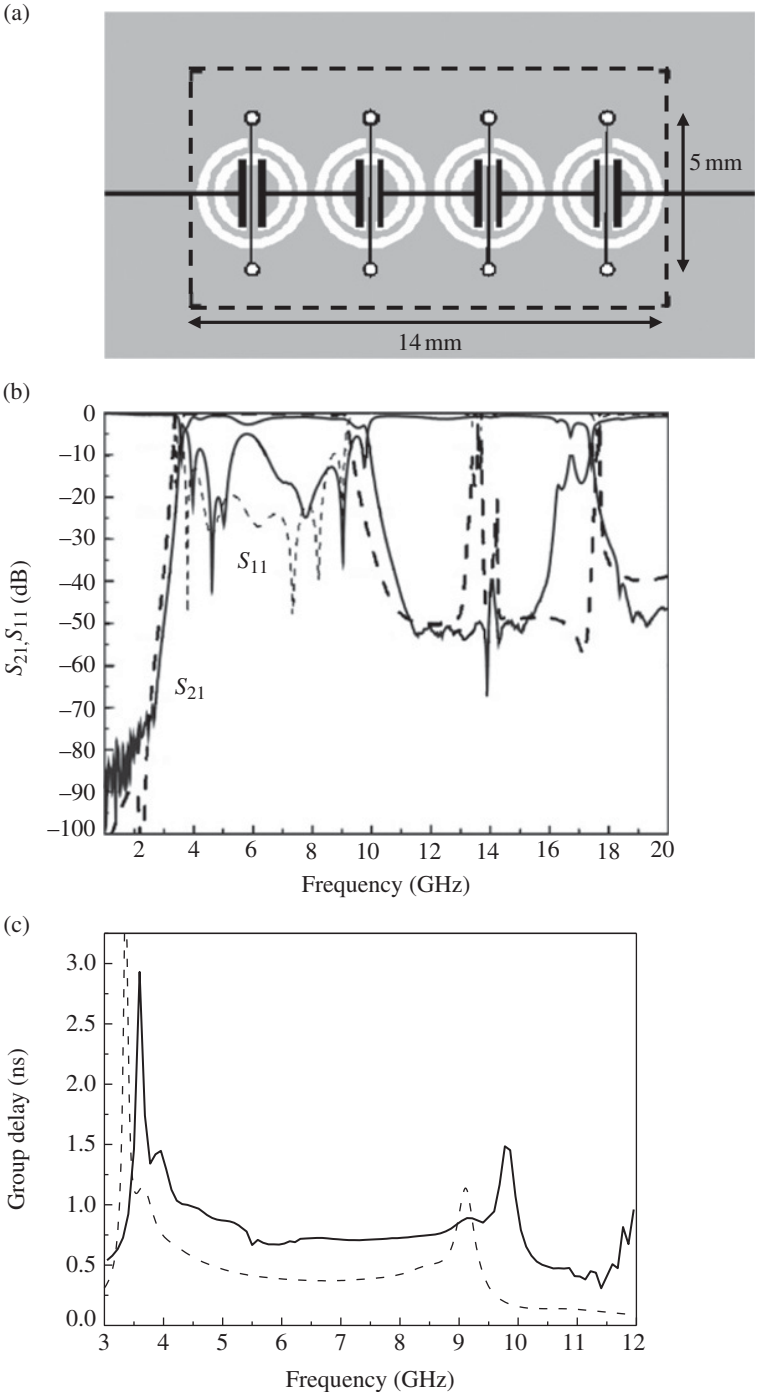

FIGURE 4.31 Layout of the wide band filter based on balanced hybrid cells (a), simulated (dashed line) and measured (solid line) frequency response (b), and simulated (dashed line) and

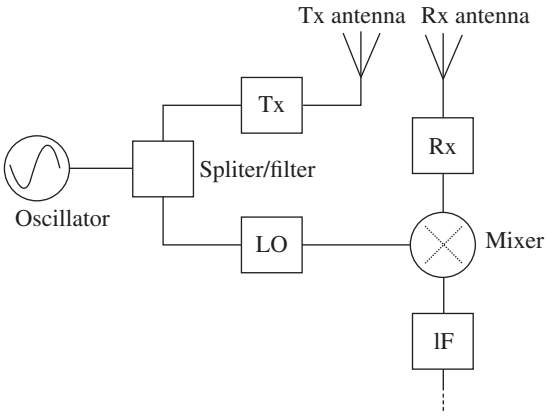

FIGURE 4.32 Schematic of the front-end of a FMCW-GPR system that uses one transmitter (Tx) antenna and one receiver (Rx) antenna.

remarkable that the filter area is as small as 0.7 cm^2. This size points out the potential of CSRR filters based on the hybrid cell for device miniaturization.

The last example of this subsection is a multifunctional filter, namely, a wideband filter with power splitting capability, of interest, for instance, for the front-end miniaturization of frequency-modulated continuous-wave ground penetrating radars (FMCW-GPRs) [67, 68]. The schematic of such system is depicted in Figure 4.32. The input signal to the power divider is modulated so that its frequency varies gradually. The power divider splits the signal between the transmitter antenna and the local oscillator of the receiver mixer, so that the radar signal is mixed with the signal reflected from the target object. Its depth can be determined from the intermediate (IF) signal frequency according to standard formulas [59]. To improve resolution and to obtain high penetration depths, it is convenient to deal with moderately low carrier frequencies (operation at the L-band) and wide radar frequency sweep. Thus, power splitters with significant fractional bandwidth are necessary. Such power dividers must also be able to reject the first harmonic of the radar signal within the whole frequency sweep. For this reason, filters are also needed (notice that harmonic rejection at a single frequency, reported in several papers [69, 70], does not suffice in the present application). In order to save space, a new power divider concept, with filtering capability, was proposed in Ref. [67] (this concept is also included in the review

FIGURE 4.31 (*Continued*) measured (solid line) group delay (c). The metallic parts are depicted in black in the top layer, and in gray in the bottom layer. The dashed rectangle has an area of 1 cm^2. Dimensions are line width $W = 0.126$ mm, external radius of the outer rings $r = 1.68$ mm, rings width $c = 0.32$ mm, and rings separation $d = 0.19$ mm; inductor width is 0.10 mm and the distance between the metals forming the gap is 0.4 mm. The considered substrate is the *Rogers RO3010* with dielectric constant $\varepsilon_r = 10.2$ and thickness $h = 0.127$ mm. Reprinted with permission from Ref. [65], copyright 2007 IEEE.

paper [68]), and reported here as an illustrative example of application of the hybrid approach of metamaterial transmission lines. The following system requirements were considered: frequency sweep 1—2 GHz; at least 20 dB rejection for the first harmonic; return losses for the splitter/filter better than 10 dB; insertion losses for the splitter/filter below 5 dB. Since the first harmonics (lower frequencies) are very close to the upper frequency of the modulated radar signal, the whole bandwidth was covered by means of two splitter/filters: one designed to scan the 1–1.5 GHz band; the other covering the 1.4—2 GHz frequency band. The area of both devices was required to be smaller than 12 cm^2.

The considered strategy for the implementation of the filters/splitters was to add an inductive transformer to the output stage of a bandpass filter. By this means, the load of the device (corresponding to the parallel connection of the two terminated output ports, that is, $R = 25\ \Omega$) can be driven to the required value to achieve input matching ($R_{eq} = 50\ \Omega$), and the filtering and splitting action are combined in a single multifunctional device. According to this strategy, the device is indeed a bandpass filter with modified output stage. The inductive transformer equations are (Fig. 4.33):

$$R_{eq} = \left(1 + \frac{L_1}{L_2}\right)^2 \cdot R \tag{4.47}$$

$$L_{eq} = L_1 + L_2 \tag{4.48}$$

Thus, it is possible to adjust the values of L_1 and L_2 to obtain the required value of the impedance R_{eq}, that is $R_{eq} = 50\ \Omega$. We report here the implementation of the splitter/filter covering the band 1–1.5 GHz. To this end, a fourth-order filter was considered, where three filter stages were implemented by means of a balanced hybrid cell (similar to that of Fig. 4.31), and the additional stage was implemented by parallel connecting an inductive stub (acting as inductive transformer) and a series resonator (implemented by series connecting a narrow inductive strip, L_3, and a capacitive patch, C_1), as depicted in Figure 4.34. This later stage, with the presence of the inductive stub, is required to include the inductive transformer, which cannot be integrated within the hybrid cell. Essentially, this fourth stage is a shunt connected parallel resonator. However, the additional inductance L_3 series connected to the capacitor C_1 provides an additional transmission zero, of interest to improve the filter stop band response.

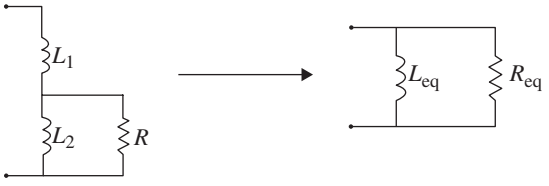

FIGURE 4.33 Inductive transformer.

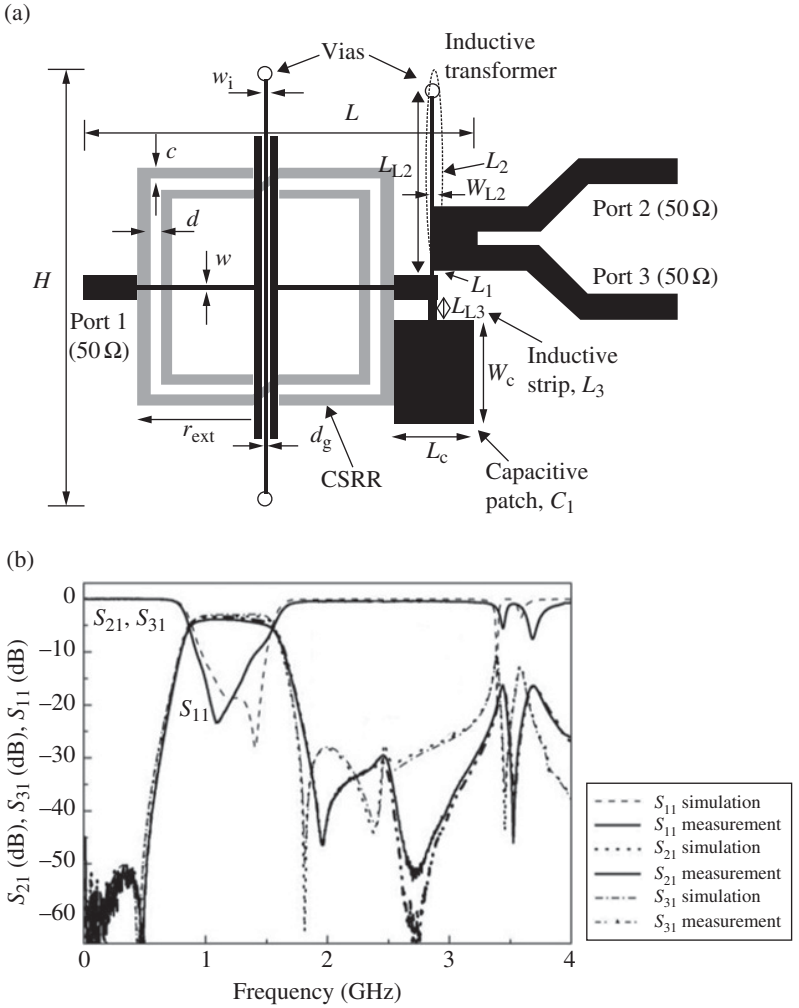

FIGURE 4.34 Topology of the designed filter/splitter (a), and EM simulation and measurement of the power splitting (S_{21}, S_{31}) and matching (S_{11}) (b). Dimensions are $H = 32.6$ mm, $L = 27.3$ mm, $W_l = 0.2$ mm, $c = 0.79$ mm, $d = 0.79$ mm, $w = 0.16$ mm, $r_{ext} = 8.12$ mm, $d_g = 0.26$ mm, $L_c = 5.7$ mm, $W_c = 7.7$ mm, $L_{L2} = 12.96$ mm, $W_{L2} = 0.2$ mm, and $L_{L3} = 1.53$ mm. The device was implemented on the *Rogers RO4003* substrate with thickness $h = 0.81$ mm and dielectric constant $\varepsilon_r = 3.55$. Notice that for better comprehension, in this figure the CSRR, etched in the back substrate side (ground plane), is depicted in gray (the back side metallization is not depicted). Black color corresponds to the upper metal level. Reprinted with permission from Ref. [68]; copyright 2011 IEEE.

The topology of the proposed filter/splitter is depicted in Figure 4.34. For design purposes, the equivalent circuit model of the hybrid cell, as well as the elements describing the inductive transformer and the shunt connected series resonator, were considered. However, the structure is complex and optimization at layout level was necessary. The EM simulation and measurement of the frequency response of the filter/splitter are depicted in Figure 4.34b. The specifications given earlier were fulfilled, with measured insertion losses in the center frequency of the pass band ($S_{21} = 3.8$ dB and $S_{31} = 3.1$ dB) close to the ideal value (3 dB) of a splitter, and a device area of 8.9 cm^2.

4.2.3.5 Highpass Filters Based on Balanced CRLH Lines In microwave engineering, the difference between a highpass and a bandpass filter is subtle since highpass filters implemented in planar technology do not exhibit an unlimited bandwidth above the cutoff frequency. Thus, microwave highpass filters are actually bandpass filters with a very wide band and a controllable cutoff frequency at the lower band edge. These filters can be implemented by cascading balanced CSRR/gap-loaded lines with unit cells similar to that depicted in Figure 3.42, by virtue of the wide band and transmission zero that such balanced cells exhibit. Rejection below cutoff can be controlled by the number of cells, as illustrated in Figure 4.35. This figure depicts the layout of a fabricated three-cell highpass filter [66]. The filter exhibits a measured rejection better than 50 dB below the cutoff frequency, and in-band insertion and return losses are good up to roughly 3 GHz.

The second reported prototype is a highpass filter implemented by means of a balanced SRR/strip-loaded CPW with three pairs of SRRs (Fig. 4.36) [71]. In this device, designed to exhibit the transmission zero frequency at $f_z = 1.4$ GHz, the measured rejection in the stop band is better than 30 dB, and insertion loss in the transmission band is good ($IL < 2$ dB between 1.40 and 2.48 GHz). Notice that the topology of the host CPW was modified (as compared to the typical topologies of SRR/strip-loaded CPWs) in order to balance the structure.

Bandpass filters with ultra wideband (UWB) responses can be designed by introducing additional elements to the balanced CSRR/gap-loaded lines able to generate a controllable upper edge. Such structures have been applied to the design of UWB bandpass filters covering the mask supplied by the Federal Communications Commission (FCC) [41, 72].

4.2.3.6 Wideband Filters Based on OSRRs and OCSRRs The open particles, OSRRs and OCSRRs, are useful for the design of bandpass filters with wide fractional bandwidths and small dimensions. Two main strategies have been reported for the implementation of wideband filters based on these particles. One of them consists of using series connected OSRRs or shunt connected OCSRRs coupled through impedance inverters; the other strategy combines series OSRRs and shunt OCSRRs in configurations similar to those corresponding to CRLH lines based on these open resonant particles (reported in Section 3.5.2.5).

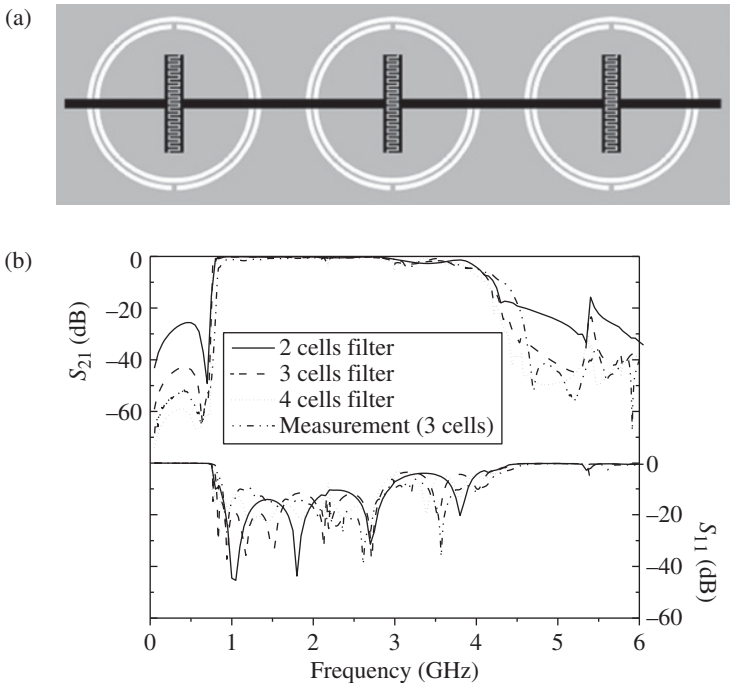

FIGURE 4.35 Layout of the microstrip highpass filter formed by three balanced CRLH CSRR-based cells (a) and measured frequency response (b). In (b), the simulated insertion and return losses for a two-, three-, and four-stage device filters are also depicted. The metallic parts are depicted in black in the top layer, and in gray in the bottom layer. Dimensions are total length $l = 55$ mm, line width $W = 0.8$ mm, external radius of the outer rings $r = 7.3$ mm, rings width $c = 0.4$ mm, and rings separation $d = 0.2$ mm; the interdigital capacitors are formed by 28 fingers separated 0.16 mm. The substrate is the *Rogers RO3010* with thickness $h = 1.27$ mm and dielectric constant $\varepsilon_r = 10.2$. Reprinted with permission from Ref. [66]; copyright 2007 IEEE.

Bandpass Filters Based on OSRRs or OCSRRs Coupled through Impedance Inverters The idea of using OSRRs for the implementation of wideband bandpass filters was first reported in Ref. [73], and the systematic approach for the design of filters where such resonators are coupled through impedance inverters was reported in Ref. [74]. The relatively large capacitance values of OSRRs are the responsible for the wideband response of these particles, and hence for the broad achievable fractional bandwidths. Filter design is based on the generalized bandpass filter network depicted in Figure 4.37, where series LC resonators are coupled through impedance inverters [33].[21] As it is pointed out in Ref. [33], there are two possibilities for filter design.

[21] This network is an alternative to the network depicted in Figure 4.28 for the design of bandpass filters. However, the approach for filter design considered in this subsection is the standard approach reported in Ref. [33], and hence different than the one reported in Section 4.2.3.4.

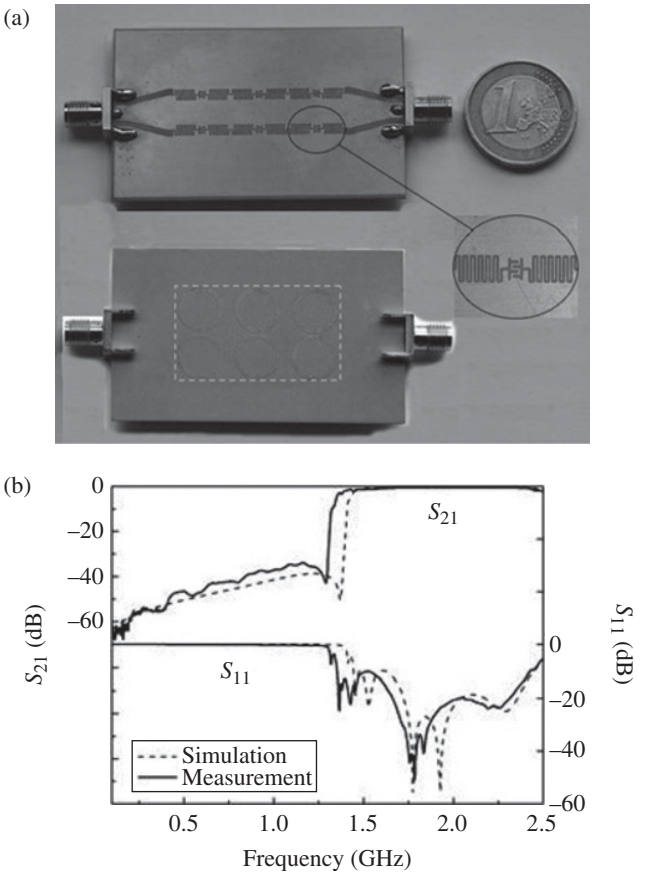

FIGURE 4.36 Photograph of the CPW highpass filter implemented by means of three CRLH SRR-based cells (a) and frequency response (b). Dimensions are external radius of the SRRs $r_{ext} = 4.68$ mm, width of the rings $c = 0.223$ mm, and rings separation $d = 0.237$ mm. The shunt inductance is implemented by means of a meander with width $w_m = 0.2$ mm and separation distance $s_m = 0.2$ mm. The gap distance between the central strip and the ground planes is $g = 0.16$ mm. The substrate is the *Rogers RO3010* with thickness $h = 1.27$ mm and measured dielectric constant $\varepsilon_r = 11.2$. Reprinted with permission from Ref. [71]; copyright 2010 IET.

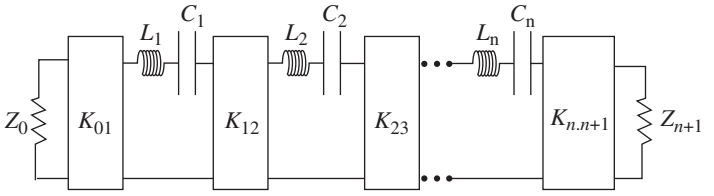

FIGURE 4.37 Generalized bandpass filter network with impedance inverters and series LC resonators.

In the first case, all the inverters are forced to have the same normalized impedance, $\overline{K}_{ij} = 1$ (i.e., the inverters are quarter wavelength transmission lines with the usual characteristic impedance $Z_o = 50\ \Omega$). In this case, the design algorithm provides different values of L_i and C_i for each filter stage. The second option, considered in Ref. [73, 74],[22] employs the same resonator for all filter stages (therefore, the values of L_i and C_i are identical in the different filter stages) and different values of K_{ij} for the impedance inverters.

As an example, an order-7 microstrip bandpass filter with central frequency $f_o = 5$ GHz, 40% fractional bandwidth and 0.01 dB ripple is reported [74] (the considered substrate is the *Rogers RO3010* with dielectric constant $\varepsilon_r = 10.2$ and thickness $h = 0.254$ mm). The geometry of the OSRR was chosen to provide a series inductance and capacitance of $L = 2.99$ nH and $C = 0.338$ pF (the effects of the parasitics are accounted for in the impedance inverters). With these reactive values, the impedances of the inverters that result by applying the formulas given in Ref. [33] (un-normalized values) are: $K_{01} = K_{78} = 48.6\ \Omega$, $K_{12} = K_{67} = 35.7\ \Omega$, $K_{23} = K_{56} = 24.1\ \Omega$, and $K_{34} = K_{45} = 22.2\ \Omega$. The determination of the length and width of the inverters was done through optimization, by forcing 90° phase shift for all filter stages at f_o. The filter layout and the frequency response are depicted in Figure 4.38. In-band insertion losses are very small (<1 dB), whereas the measured filter bandwidth is 36%, slightly below the nominal value as expected on account of the limited functionality of the impedance inverters.[23] Optimization of filter size by meandering the inverters is reported in Ref. [74] through two additional examples.

Wideband bandpass filters based on OCSRRs and implemented in CPW technology were reported for the first time in Ref. [75] (the design methodology is similar to that corresponding to the OSRR-based filters detailed above). Notice that the wideband filters considered in this subsection are not based or inspired on artificial transmission lines. They are simply implemented by means of the open versions of the SRR or CSRR (i.e., OSRRs and OCSRRs). Nevertheless, the inclusion of these filters in this book obeys to the fact that these filters were conceived before the OSRR/OCSRR-based CRLH lines (discussed in Section 3.5.2.5), and they were in fact the precursor of these artificial lines and the filters based on them, to be discussed in the next subsection.

Bandpass Filters Based on CRLH Lines Implemented by Means of OSRRs and OCSRRs The CRLH unit cell based on the combination of OSRRs and OCSRRs, used in Section "Dual-Band Devices Based on Fully Planar CRLH Lines" for the

[22] The reason for this choice is that the synthesis of transmission lines with a given characteristic impedance is more simple than the synthesis of OSRRs with given values of L and C.

[23] It is well known that wideband filters based on impedance inverters implemented by means of quarter-wavelength transmission lines experience bandwidth degradation as compared to the nominal value. The reason is that in the extremes of the transmission band, the phase of the line may be distant from the 90° requirement for inverter functionality.

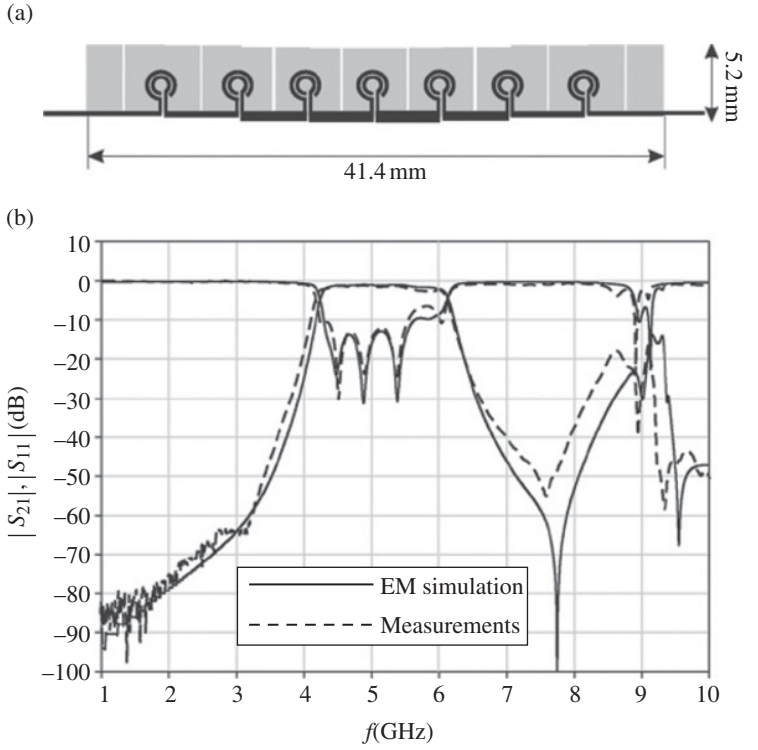

FIGURE 4.38 Layout (a) and frequency response (b) of the filter based on OSRR coupled through impedance inverters. OSRR dimensions are $r_{ext} = 1.1$ mm and $c = d = 0.2$ mm. The gray region indicates the windows in the ground plane. Reprinted with permission from Ref. [74]; copyright 2007 IEEE.

implementation of dual-band components, is described by a model that is also the canonical circuit of an order-3 bandpass filter.[24] Therefore, such structures can be used as building blocks for wideband bandpass filter design. By sacrificing periodicity, it is possible to implement higher-order filters subjected to standard responses, such as Chebyshev or Butterworth, among others. Filter synthesis follows the same approach considered for the synthesis of dual-band impedance inverters and the dual-band components based on them. Therefore, it will not be repeated in this subsection. Let us recall, however, that synthesis requires tuning the element values of the circuit model with the presence of parasitics in order to achieve the required response. If the parasitics are small, and for low-order filters, this tuning can be done manually. However, if the filter order and/or the parasitic element values increase, the manual

[24] Notice that by neglecting the parasitics, the circuits of Figure 3.58c, or d, are the circuit models of order-3 bandpass filters and also the circuit models of order-2 CRLH lines, where the line order indicates the number of elements of the series and shunt branch of the CRLH line, as discussed in Chapter 3. Therefore, caution must be taken to avoid confusion between filter order and line order (for CRLH lines).

tuning of the structure can be complex and time-consuming. For this reason, an automatic optimization routine that forces the frequency positions at the N matching points (N being the filter order) of the Chebyshev response (which is the considered response in all the examples) can be implemented in a commercial circuit simulator, such as the *Agilent ADS* [76]. Thus, from the matching frequencies and ripple, given by the standard Chebyshev response, the optimum circuit elements (considering the parasitics set to certain values) can be obtained. This procedure allows us to obtain filter responses at the circuit level, with the presence of parasitics, which are very close to the required Chebyshev response. The resulting circuits are slightly unbalanced in order to preserve the equal-ripple magnitude response. One important point for filter design, especially for wide band filters, is the inclusion of the inductance L_{sh} in the circuit model of the OCSRR stages (see Fig. 3.55). This typically gives higher rejection at the upper stop band, as compared to the Chebyshev response, and the agreement with the EM simulation and measurement is expected to be more accurate.

The synthesis technique was applied to the design of various filters with different order and bandwidth [28, 68, 76–78], including order-7 filters and fractional bandwidths in the vicinity of 100%. As an example, Figure 4.39 depicts an order-3 Chebyshev bandpass filter with central frequency $f_o = 2$ GHz, 0.15 dB ripple and 70% fractional bandwidth, and its frequency response as well. In the narrow band response,[25] where the lossless EM simulation and the circuit simulation with and without the inclusion of L_{sh} are considered, it can be appreciated the excellent agreement between the circuit and EM simulation when L_{sh} is included. The wideband response indicates that the measured filter response is in good agreement with the circuit simulation and with the ideal Chebyshev response. It is also remarkable that filter size is as small as $0.13\lambda \times 0.15\lambda$, where λ is the guided wavelength at the filter central frequency. In summary, the combination of OSRRs and OCSRRs is useful for the design of filters requiring wide transmission bands and small size. The synthesis procedure is simple, and the circuit models accurately describe the filter responses.

Dual-Band Bandpass Filters Based on the E-CRLH Transmission Line Concept It is also possible to design dual-band bandpass filters by means of the order-4 E-CRLH structures of the type depicted in Figure 4.19. This dual-band functionality can be obtained from the lowpass filter prototype through convenient transformations. In a first step, a single-band bandpass response results from the well known transformation [58]:

$$\frac{\Omega}{\Omega_c} = \frac{1}{w}\left(\frac{\omega}{\omega_0} - \frac{\omega_0}{\omega}\right) \tag{4.49}$$

Ω and ω being the angular frequency of the lowpass and bandpass filter, w and ω_0 the fractional bandwidth and central frequency of the bandpass filter and Ω_c the angular cutoff frequency of the lowpass filter. Then, a second transformation is applied to the single-band bandpass filter to obtain dual-band behavior [79]:

[25] By narrow band response, we mean the insertion and return loss restricted to the bandpass region (that can be arbitrarily broad).

$$\omega = \frac{\omega_0}{w'}\left(\frac{\omega'}{\omega_0} - \frac{\omega_0}{\omega'}\right) \tag{4.50a}$$

$$w' = \left(\frac{\omega_2 - \omega_1}{\omega_0}\right) \tag{4.50b}$$

$$\omega_0 = \sqrt{\omega_1 \omega_2} \tag{4.50c}$$

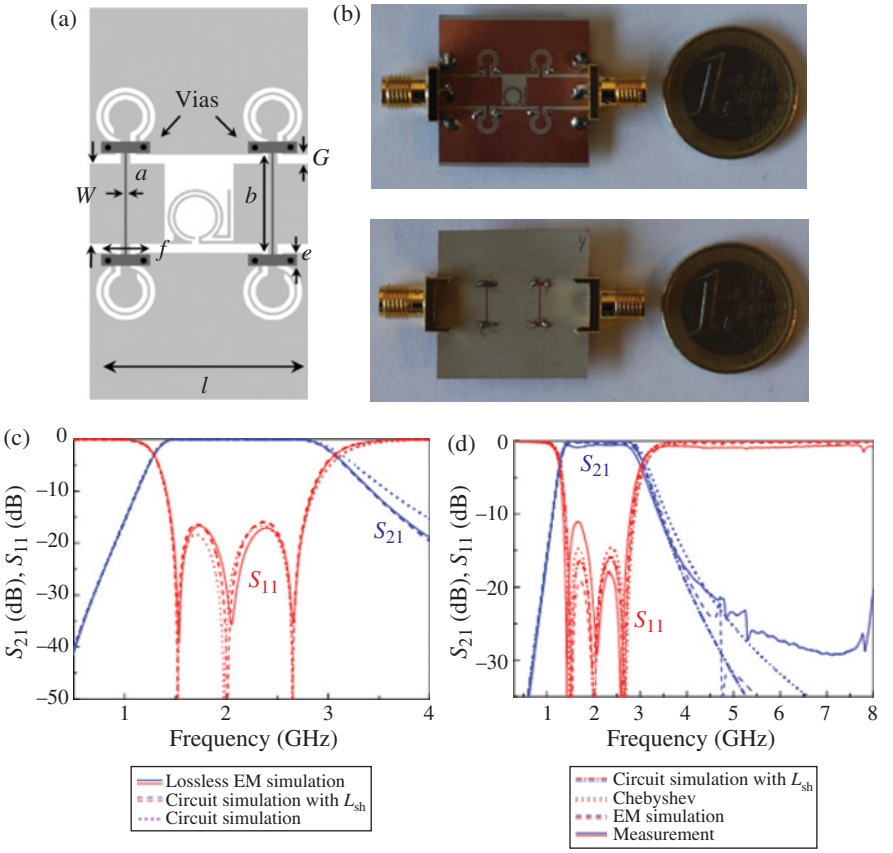

FIGURE 4.39 Topology (a), photograph (b), narrow band response (c), and wideband response (d) of the designed third-order filter with 70% fractional bandwidth. The considered substrate is the *Rogers RO3010* with thickness $h = 0.254$ mm and measured dielectric constant $\varepsilon_r = 11.2$. Dimensions are $l = 13.38$ mm, $W = 5$ mm, $G = 0.547$ mm, $a = 0.16$ mm, $b = 6.27$ mm, $e = 0.73$ mm, and $f = 3$ mm. For the OCSRR, $r_{ext} = 1.8$ mm, $c = 0.3$ mm, and $d = 0.16$ mm. For the OSRR, $r_{ext} = 1.7$ mm, and $c = d = 0.16$ mm. The values of the circuit simulation considering parasitics are (in reference to Figure 3.58d): $C = 0.188$pF, $L = 0.62$nH, $C_s = 0.85$pF, $L'_s = 6.3$nH, $C'_p = 2.43$pF, and $L'_p = 2.7$nH. The modified values of the OCSRR considering the wideband model with the additional parasitic element L_{sh} are (in reference to Figure 3.55a): $L = 0.62$ nH, $C'_p = 2.54$ pF, $L'_p = 2.56$ nH, and $L_{sh} = 0.15$ nH. Reprinted with permission from Ref. [68]; copyright 2011 IEEE.

ω' being the angular frequency of the dual-band bandpass filter and ω_1, ω_2 the angular central frequencies of the first and second filter bands. Once these transformations are applied to the lowpass filter prototype, the circuit of Figure 3.25c is obtained, provided identical fractional bandwidths for the two bands, as well as the narrow band approximation (i.e., a fractional bandwidth, *FBW*, for each band less than 10%), are considered [79]. As reported in Ref. [79], the element values of the circuit of Figure 3.25c are obtained from a set of equations dependent on the lowpass filter prototype coefficients (g_i), Ω_c and on the relevant design parameters, namely, the angular central frequencies (ω_1, ω_2) and the *FBW* (these equations are not reproduced here for simplicity).

Using this procedure, a dual-band bandpass filter that covers the GSM (0.9–1.8 GHz) and the *L*1 (1575.42 MHz) – *L*5 (1176.45 MHz) civil GPS frequency bands is reported [35]. An order-3 Chebyshev response with 0.01 dB ripple, central frequencies of $f_{c1} = 1.02$ GHz and $f_{c2} = 1.68$ GHz, and 20% fractional bandwidth was considered. Even though the narrow band approximation is not satisfied, the filter response is in good agreement with the ideal (single-band) Chebyshev response (only small deviations in the transition bands are observed). From the aforementioned filter specifications, the values of the circuit elements (Fig. 3.25c) are $L_{hs} = 19.05$ nH, $C_{hs} = 0.79$ pF, $L_{hp} = 1.16$ nH, $C_{hp} = 12.69$ pF, $L_{vs} = 10.29$ nH, $C_{vs} = 1.43$ pF, $L_{vp} = 2.58$ nH, and $C_{vp} = 5.71$ pF.

Using the design methodology applied to the quad-band inverters, the filter layout was obtained (this is depicted in Figure 4.40 together with the photograph of the fabricated prototype). Filter optimization taking parasitics into account was done by tuning the reactive elements at the circuit level. Specifically, the values that are changed (in reference of Fig. 4.19b) are $L_{hs} = 18.26$ nH, $C_{vp} = 4.4$ pF, $C_1 = 0.33$ pF, $C_2 = 0.51$ pF, and $L = 0.45$ nH.

The frequency response and group delay of the filter, including measurement, EM simulation, circuit simulation of the accurate circuit model of Figure 4.19b and the dual-band Chebyshev response (circuit of Fig. 3.25c), are also depicted in Figure 4.40. As can be seen, good agreement between the different responses is obtained, with measured return losses better than 20 dB and a rejection level better than 20 dB up to 4.6 GHz ($3.5f_o$), f_o given by expression 4.50c. Moreover, the size of the filter is 19.5 mm × 13.5 mm, which corresponds to $0.22\lambda_g \times 0.15\lambda_g$, λ_g being the guided wavelength at f_o.

4.2.3.7 Elliptic Lowpass Filters Based on OCSRRs The elliptic lowpass filters considered in this subsection are actually structures based on transmission lines with metamaterial loading (OCSRRs). Namely, they are neither based on the CRLH transmission line concept nor on the hybrid approach or on other structures that can be used as building blocks of metamaterial transmission lines. Nevertheless, the proposed OCSRR-based elliptic lowpass filters are introduced here for thematic coherence and because the procedure for filter design is not very different to that considered for the design of bandpass filters based on the combination of OSRRs and OCSRRs.

The reported OCSRR-based elliptic-function lowpass filters are described by the network of Figure 4.41 and implemented in coplanar waveguide (CPW) technology.

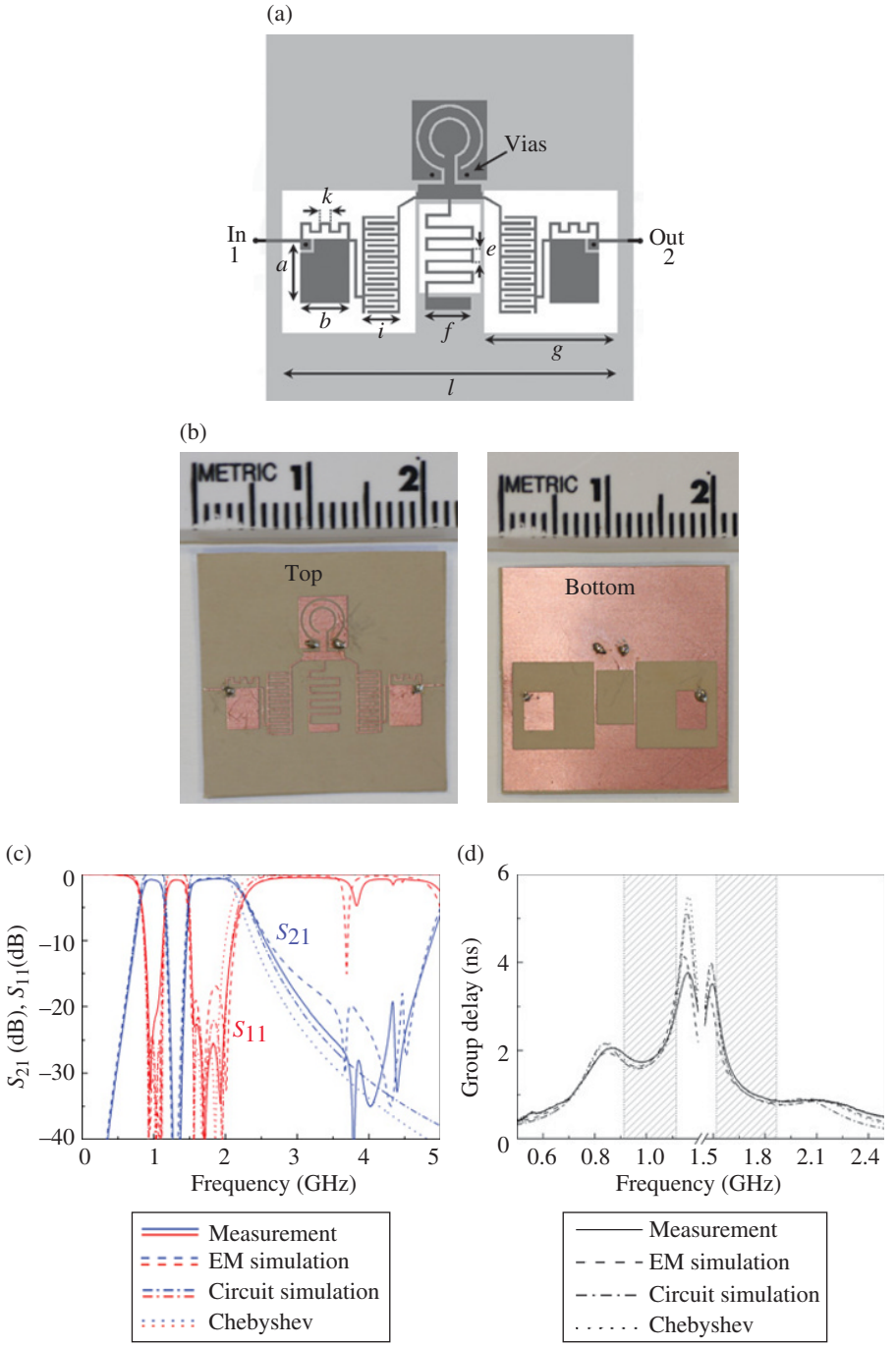

FIGURE 4.40 Layout (a), photograph (b), frequency response (c), and group delay (d) of the dual-band bandpass filter. Dimensions are $a = 3.52$ mm, $b = 2.85$ mm, $f = 2.64$ mm,

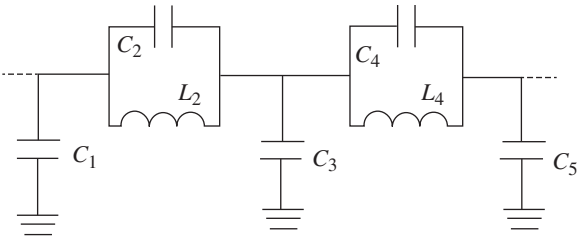

FIGURE 4.41 Low-pass elliptic-function prototype filter. The circuit corresponds to a fifth-order prototype.

The series connected parallel resonators are implemented by means of OCSRRs, whereas the shunt capacitances are implemented by etching metallic patches in the back side of the substrate connected to the ground planes through vias. The device (presented in Ref. [80]) is an order-5 elliptic-function lowpass filter with a pass band ripple of $L_{Ar} = 0.1$ dB, a cutoff frequency of $f_c = 1$ GHz and an equal-ripple stop band starting frequency of 1.4085 GHz (with stop band ripple of $L_{As} = 39.59$ dB) [33]. The element values corresponding to this elliptic filter response are (referred to the circuit of Fig. 4.41): $C_1 = 3.20$ pF, $C_2 = 0.58$ pF, $L_2 = 9.44$ nH, $C_3 = 5.02$ pF, $C_4 = 1.73$ pF, $L_4 = 6.87$ nH, $C_5 = 2.41$ pF. Filter implementation was realized by means of two series connected OCSRRs (etched in the central strip) cascaded between electrically short (to avoid the parasitic effects of the series inductance) transmission line sections with a metallic patch etched in the back substrate side and connected to the ground planes by means of vias. These patches are necessary to obtain the high required values of the shunt capacitors.

The dimensions of the metallic patches are inferred from the EM simulation of the *S*-parameters of the short CPW transmission line section with the metallic patch below it. From these results, the shunt (capacitive) reactance of the π-circuit of such transmission line section can be obtained through standard formulas linking the *S*-parameters and *Z*-parameters (see Appendix C). Then, the capacitance is extracted and compared to the nominal value. The procedure is repeated (by modifying the patch dimensions) until good agreement results. In practice, the length, l_P, of the patch was modified, while its width was set to a fixed value ($w_P = 15.84$ mm) [80].

FIGURE 4.40 (*Continued*) $e = 0.49$ mm, $g = 7.71$ mm, $i = 2.19$ mm, and $l = 19.4$ mm. The OCSRR dimensions are $r_{ext} = 1.95$ mm, $c = 0.16$ mm, and $d = 0.6$ mm, where r_{ext}, c, and d are the external radius, width, and separation of the rings. All the meanders have a width of 0.16 mm. The interdigital capacitors have a width and separation between fingers of 0.16 mm. The radius of the vias is of 0.15 mm. The considered substrate is the *Rogers RO3010* with thickness $h = 0.254$ mm and measured dielectric constant $\varepsilon_r = 10.5$. Reprinted with permission from Ref. [35]; copyright 2010 IEEE.

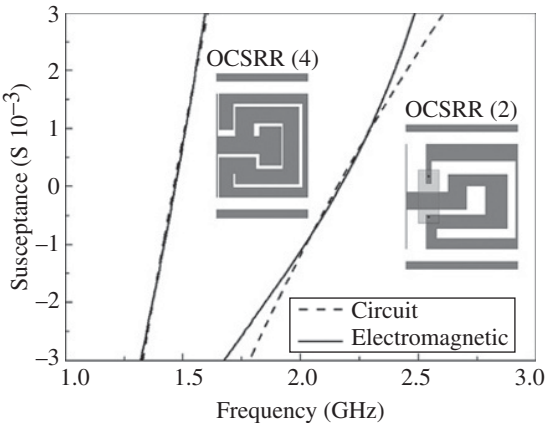

FIGURE 4.42 Susceptance of the two series connected parallel resonators of the designed elliptic-function lowpass filter. The susceptance inferred by means of EM simulation was obtained from the optimized layout topologies included in the figure. The *Rogers RO3010* substrate with measured dielectric constant $\varepsilon_r = 11.5$ and thickness $h = 0.635$ mm was considered. Reprinted with permission from Ref. [80]; copyright 2009 IEEE.

The dimensions of the OCSRRs are determined by forcing their resonance frequencies to the required values and by forcing the susceptance slopes to be identical to those of the lumped element resonators (of the elliptic-function model) at resonance. Depending on the values of the resonator inductance and capacitance, it is necessary to substantially modify the topology of the OCSRR in order to obtain the desired values of the elements. Thus, the formulas that link the geometry of the OCSRR and the element values are only used as reference. Optimization is required to provide a good description of the resonators in the vicinity of resonance. Figure 4.42 depicts resonator's susceptance for the two parallel resonators of the filter of Figure 4.41 in the vicinity of resonance. The susceptances that have been inferred from EM simulation of the optimized OCSRR topologies (shown in the inset) are also depicted in this figure. As required, there is good agreement between the two pair of curves in the vicinity of resonance.

The layout and photograph of the fabricated lowpass filter are depicted in Figure 4.43. The device was fabricated on the *Rogers RO3010* substrate with measured dielectric constant $\varepsilon_r = 11.5$ and thickness $h = 0.635$ mm. Besides the patch capacitances, there is an additional strip on the back side of the substrate that connects (through metallic vias), the external metallic regions of OCSRR (2) (the one which exhibits the upper resonance frequency). With this strategy, a parasitic slot mode that is otherwise generated in this resonator is suppressed, as revealed from the simulated magnetic currents (not shown). This parasitic mode obscures the first resonance frequency of the OCSRR (2). Thus, by etching such additional metallic strip, the stop band filter response is improved, and the two transmission zeros can be clearly identified. The simulated and measured frequency responses of the device are also shown in Figure 4.43. The circuit simulation of the model of Figure 4.41 with the above

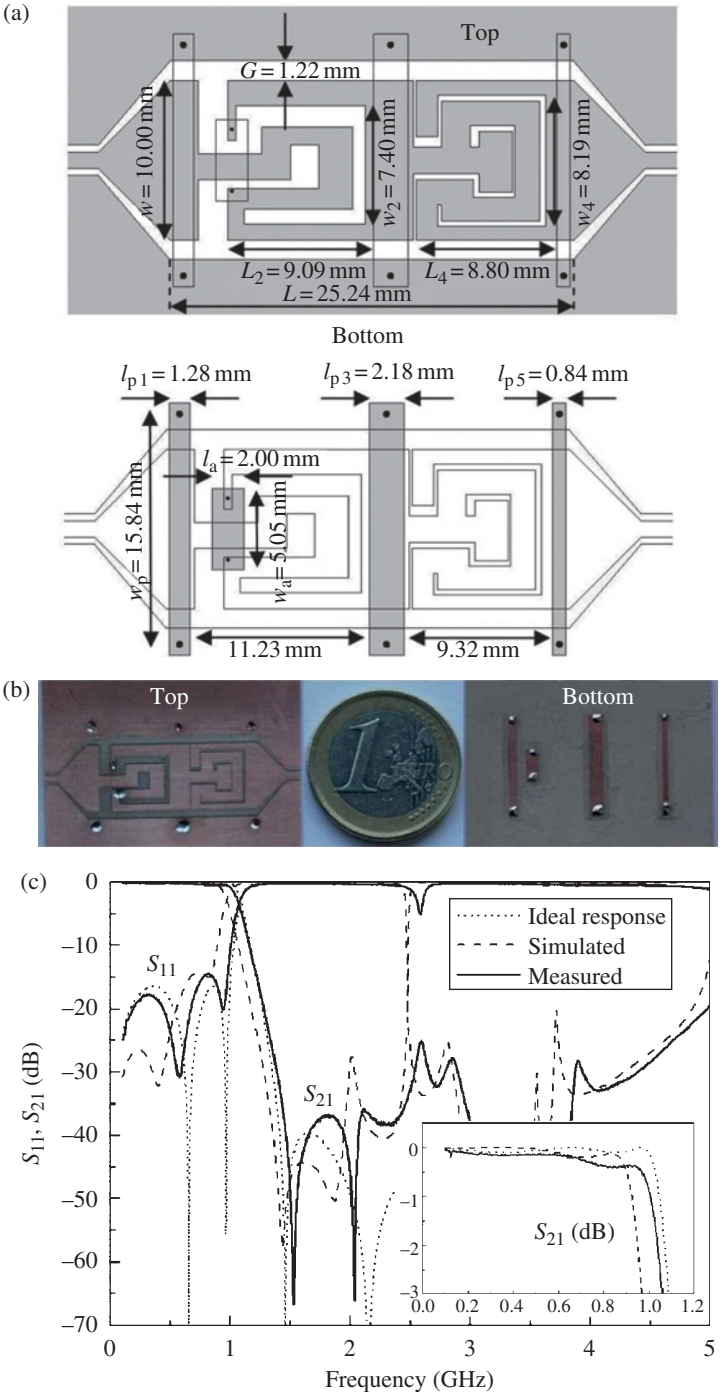

FIGURE 4.43 Layout (a), photograph (b), and simulated and measured frequency response (c) of the fabricated OCSRR-based lowpass filter. The ideal elliptic-function response is also depicted. The detail of the in-band insertion loss is depicted in the inset. Reprinted with permission from Ref. [80]; copyright 2009 IEEE.

TABLE 4.3 Comparison of split-ring elliptic lowpass filters

Reference	Pass-band IL (dB)	Pass-band RL (dB)	Stop-band rejection (up to $2f_c$) (dB)	Electrical size
[89]	<1	N.A.	>35	$0.52\lambda \times 0.27\lambda$
[90]	<0.7	>9	>32	$1.2\lambda \times 0.26\lambda$
Figure 4.43	<0.4	>14	>35	$0.13\lambda \times 0.086\lambda$

indicated element values (corresponding to the ideal elliptic-function response) is also depicted the figure. The agreement between experimental data and the elliptic function response is good up to approximately 2 GHz. At higher frequencies, the mismatch is due to the fact that the lumped element models of the different filter elements (OCSRRs and shunt capacitors) fail. Measured insertion losses in the pass band differ in less than 0.3 dB to the ideal response, and return losses are better than 14 dB. The frequency response exhibits a sharp cutoff, with a stop band rejection better than 25 dB up to roughly 4.5 GHz. It is also remarkable that filter length is small, that is, 2.5 cm, which corresponds to 0.13λ, where λ is the guided wavelength at the cutoff frequency. This combination of size (relative to the filter cutoff frequency) and performance (especially for which concerns the width of the stop band) is not easily found in other elliptic lowpass filters (see for instance [81–88]). Moreover, the electrical size of this lowpass filter is much smaller than the size of other lowpass filters based on split rings, such as CSRRs [89, 90]. The dimensions and performance of these latter filters and the filter of Figure 4.43 are compared in Table 4.3.

In summary, OCSRRs provide a good solution for the implementation of compact elliptic function lowpass filters in CPW technology. OCSRR-based lowpass filters in microstrip technology are reported in Ref. [91]. Although these filters are very selective and spurious free up to high frequencies, they are merely designed by cascading identical unit cells and therefore they do not give standard filter responses.

4.2.4 Leaky Wave Antennas (LWA)

Leaky wave radiation in periodic structures was succinctly considered in Chapter 2.[26] Leaky wave antennas (LWAs) can be defined as guiding structures with the wave radiating, or leaking, along the structure. The topic of LWAs has been in steady development for many years, and there are several excellent sources that are recommended to the interested reader on the topic [92–96]. Nevertheless, the field has been activated in recent years, especially for planar LWAs, due to the advent of metamaterials and metamaterial transmission lines [97–99]. In this subsection, the objective is to point out the potential of CRLH transmission lines for the implementation of planar LWAs,

[26] In this subsection, there are general antenna concepts not covered in any appendix to avoid an excessively long book. The author recommends general textbooks on antennas to those readers not familiarized with the topic. Nevertheless, there are several references on the specific topic of LWAs in this subsection.

and to highlight some advantages and properties of such CRLH-based antennas over other LWAs.

Traditionally, one-dimensional LWAs have been divided in two categories: uniform and periodic. In uniform LWAs, the guiding structure is uniform along the direction of propagation, and the structure supports fast waves with respect to free space, so that the complex wavenumber of the leaky mode ($k_n = \beta - j\alpha$) has a phase constant satisfying $0 < \beta < k$, k being the free space wavenumber. Typically, uniform LWAs only radiate in the forward direction since $\beta > 0$, and broadside radiation is not possible in conventional uniform LWAs. Moreover, uniform LWAs, such as microstrip antennas [100–102], typically require complex feeding structures in order to excite the required leaky mode and prevent the excitation of the dominant (slow-wave) microstrip mode.

Periodic LWAs are based on guiding structures with slow waves as compared to free space (i.e., $\beta > k$), where leaky wave radiation is achieved by introducing periodicity along the propagation direction. As studied in Chapter 2, due to periodicity the fields in these periodic structures are characterized by space harmonics with wavenumbers given by (2.6), and the structure may radiate if the leaky wave condition ($|\beta_n| < k$) is satisfied for any of the space harmonics (see Fig. 2.2).[27] In periodic LWAs, the fundamental mode does not radiate. Periodic LWAs can either radiate in the forward or backward direction since the phase constant of the $n = -1$ space harmonic can either be positive or negative. This is a fundamental difference of periodic LWAs, as compared to uniform antennas. However, in general, the presence of gaps at periodic frequencies prevents broadside radiation as a leaky wave structure [103, 104]. In practice, continuous frequency scanning from backward to forward direction is not possible due to the lack of radiation over the frequency gaps.[28] Periodic bidirectional LWAs (fed in the center to create a bidirectional leaky wave) can, however, radiate at broadside as an LWA by operating slightly away from the broadside frequency, so that $\beta_{-1} > 0$ or $\beta_{-1} < 0$. In this case, a bidirectional beam is created in which the beam from each half of the structure is slightly deviated from broadside. However, the combination of the two beams results in a symmetrical broadside beam.

Contrarily to resonant antennas, where dimensions scale with the operating frequency, the length of the leaky wave structure in LWAs (uniform or periodic) is related to the antenna directivity. Indeed, one important feature of LWAs is that they can achieve a high directivity with a simple structure, without the need for a complicated and costly feeding network as typically used in phased arrays. Directivity increases with the length of the LWA provided the leakage factor α is small enough so that the guided power is not completely leaked along the structure (i.e., it is partially absorbed by a matched load). Under these conditions, the radiation aperture is given

[27] In the analysis carried out in Section 2.2 to obtain the leaky wave condition, the attenuation constant α was neglected. Hence $k_n = \beta_n$, and for that reason the leaky wave condition was expressed as $|k_n| < k$.

[28] The stop band that occurs when the beam is scanned at broadside is known in the literature as open stopband region. In it, the radiated power drops substantially. However, there are strategies to effectively close this region and achieve leaky wave radiation at broadside in periodic structures [103, 104].

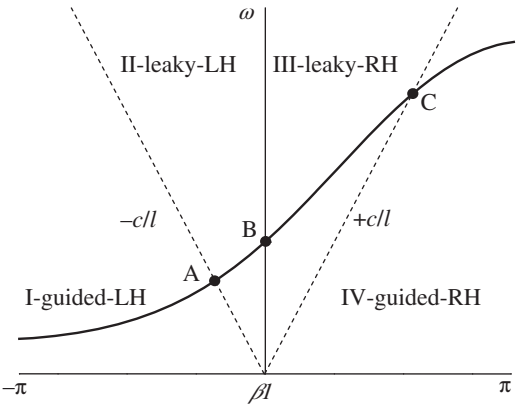

FIGURE 4.44 Typical dispersion diagram of a balanced CRLH transmission line and indication of the four main regions (enumerated I, II, III, and IV) and the relevant points separating such regions. A, B, and C points correspond to backfire, broadside, and endfire leaky wave radiation, respectively.

by the length of the LWA, and hence a high directivity is obtained for long LWA structures.

As an alternative to periodic and uniform leaky wave structures, LWAs can be implemented by means of balanced CRLH transmission lines [97]. Indeed, balanced CRLH lines are periodic structures by nature. However, in such lines, the periodicity is much smaller than the wavelength and does not play an active role in the radiation. Balanced CRLH-based LWAs radiate from the fundamental ($n = 0$) space harmonic, and essentially they behave as uniform leaky wave structures in the sense that they are homogeneous one-dimensional media.[29] Therefore, CRLH-based LWAs may be considered to belong to the category of uniform LWAs despite the fact that they are structurally periodic. To distinguish them from conventional uniform LWAs, CRLH LWAs can be referred to as quasi-uniform LWAs [96].

According to the typical dispersion of a CRLH transmission line (reproduced in Fig. 4.44), it is clear that there are regions where the dispersion curve lies in the fast wave region. Therefore, open CRLH transmission lines can be used as LWAs. Although the balance condition is not strictly necessary, by balancing the line it is possible to achieve continuous frequency scanning from backward to forward directions, including broadside radiation at the transition frequency, ω_o. Thus, balanced CRLH LWAs radiate from the fundamental mode and exhibit backfire-to-endfire capability. This is an important feature of CRLH LWAs, which is not achievable with their conventional uniform or periodic counterparts (although, as mentioned before, there are strategies to mitigate the effects of the open stop bands

[29] Although it was stated in Chapter 3 that, in general, periodicity and homogeneity are not necessary for the implementation of metamaterial transmission line-based circuits, CRLH-based LWAs are implemented by homogeneous periodic structures.

in periodic LWAs). The fact that CRLH LWAs operate at the fundamental mode is important since the feeding structures do not need to be complex (a simple transmission line suffices).

The first implementation of a CRLH LWA exploiting the backward-to-forward radiation capability was presented in Ref. [97], and consisted of a 24-unit cell microstrip line periodic-loaded with series interdigital capacitors and shunt-connected grounded stubs. The structure is the one depicted in Figure 3.27 (substrate parameters and dimensions are given in Ref. [97]). The phase and attenuation constants of this structure, as well as the radiation patterns at different frequencies, are depicted in Figure 4.45. For this design, the LH and RH guided-wave regions, designated as I and IV, respectively, in the figure, extend to frequencies below 3.1 GHz and above 6.3 GHz. Region II is the backward radiated region (with $|\beta| < k_o$ and $\beta < 0$), extending from 3.1 up to 3.9 GHz, and region III is the forward radiated region (with $|\beta| < k_o$ and $\beta > 0$), extending from 3.9 up to 6.3 GHz. The radiation patterns at the considered frequencies are consistent with the dispersion characteristics of the LWA, and confirm the frequency scanning capability of the designed antenna. At this point, it is important to mention that backward leaky wave radiation in metamaterial transmission lines was demonstrated almost simultaneously in Ref. [98] (see Chapter 3), by considering a CPW transmission line loaded with series capacitive gaps and shunt connected (inductive) strips. However, in such antenna, backward-to-forward frequency scanning capability was not demonstrated. The same authors reported a forward CPW LWA consisting of a similar structure, but only loaded with series capacitive gaps [99]. It was argued in Refs. [98, 99] that the radiating elements in the reported CPW-based LWAs are the capacitive gaps, which cause a backward [98] or forward [99] transverse magnetic wave front. Conversely, the pairs of inductive strips support opposite (antiparallel) currents, causing cancelation in the far field (E-plane) due to line symmetry and even excitation of the fundamental CPW mode.

CPW transmission lines loaded with pairs of SRRs and shunt-connected inductive strips do also exhibit fast wave regions for the fundamental ($n = 0$) mode. However, such structures are inefficient to produce leaky wave radiation from the fundamental mode due to far field cancelation caused by opposite currents. That is, due to line symmetry and even mode excitation (CPW mode), the symmetry plane of the structure is a magnetic wall, and the magnetic currents in the slots are antiparallel.[30] In order to achieve efficient leaky wave radiation in SRR-based CPW transmission lines, a strong asymmetry can be forced by removing the set of SRRs present at one side of the symmetry plane of the line. This allows reducing far field cancelation from the

[30] The far-field cancellation effect due to antiparallel magnetic currents can be explained by considering a magnetic current (that of a single slot) parallel and close to a perfect magnetic conductor (PMC), located at the symmetry plane of the CPW transmission line. The PMC generates an antiparallel image current, causing far field cancellation. The effect is similar to the antiparallel electric (image) current generated by a perfect electric conductor (PEC), preventing the radiation from an electric dipole, if it is parallel oriented and closely located to the PEC.

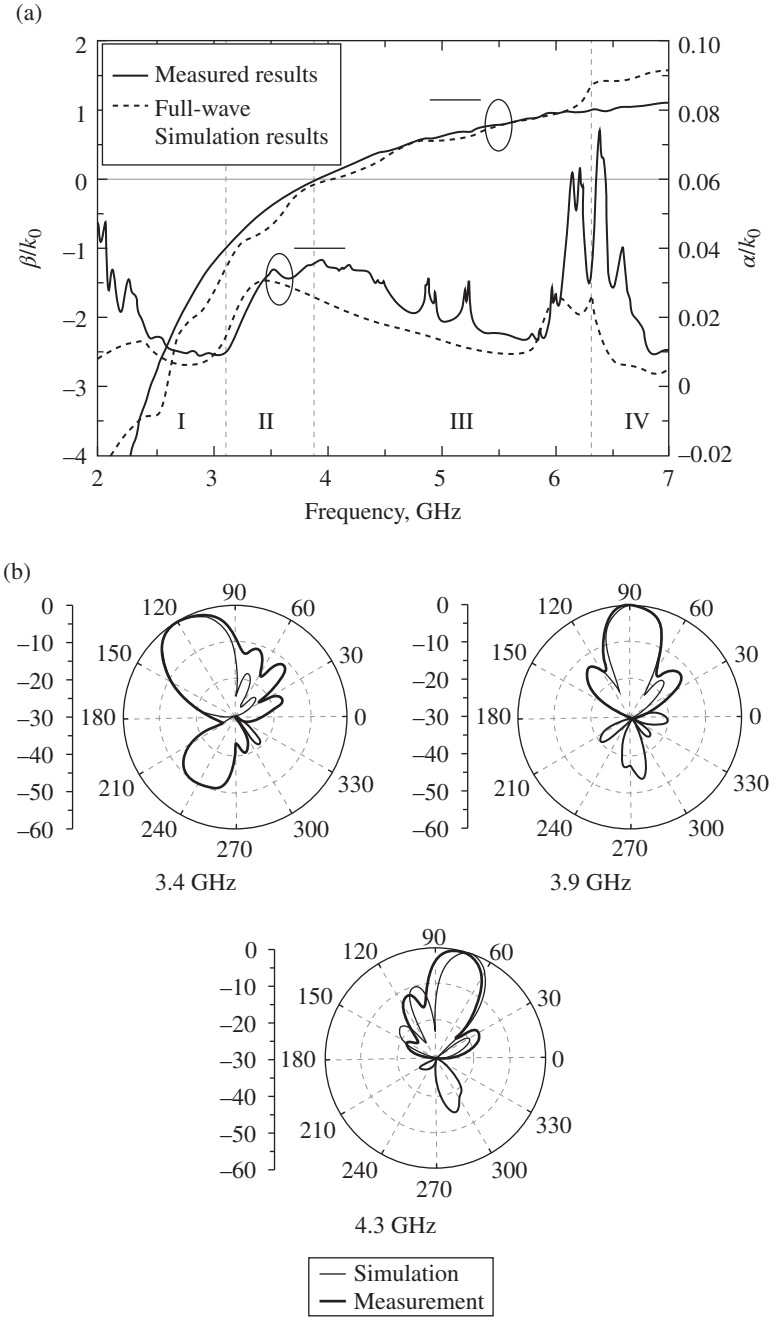

FIGURE 4.45 (a) Dispersion characteristics of the structure of Figure 3.27; (b) radiation patterns (E-plane) for the indicated frequencies. Reprinted with permission from Ref. [97]; copyright 2002 IET.

magnetic current balance between both slots, providing the excitation of the slot line mode, which results in an important contribution to increase leaky wave radiation [105].

Alternatively to the previous strategy, efficient leaky wave radiation can be achieved by loading a slot line with SRRs and shunt inductive strips [106]. With such a structure, it is possible to scan the radiation angle with frequency by balancing the line. The design of the structure starts by conceiving a balanced SRR/strip-loaded CPW with sufficiently distant slots (wide central strip) to minimize the field coupling between the slots. Under these conditions, the CPW can be viewed as a pair of two independent slot lines sharing the same substrate, with antiparallel slot magnetic currents. Therefore, it is expected that a symmetric CPW with a wide central strip exhibits similar propagation characteristics than the slot line resulting by removing one half of the CPW structure. With this in mind, a balanced SRR/strip-loaded CPW with the transition frequency at $f_o = 2.5$ GHz was designed in Ref. [106]. The phase constant inferred from EM simulation of the structure (unit cell), depicted in Figure 4.46, is roughly the same as the phase constant corresponding to the slot line that results by removing one half of the CPW transmission line (the fabricated structure is depicted in Fig. 4.47a). Unlike the phase constant, the analysis of a single-unit cell is inaccurate for the determination of the attenuation constant α of leaky periodic structures. This is due to mutual coupling and edge effects. However, as the number of the considered unit cells increases, edge effects become less significant and the obtained attenuation constant is more accurate [107]. Therefore, in order to determine the required number of unit cells, N, the attenuation constant was computed by simulating an N-element two-port structure, using the *Agilent Momentum* commercial software. Figure 4.47b shows the normalized attenuation constant α/k_0 at the transition frequency. It can be observed that more than 15 elements are required to achieve

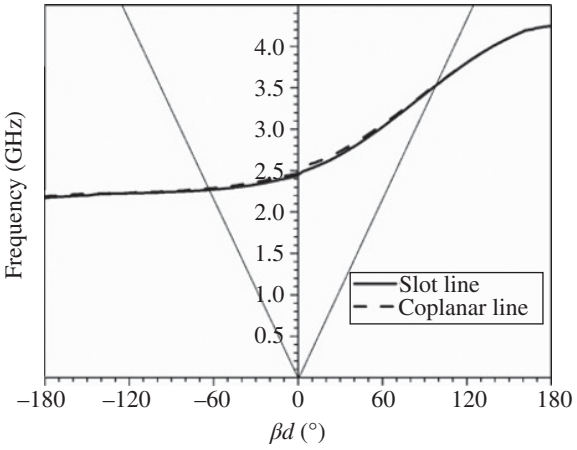

FIGURE 4.46 Dispersion diagram of the SRR/strip-loaded CPW unit cell (dashed line) and SRR/strip-loaded slot line unit cell (solid line) inferred from EM simulation.

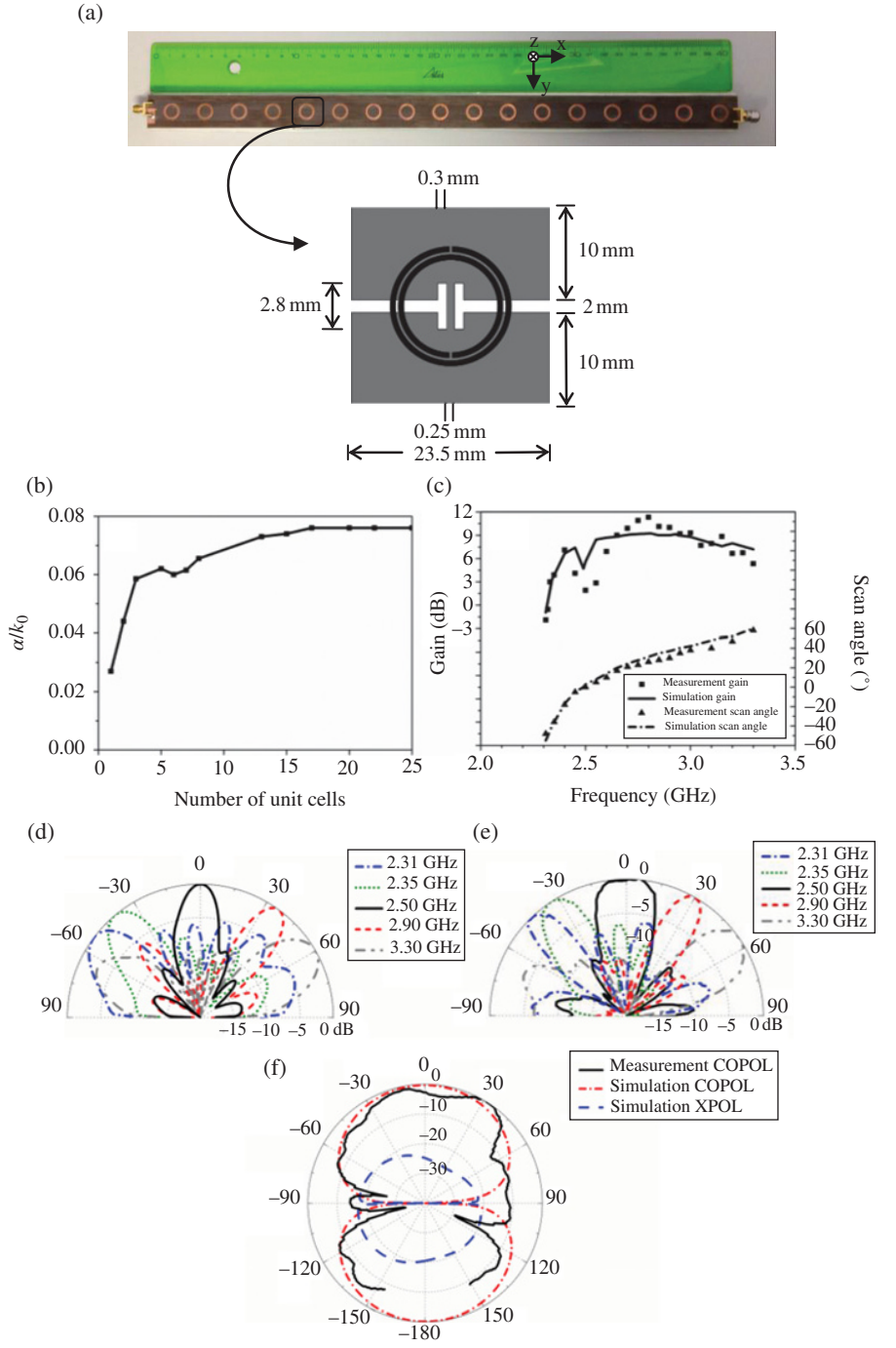

FIGURE 4.47 Fabricated 17-cell SRR/strip-loaded slot LWA and antenna performance. (a) Photograph and relevant dimensions of the unit cell, (b) attenuation constant versus the

convergence to a value of $\alpha/k_0 = 0.076$. This value was used to obtain the length of the LWA from the expression for the power flow along a lossy periodic structure with periodicity d

$$P_n = P_o e^{-2\alpha n d} \tag{4.51}$$

where P_0 is the power delivered to the LWA, P_n is the power at the nth terminal of the periodic structure and d is the unit cell length. For 95% of the power dissipated before reaching the antenna termination and using the converged value of $\alpha/k_0 = 0.076$, the required number of unit cells is $N = 17$.

According to simulation, the characteristic impedance of the loaded line at the transition frequency is $Z_o = 150\ \Omega$. This impedance was matched to the $50\ \Omega$ connector using a semilumped microstrip matching network, connected to the slot line by means of a via hole. The measured and simulated gains are depicted in Figure 4.47c, with a maximum measured gain of 7.1 dB and 11.3 dB for the LH and RH bands, respectively. There is a relatively good agreement between measured and simulated data. The angle of the maximum beam θ_m as a function of frequency is also plotted in Figure 4.47c, showing good agreement between measurement and simulation. The measured backward to forward scanning range is from -50° to $+60^\circ$ while maintaining an acceptable gain level. The simulated and measured normalized radiation patterns are shown in Figure 4.47d and e. As it can be appreciated, backward, broadside and forward leaky wave radiation is obtained as frequency increases from the LH to the RH frequency bands. The simulated and measured orthogonal pattern at 2.5 GHz is depicted in Figure 4.47f. It can be observed that while the radiated beam is directive in the *xz*-plane (see Fig. 4.47d and e), it is fat in the perpendicular direction (*yz*-plane), thus resulting in a fan beam.

In microstrip technology, LWAs loaded with CSRRs have been recently demonstrated [108]. There are many other CRLH-based LWAs reported in the recent literature. It is not possible to cover all of them in a general textbook like the present one. However, let us mention to finish this subsection that besides microstrip, CPW and slot-line technology, CRLH LWAs have been also demonstrated using CPSs [109] and SIW technology [110, 111] (these antennas will be analyzed in the last chapter, where a section is devoted to SIW technology). Electrically scanned (tunable) LWAs, with fixed frequency but variable radiation angle [112, 113], and dual-band LWAs based on E-CRLH lines have also been reported [111, 114]. Finally, active CRLH LWAs consisting of CRLH line sections interconnected through amplifiers have been

FIGURE 4.47 (*Continued*) number of unit cells at 2.5 GHz, (c) simulated and measured antenna gain and scanning angle, (d) simulated normalized radiation patterns at the longitudinal plane, (e) measured normalized radiation patterns at the longitudinal plane, and (f) simulated and measured orthogonal plane radiation pattern of the proposed LWA at 2.5 GHz. The antenna was fabricated on the *Arlon Cuclad 250XL* substrate with dielectric constant $\varepsilon_r = 2.43$, loss tangent $\tan\delta = 0.002$, and thickness $h = 0.49$ mm. Reprinted with permission from Ref. [106]; copyright 2013 IEEE.

presented in Ref. [115]. Since the amplifiers regenerate the power progressively leaked out of the structure in the radiation process, the effective aperture of the antenna is increased, and hence the directivity and gain are enhanced.

4.2.5 Active Circuits

The CRLH transmission lines or some of the considered CRLH-based passive circuits studied in the previous subsections can be combined with active elements such as diodes and transistors, or with amplifiers, for the implementation of RF/microwave circuits with enhanced performance or functionality. Thus, for instance, dual-band balanced mixers implemented by means of dual-band CRLH-based hybrid couplers [116], dual-band class-E power amplifiers with CRLH-based impedance matching networks [117], and active LWAs [115], among others, have been reported. In this subsection, the aim is to demonstrate the potential of CRLH transmission lines for the implementation of active microwave circuits, on the basis of two types of circuits: distributed amplifiers with enhanced functionalities and dual-band recursive active filters.

4.2.5.1 Distributed Amplifiers Distributed amplification was proposed as a means of improving the gain-bandwidth product [118]. Essentially, distributed amplifiers consist of a pair of actively coupled transmission lines, the gate line, and the drain line. Active coupling is achieved through the distributed transconductance of a set of transistors (normally field-effect transistors or FETs) with their gates and drains connected to the gate and drain lines, respectively. By injecting the input signal to any of the ports of the gate line (the other one being matched), the signal in the drain line is amplified by virtue of the distributed transconductance [119]. This results in a certain gain between the input and the so-called forward and reverse output ports.[31] Since the fifties of the past century, there have been many notable contributions to the field of distributed amplifiers. Among them, those amplifiers that first used FETs [120, 121], the first monolithic implementations based on AsGa-FETs (achieving bandwidths beyond 10 GHz) [122–124], and the dual-fed concept to improve device gain Ref. [125], are worth mentioning. More recently, several works have been focused on improving the amplifier bandwidth and efficiency [126, 127], and notable achievements have been reported in the field of distributed mixers [128, 129], formerly reported in Ref. [130, 131].

In all the previous reported distributed amplifiers and mixers, forward (RH) gate and drain transmission lines are used. The first structure that made use of LH transmission lines was presented by Eccleston in 2005 [132]. However, the aim in that work was to reduce device dimensions, rather than using the unusual dispersion characteristics of LH lines. The combination of distributed amplification with the nonlinear dispersive behavior of CRLH transmission lines was first pointed out in Ref. [133]. This work opened the path toward the design of distributed amplifiers with a radically new

[31] The forward and reverse output ports are those ports of the drain line located in the opposite and in the same extreme, respectively, than the input (gate line) port.

intrinsic behavior. Thanks to the controllability of the dispersion in the gate and drain lines, it is possible, for instance, to achieve maximum gain at arbitrary frequencies in the forward and reverse ports, and thus achieve a dual-band/diplexing action, avoiding the use of additional costly components. In other words, the introduction of CRLH lines in distributed amplifiers, rather than improving the performance of the conventional counterparts, has generated novel and interesting functionalities for these devices. Distributed amplifiers based on metamaterial transmission lines constitute a genuine example of devices designed through dispersion and impedance engineering. Such devices have been designated as metadistributed amplifiers to highlight the fact that they are based on metamaterial structures (CRLH transmission lines). CRLH transmission lines can also be introduced in distributed mixers (meta-distributed mixers) [134], but the analysis of these devices is out of the scope of this book.

To understand the high potential of CRLH transmission lines to the implementation of distributed amplifiers with advanced functionalities, it is necessary to briefly review the principles behind distributed amplification and to derive some useful expressions that link the amplifier gain to the main device parameters, including the phase constants of the drain and gate lines. Such expressions will then be analyzed to point out several amplifier functionalities, related to the dependence of the gain in the forward and reverse output ports with frequency. Finally, an illustrative implementation and its characterization will be reported.

Principle of Distributed Amplification Let us introduce the principle of distributed amplification by considering a lossless, unilateral, and continuous model for the elemental cell of the distributed amplifier. It consists of two lossless transmission lines with active unilateral coupling through a distributed transconductance, as depicted in Figure 4.48a [120, 135]. In this basic cell, $\beta_g(\omega)$ and $\beta_d(\omega)$ are the phase constants of the gate and drain lines, respectively, and Z_g and Z_d the corresponding characteristic impedances. The per-unit-length transconductance, $g_{m,}$ provides a current in the drain line that depends on the voltage on the gate line, $V_{gs}(z)$. By considering the input port of the distributed amplifier to be one of the ports of the gate line, the ratio of the output power in the forward port (see Fig. 4.48b), P_o^{fwd}, to the input power, P_i, is called forward gain, whereas the reverse gain is the ratio of the power collected in the reverse port, P_o^{rev}, to the input power, that is,

$$G_{fwd} = \frac{P_o^{fwd}}{P_i} \tag{4.52a}$$

$$G_{rev} = \frac{P_o^{rev}}{P_i} \tag{4.52b}$$

Let us consider that all the ports of the amplifier are matched, so that no reflected waves are generated in the structure. Under these conditions, the output current in the forward port is given by the contribution of all the source currents along the structure, namely

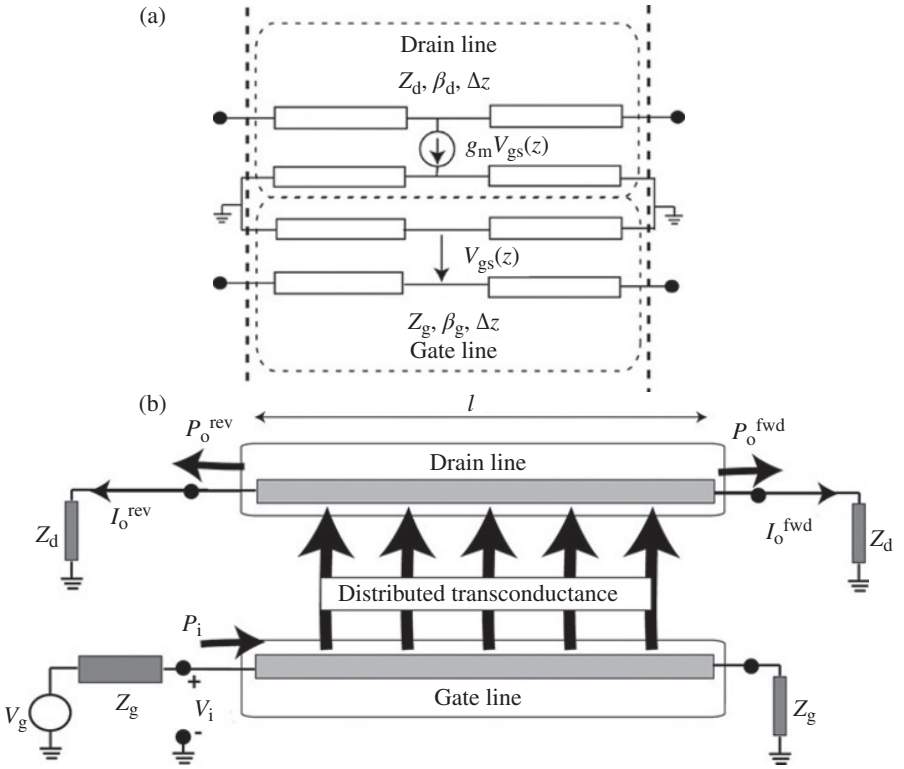

FIGURE 4.48 Basic cell (a) and scheme (b) of the continuous unilateral distributed amplifier. Reprinted from Ref. [135], with permission from the author.

$$I_o^{fwd} = -\int_o^l V_{gs}(z) g_m e^{-j\beta_d(\omega)(l-z)} dz = -\int_o^l V_i e^{-j\beta_g(\omega)z} g_m e^{-j\beta_d(\omega)(l-z)} dz \tag{4.53}$$

where V_i is the input voltage. The integral in (4.53) gives[32]

$$I_o^{fwd} = -V_i g_m l \cdot \mathrm{sinc}\left(\left(\beta_g(\omega) - \beta_d(\omega)\right)\frac{l}{2}\right) \cdot e^{-j\left(\beta_g(\omega)+\beta_d(\omega)\right)\frac{l}{2}} \tag{4.54}$$

From (4.54) the power gain is found to be

$$G_{fwd} = \frac{\left|I_o^{fwd}\right|^2}{4\left|V_i\right|^2} Z_g Z_d = \frac{g_m^2 l^2 Z_g Z_d}{4} \mathrm{sinc}^2\left(\left(\beta_g(\omega) - \beta_d(\omega)\right)\frac{l}{2}\right) \tag{4.55}$$

[32] The sinc function is defined as $\mathrm{sinc}(x) = \sin(x)/x$.

The power gain in the reverse port is derived by simply changing the signs in the exponential function of (4.53), that is,

$$I_{\mathrm{o}}^{\mathrm{rev}} = -\int_{\mathrm{o}}^{l} V_{\mathrm{gs}}(z) g_{\mathrm{m}} e^{-j\beta_{\mathrm{d}}(\omega)(z-l)} dz \tag{4.56}$$

This gives

$$G_{\mathrm{rev}} = \frac{\left|I_{\mathrm{o}}^{\mathrm{rev}}\right|^2}{4\left|V_{\mathrm{i}}\right|^2} Z_{\mathrm{g}} Z_{\mathrm{d}} = \frac{g_{\mathrm{m}}^2 l^2 Z_{\mathrm{g}} Z_{\mathrm{d}}}{4} \mathrm{sinc}^2\left(\left(\beta_{\mathrm{g}}(\omega) + \beta_{\mathrm{d}}(\omega)\right)\frac{l}{2}\right) \tag{4.57}$$

According to this continuous model, the frequency behavior of the distributed amplifier is exclusively determined by the phase constants of the gate and drain lines. The maximum power gain for the forward and reverse ports is given by

$$G_{\mathrm{MAX}} = \frac{g_{\mathrm{m}}^2 l^2 Z_{\mathrm{g}} Z_{\mathrm{d}}}{4} \tag{4.58}$$

and it depends on the values of g_{m}, l, Z_{g}, and Z_{d}. Notice that, according to expressions (4.55) and (4.57), the maximum power gain for the forward port is obtained for those frequencies satisfying $\beta_{\mathrm{g}}(\omega) = \beta_{\mathrm{d}}(\omega)$, whereas for the reverse port the maximum power (i.e., maximum gain) is collected when $\beta_{\mathrm{g}}(\omega) = -\beta_{\mathrm{d}}(\omega)$. In distributed amplifiers implemented by means of forward transmission lines (conventional distributed amplifiers), the latter condition ($\beta_{\mathrm{g}}(\omega) = -\beta_{\mathrm{d}}(\omega)$) can only be satisfied at DC, where $\beta_{\mathrm{g}}(\omega) = \beta_{\mathrm{d}}(\omega) = 0$. Hence, the maximum power gain for the reverse port occurs at DC, and the power at the reverse port exhibits a lowpass behavior. If the gate and drain lines are identical (i.e., they have the same phase constant), the gain in the forward port takes the value given by (4.58) at all frequencies. Thus, distributed amplifiers ideally exhibit an infinite gain-bandwidth product (forward port). In practice, this of course does not occur since discretization due to the presence of transistors at periodic positions in the lines limits amplifier bandwidth. Bandwidth is also limited by potentially slight differences in the phase constants of the gate and drain lines. The ideal power gains (forward and reverse ports) of a continuous distributed amplifier that result by considering conventional gate and drain lines with identical (and linear) phase constant ($\beta_{\mathrm{g}}(\omega) = \beta_{\mathrm{d}}(\omega)$) are depicted in Figure 4.49a.

Dispersion Engineering in the Drain and Gate Lines To the light of the dependence of the forward and reverse power gains with the phase constants of the gate and drain lines, it is simple to deduce that by engineering such phase constants it is possible to obtain functionalities beyond those achievable with conventional distributed amplifiers. To start, let us consider that the gate and drain lines are replaced with PLH transmission lines. If the lines are identical and exhibit a dependence of the phase constant with frequency of the type given by expression (3.41), the forward gain is independent of frequency (since $\beta_{\mathrm{g}}(\omega) = \beta_{\mathrm{d}}(\omega)$) and given by (4.58). However, since the phase

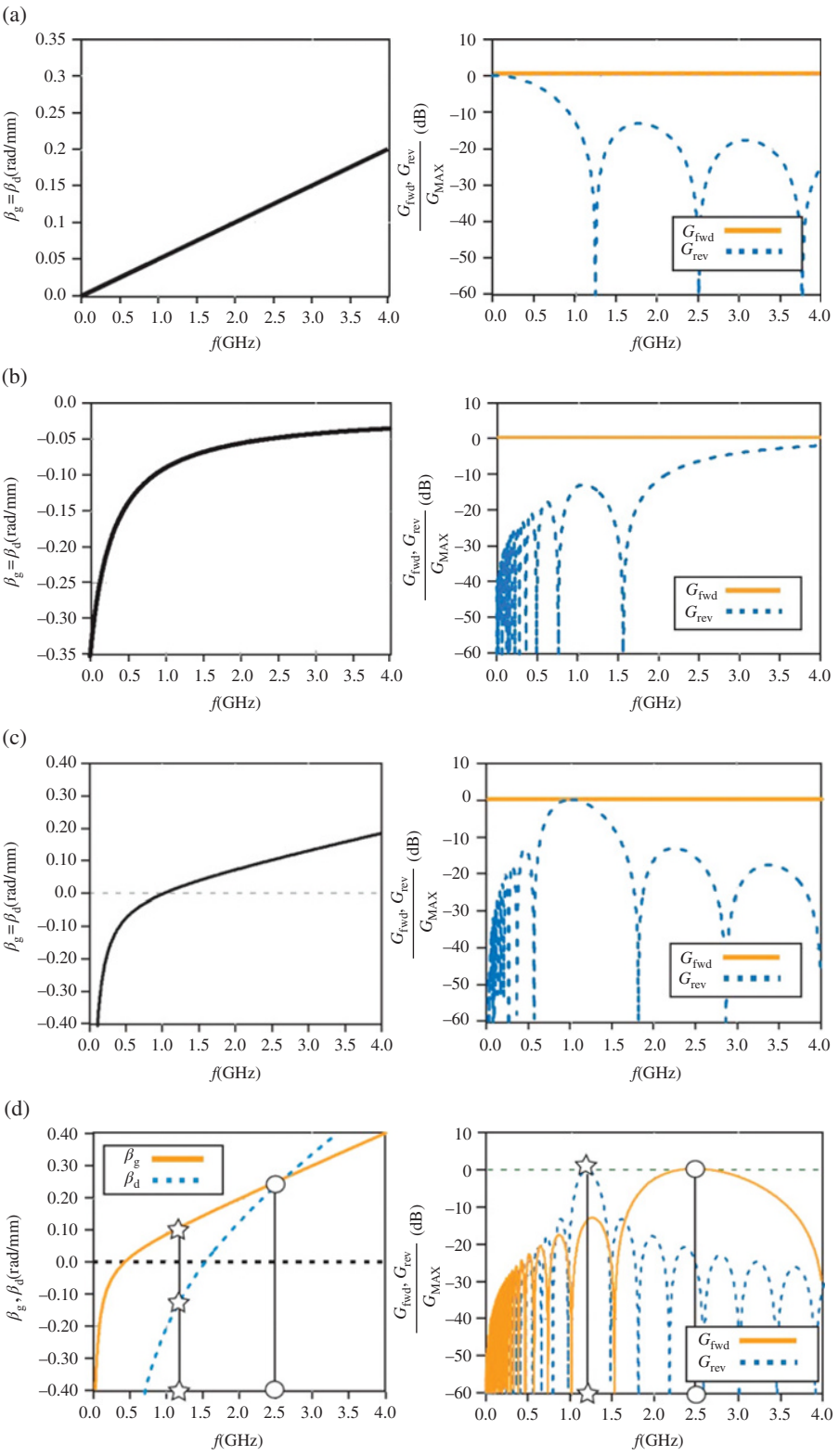
(a)
$\beta_g = \beta_d$(rad/mm)
f(GHz)
$\frac{G_{fwd}, G_{rev}}{G_{MAX}}$ (dB)
G_{fwd}
G_{rev}
(b)
(c)
(d)
β_g
β_d
β_g, β_d(rad/mm)

constant is null in the high-frequency limit, it follows that the reverse gain takes the maximum value in that limit, and hence it exhibits a high-pass behavior (this situation is illustrated in Fig. 4.49b). In practice, discretization limits the bandwidth of the forward gain since the phase constant is purely imaginary at low frequencies (expression 3.41 is valid in the long wavelength limit, that is, at high frequencies for a PLH line). On the other hand, a PLH line cannot be implemented in practice, as it was discussed in Chapter 3, with the result of a forward gain also decaying at sufficiently high frequencies.

Another interesting situation results by considering gate and drain lines with CRLH behavior. In the long wavelength limit (continuous limit), the phase constant of the CRLH transmission line is given by expression (3.59). By balancing the line ($\omega_s = \omega_p = \omega_o$) the phase constant is simplified to

$$\beta l = \frac{\omega}{\omega_R}\left(1 - \frac{\omega_o^2}{\omega^2}\right) \tag{4.59}$$

where ω_R was defined in Section (3.4.2) and ω_o is the so-called transition frequency. In this case, the reverse gain exhibits an intrinsic bandpass behavior with maximum gain at ω_o. This situation is illustrated in Figure 4.49c. Many other interesting situations arise by considering different gate and drain lines (i.e., with different CRLH-type phase constants). We will not cover all of them in the present book (the author recommends [135] for an in-depth analysis). However, let us point out the situation that results by considering the phase constants for the gate and drain lines indicated in Figure 4.49d (the corresponding normalized forward and reverse gains are also depicted in the figure). In view of this figure, both the forward and reverse power gains exhibit an intrinsic bandpass behavior. The important aspect is that by tailoring the dispersion of the gate and drain lines, it is possible to independently control the frequency where the forward and reverse gains are maximized. Therefore, such distributed amplifier exhibits a dual-band/diplexing amplifying functionality that can be of interest in numerous applications. As pointed out in Ref. [135], such diplexing capability can also be achieved through a conventional gate line and a CRLH drain line with properly engineered phase constants.

The frequency dependence of the forward and reverse gains depicted in Figure 4.49 has been inferred by introducing the considered phase constants ($\beta_g(\omega)$ and $\beta_d(\omega)$) in expressions (4.55) and (4.57). This provides the intrinsic (ideal) behavior of the continuous distributed or metadistributed amplifiers. The analysis of the discrete model

FIGURE 4.49 Phase constants of the drain and gate lines and the corresponding forward and reverse power gains for an ideal continuous unilateral distributed amplifier. (a) Forward gate and drain lines with identical phase constants, (b) backward gate and drain lines with identical phase constants, (c) CRLH gate and drain lines with identical phase constants, and (d) CRLH gate and drain lines with different phase constants. Reprinted from Ref. [135], with permission from the author.

can be found in Ref. [119, 135], and it will not be reproduced here. Nevertheless, the expressions of the forward and reverse gains for a distributed (or metadistributed) amplifier consisting of two transmission lines actively coupled through N FETs with transconductance g_m are

$$G_{fwd} = \frac{(g_m N)^2 Z_g(\omega) Z_d(\omega)}{4} \frac{\sin^2\left[\frac{N}{2}\left(\beta_g(\omega) - \beta_d(\omega)\right)\right]}{N^2 \sin^2\left[\frac{1}{2}\left(\beta_g(\omega) - \beta_d(\omega)\right)\right]} \tag{4.60}$$

$$G_{rev} = \frac{(g_m N)^2 Z_g(\omega) Z_d(\omega)}{4} \frac{\sin^2\left[\frac{N}{2}\left(\beta_g(\omega) + \beta_d(\omega)\right)\right]}{N^2 \sin^2\left[\frac{1}{2}\left(\beta_g(\omega) + \beta_d(\omega)\right)\right]} \tag{4.61}$$

Due to the similarities between (4.60), (4.61) and (4.55), (4.57), the main features relative to the continuous (ideal) distributed or metadistributed amplifiers pointed out before can be extended to the discrete structure, with exception of bandwidth, as has been discussed before (notice that the explicit dependence of the characteristic impedances of the gate and drain lines with frequency has been included in (4.60) and (4.61)). Indeed, the continuous model can be used to analyze the discrete distributed amplifier provided the frequency regions of interest are far away from the cutoff frequencies and close to the frequencies where the forward and reverse gains are maximized [135].

An Illustrative Example: Dual-Band/Diplexer Meta-Distributed Amplifier A dual-band/diplexer metadistributed amplifier, based on two actively coupled CRLH transmission lines, is reported as an illustrative example [136]. The amplifier was designed to exhibit maximum forward and reverse gains at 440 MHz and 640 MHz, respectively, with a bandwidth of approximately 100 MHz in both cases, and characteristic impedances for the drain and gate lines of 50 Ω. The CRLH lines were implemented by means of lumped elements. The element values can be inferred from the required phase constants of the CRLH lines, which in turn are determined by expressions (4.60) and (4.61). However, as pointed out in Ref. [136], it is necessary to take into account the input and output FET capacitances, which are parallel connected to the shunt capacitance of the CRLH lines (the considered active devices are *Infineon CFY-30* FET transistors). On the other hand, the shunt inductor of the CRLH lines is a short-circuit at DC, and therefore it prevents the active device from being properly biased. This problem was circumvented in Ref. [136] by series connecting a capacitor with this inductor. This capacitor allows for device biasing, but it must exhibit a very low impedance at all the significant frequencies, being effectively a short circuit for those frequencies. To achieve this, 100 pF capacitors were used in the design. Figure 4.50a depicts the scheme of the amplifier, where the dual-band/diplexing functionality is represented, and the fabricated device is shown in Figure 4.50b. The measured forward and reverse gains, depicted in Figure 4.50c and obtained for the bias

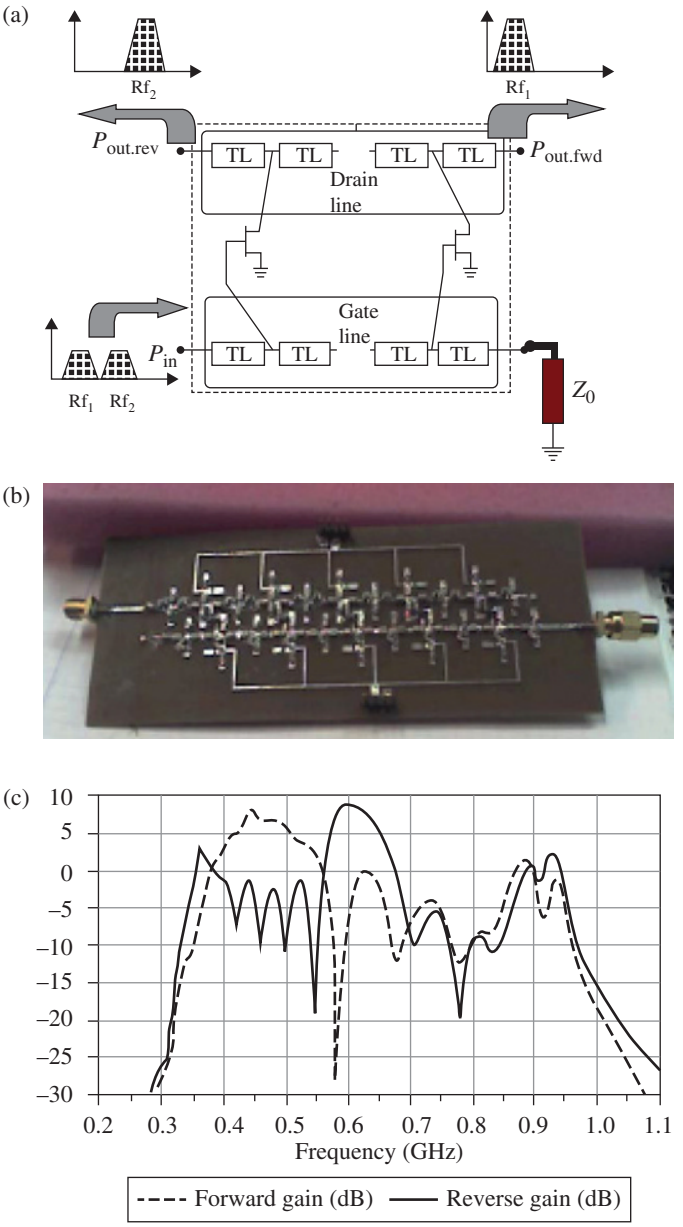

FIGURE 4.50 Scheme showing the dual-band/diplexer functionality of the designed distributed amplifier (a), photograph (b), and measured forward and reverse power gains (c). Reprinted with permission from Ref. [136]; copyright 2007 EuMA.

point defined by $V_{DS} = 3.5$ V and $V_{GS} = -0.7$ V, reveal that the required functionality is achieved. Noise measurements (not depicted here) reveal that the forward and reverse noise figures are similar to those achieved in conventional distributed amplifiers [136].

Other representative works of the recent progress in metadistributed amplifiers and mixers are given in Refs. [137–142]. The list includes distributed amplifiers integrated with CRLH LWAs [138, 141], and the first monolithic metadistributed amplifier implemented in GaN technology operative at C-band [142].

4.2.5.2 Dual-Band Recursive Active Filters Recursive active filters are a subclass of active filters based on distributed components and a feedback scheme, where the frequency selective response is generated by combining two signals: the main path signal component and a component properly weighted and delayed that constitutes the feedback [143]. The design of the filter is based on providing a certain phase response (phase delay) to the feedback section at the center frequency of the pass band. Such phase delay can be achieved by means of a transmission line section. Since the phase delay is a periodic function, it follows that recursive active filters implemented with conventional lines actually exhibit a periodic response. However, since the higher-order bands are centered at the harmonics of the fundamental frequency (i.e., not controllable), such filters are single-band devices. However, it is possible to extend the functionality of recursive active filters by replacing the conventional lines in the feedback section with CRLH transmission lines, in order to achieve a frequency response with two transmission bands (dual-band filter) [144]. In order to produce a dual-band response, the phase condition should be fulfilled at two different controllable frequencies (an inherent property of CRLH lines, as it was discussed in Section 4.2.2). Thus, the purpose of this subsection is to demonstrate that CRLH lines can be applied to the implementation of dual-band recursive active filters.

The typical schematic of a recursive active filter is depicted in Figure 4.51. The filter uses power dividers and combiners that can be implemented by means of branch line couplers with a matched load in one of the ports, as depicted in Figure 4.51. The weighting factor is achieved by means of the amplifier, whereas the phase delay in the feedback signal is obtained thanks to the transmission line in the feedback branch.

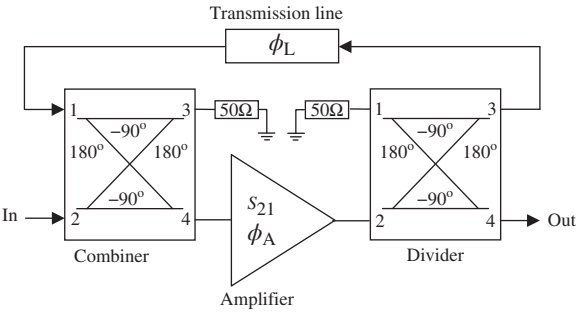

FIGURE 4.51 Bloch diagram of a first-order recursive active filter that makes use of branch line hybrid couplers for the power divider and combiner stages.

According to this scheme, the central frequencies of the filter pass bands are given by those angular frequencies, ω_o, satisfying the following phase condition (loop phase):

$$\phi_A(\omega_o) + \phi_D(\omega_o) + \phi_L(\omega_o) + \phi_C(\omega_o) = n \cdot 2\pi \tag{4.62}$$

where ϕ_A, ϕ_D, ϕ_L, and ϕ_C are the phase responses of the amplifier, power divider, transmission line section and power combiner, respectively, n being an integer number. Notice that, according to (4.62), the feedback signal and the input power signal are combined constructively (i.e., with null relative phase shift) at any of the filter-operating frequencies. Assuming that the dividers and combiners produce a −3 dB insertion loss and perfect matching between blocks, the filter transmission coefficient at ω_o is given by [144]

$$S_{21,F}(\omega_o) = \frac{1}{2} \frac{|S_{21,A}|}{|1 - 0.5 \cdot |S_{21,A}||} \tag{4.63}$$

where $S_{21,A}$ is the amplifier gain. Depending on the amplifier gain the whole structure may be unstable. This aspect is discussed in Refs. [144, 145] where it is concluded that first-order recursive filter topologies with −3 dB couplers are unconditionally unstable when using amplifier gain values over 6 dB, and potentially unstable or unconditionally stable below that value.

Although important, the stability issue is out of the scope of this subsection, focused on the potential of CRLH lines as delay lines for achieving dual-band functionality in the recursive active filters. If we assume that the phase delays given by the power combiner and divider take fixed values at the operating frequencies, expression (4.62) can be reduced to an expression only dependent on the phases of the transmission line section and the amplifier. The phase delay of a branch-line coupler is π; thus, the phase condition in (4.62) can be rewritten as follows:[33]

$$\phi_A(\omega_i) + \phi_L(\omega_i) = n \cdot 2\pi \tag{4.64}$$

where the index $i = 1, 2$ is used to designate the two desired operating frequencies of the dual-band recursive active filter. Expression (4.64) represents actually a pair of equations that have a solution provided the phase response of the considered transmission line has a nonlinear dispersion. Thus, it is obvious that by using CRLH lines in the feedback branch it is possible to achieve the dual-band functionality. As an illustrative example, Figure 4.52a depicts the dual-band recursive active filter reported in Ref. [144]. The filter response is also depicted in the figure, where the dual-band behavior can be appreciated. In Figure 4.52d the phase responses of the amplifier and transmission line stages are depicted; it can be seen that (4.64), with $n = 0$, is fulfilled at the design frequencies (0.8 GHz and 1.7 GHz). Higher-order dual-band and tunable recursive active filters are reported in Refs. [146, 147].

[33] It is assumed that the branch line coupler is also a dual-band device.

4.2.6 Sensors

Metamaterial transmission lines are also of interest for the implementation of microwave sensors with advanced properties. In microwave sensors, the sensing principle is based on the effects caused by the measured variable (temperature, humidity, pressure, position, dielectric loading, etc.) on the characteristics (phase, magnitude, resonance frequency, delay, etc.) of a feeding microwave signal.[34] For instance, a transmission line loaded with an SRR exhibits a notch in the transmission coefficient

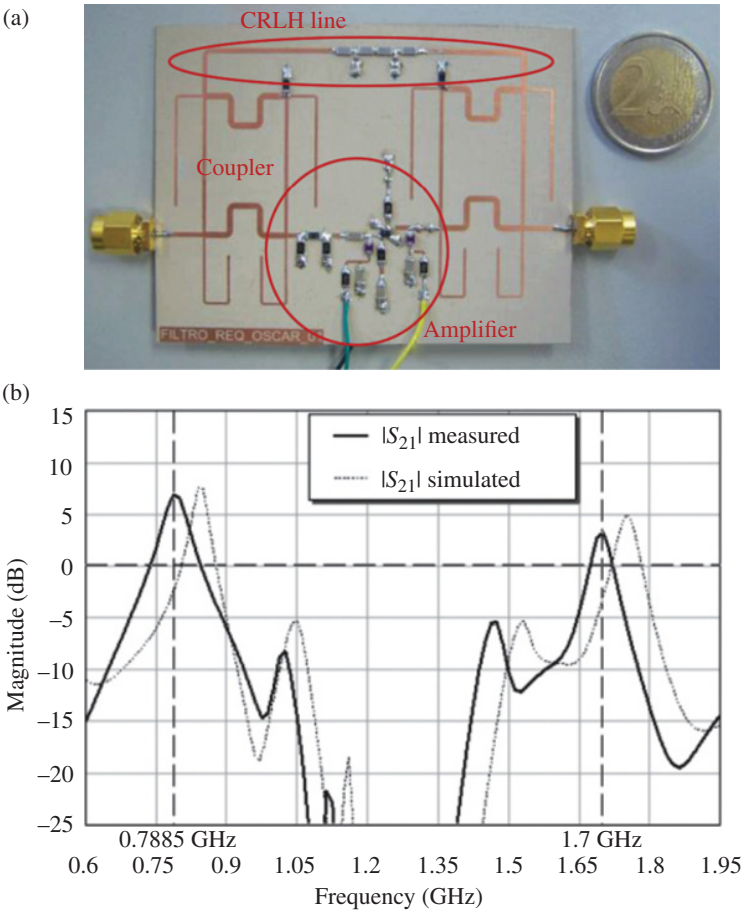

FIGURE 4.52 Dual-band recursive active filter implemented by means of a CRLH line and dual-band couplers: (a) photograph of the prototype, (b) insertion loss, (c) return loss, and (d) simulated phase response of the gain stage and feedback line. Reprinted with permission from Ref. [144]; copyright 2009 IEEE.

[34] In microwave sensors, the feeding signal can be provided by the source thorough direct (wire) connection or wirelessly. In the latter case, the devices are designated as wireless microwave sensors.

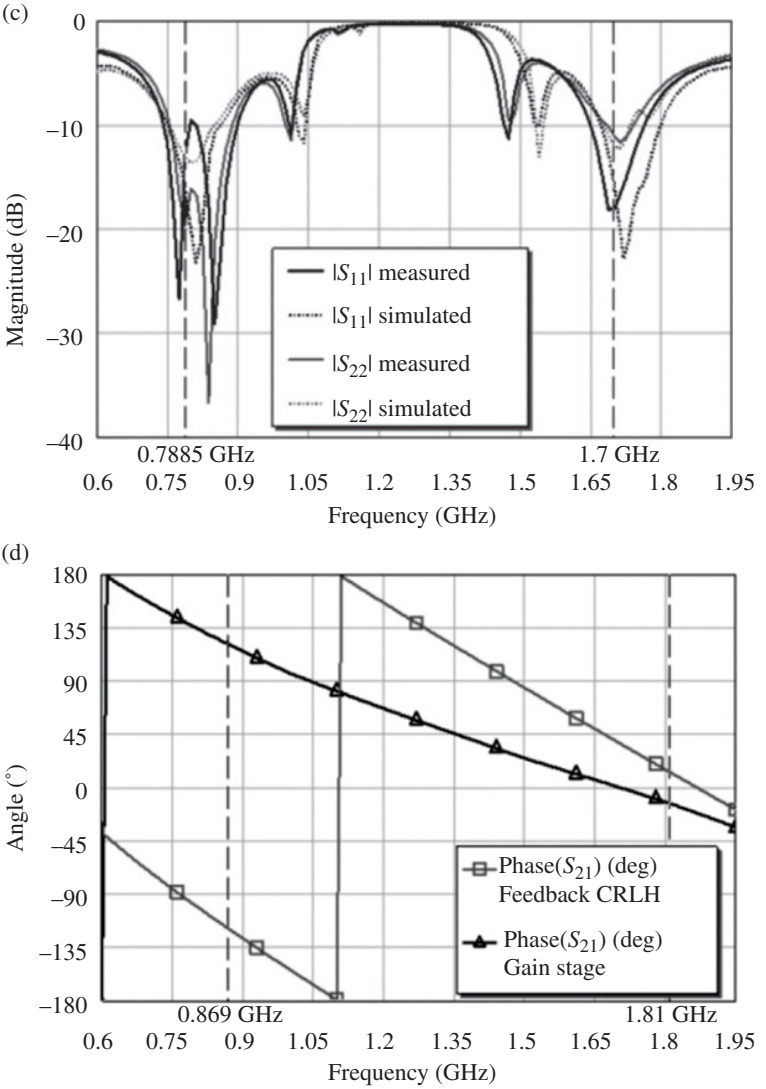

FIGURE 4.52 (*Continued*)

at the fundamental SRR resonance frequency (and at higher-order resonances). Thus, any variable able to modify the resonance frequency of the SRR can be easily sensed. Indeed, SRR-loaded lines can be used for sensing purposes, but these microwave sensors are considered to belong to the category of lines with metamaterial loading, and will be studied later in this chapter.

CRLH lines can be engineered in order to implement sensors with small size and high sensitivity (the author recommends the paper [148] and references therein to those readers willing to penetrate more deeply in the topic of CRLH transmission

line-based sensors—from now on CRLH-sensors to simplify the terminology). Typically, CRLH-sensors use capacitive elements as transducers. Hence, in combination with functional layers (e.g., for the monitoring of chemical or biological substances), with specific mechanical setups such as movable capacitor plates, or with tunable materials, such CRLH-sensors can be useful to measure very different variables. CRLH-sensors can be subdivided into two groups: spatially integrating sensors and spatially resolved sensors [148]. The first group refers to sensors where the output signal is determined by a change of the overall (average) transmission line properties caused by changes within the line capacitors as transducer elements. Spatially resolved CRLH sensors have the same structure, but each transducer element is read out individually, which leads to an output vector instead of a single measured value.

As an example of a spatially integrating CRLH-sensor, we report here a mass flow sensor first presented in Ref. [149], able to detect velocities in a conveyor belt system. The sensor consists of a 10-cell CRLH resonator coupled to the input ports by means of SMD capacitors. Actually, the CRLH line is composed of series (patch) capacitances and shunt inductances, as depicted in Figure 4.53. However, parasitics are unavoidable and therefore the line is actually a CRLH line. The sensor is fed by a microwave signal tuned to the desired resonance of the sensor, and, simultaneously, such signal is fed into a phase comparator. The time-dependent dielectric load of the sensor modulates the phase of the resonator output signal. This phase is compared with the reference phase originated directly from the source. The difference provides a measure of the dielectric loading of the resonator [149]. For velocity measurement of single particles passing on the measurement section, the time-dependent phase shift describes a sinusoidal wave. From the time difference between two adjacent phase minima, the velocity can be inferred.

Another interesting sensing device reported by the same authors is the CRLH transmission line-based differential sensor [150]. This sensor, depicted in Figure 4.54, utilizes two identical CRLH lines and two power dividers/combiners. The microwave signal is divided into two equal parts (by means of a Wilkinson power divider) and fed into the two CRLH lines. The feeding lines of the upper artificial line are one half wavelength longer than the ones of the lower line, so that the signals at the end of both lines exhibit a phase difference of 180°. One of these CRLH lines acts as the reference, whereas the other one is detuned by dielectric loading. The altered signal is subtracted (due to the presence of the combiner) from the unaltered reference to form the output signal. The resulting signal to noise ratio for this configuration has been found to be roughly 60 dB, allowing a high measurement dynamic range [150] (see Fig. 4.54b). In this sensor, the variable to be evaluated is simply the magnitude of S_{21} at the output port, rather than the phase. However, such magnitude is intimately related to the phase variation in the active line, caused by the presence of a dielectric load. Thus, the sensor principle is based on a power measurement, rather than on a phase measurement. Another advantage of this setup is that the sensitivity can be linearly increased with the number of used cells. These devices can be applied in medical diagnosis or as biosensors for the detection of specific substances.

Examples of spatially resolved sensors are reported in Ref. [148] and references therein. Among them, wireless temperature sensors with identification [151] and level

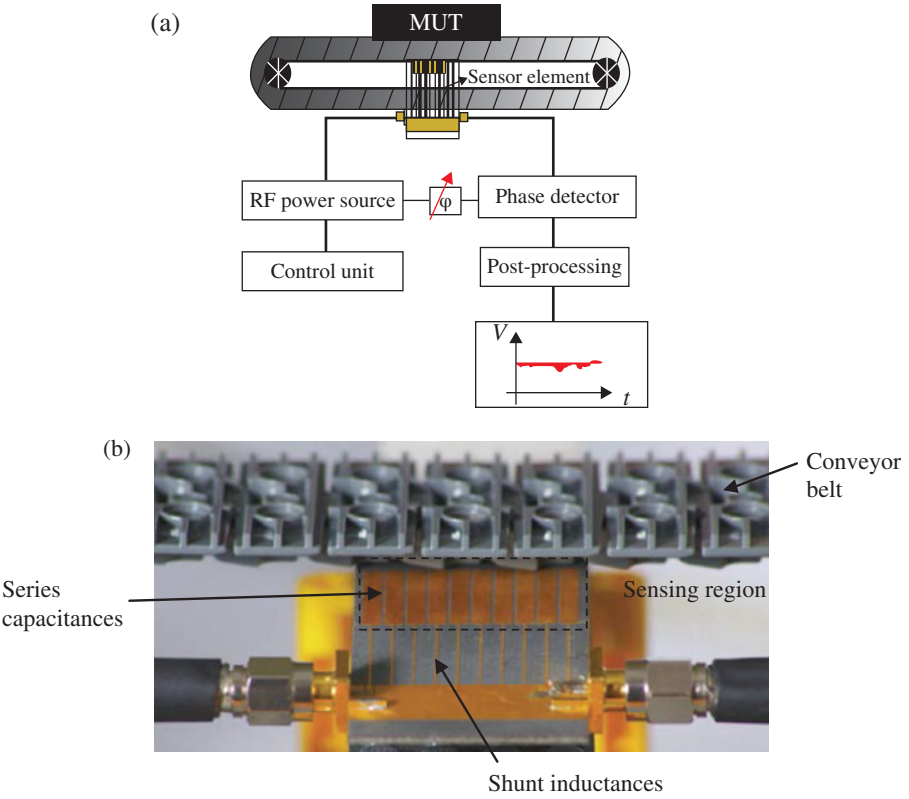

FIGURE 4.53 Bloch diagram of the mass flow sensor setup (a) and photograph of the sensor under the conveyor belt (b). Reprinted with permission from Ref. [147]; copyright 2012 IEEE.

sensors [152] constitute good examples of the potential of CRLH transmission lines for sensing purposes.

4.3 TRANSMISSION LINES WITH METAMATERIAL LOADING AND APPLICATIONS

By loading a transmission line with electrically small resonators, such as those formerly used for the implementation of metamaterials (SRRs, CSRRs) or other related resonators (see Section 3.3), multiband planar antennas, sensors, radiofrequency bar codes, and other RF/microwave devices can be implemented.[35] Let us review some of these applications in the next subsections.

[35] Indeed, planar notch and stopband filters consisting of transmission lines loaded with SRRs, CSRRs, and so on, could have been included in this section (notice that the design of these filters is not based on dispersion/impedance engineering). However, the author has opted for the inclusion of SRR-based notch and stopband filters in a single subsection devoted to filters (Section 4.2.3) for coherence. Nevertheless, tunable filters and other advanced filters will be studied in the next chapters.

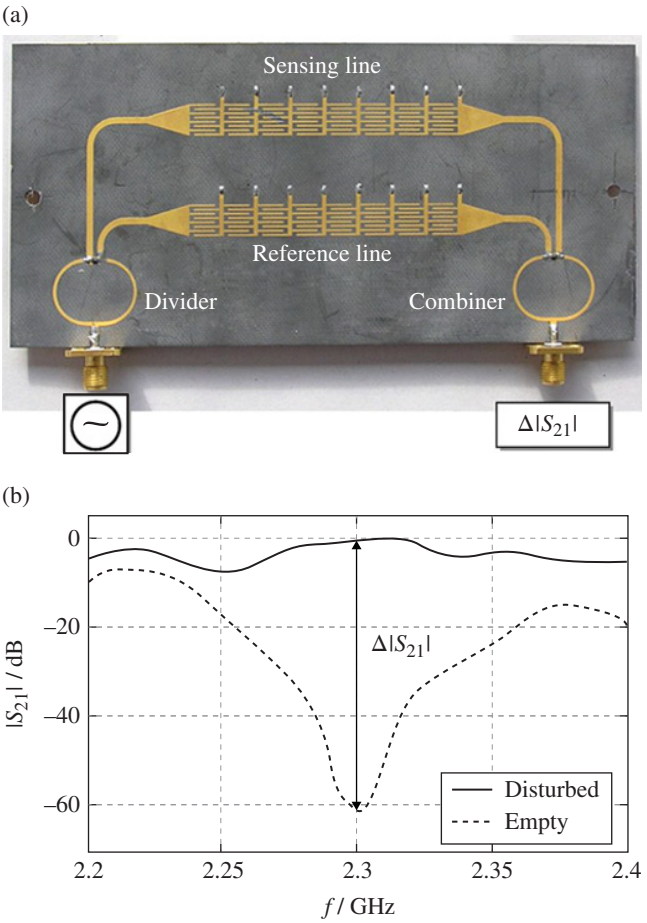

FIGURE 4.54 Photograph of the proposed CRLH transmission line-based differential sensor (a) and comparison between the transmission coefficients for the empty case (unloaded sensing line) and for a small dielectric disturbance applied to the sensing line (b). Reprinted with permission from Ref. [150]; copyright 2009 IEEE.

4.3.1 Multiband Planar Antennas

There are several approaches for the implementation of multiband antennas in planar technology. Here we report two strategies: one based on the concept of trap antennas and the other based on a perturbation method, of special interest in ultra-high-frequency radiofrequency identification (UHF-RFID) for the implementation of tags able to operate in two of the regulated UHF-RFID bands.

4.3.1.1 Multiband Printed Dipole and Monopole Antennas In this subsection, the focus is on printed dipole and monopole antennas with metamaterial loading

[153–157]. The idea of this technique is based on loading a conventional printed antenna with a set of resonant particles. In Ref. [154], it is shown that a dual-band antenna is achieved by coupling a set of SRRs to a printed dipole. Using this approach, the benefits of printed antennas are kept while dual-band antennas are achieved by using a simple design technique. The SRRs produce open circuits in their positions at the resonance frequencies. Hence the antenna resonance is achieved not only when the effective length of the dipole arms is $\lambda/4$ (λ being the guided wavelength), but also when the different locations of the SRR are $\lambda/4$ from the antenna feeding point (the SRRs must be tuned at these frequencies). By using SRRs, narrow bandwidths are reported in Ref. [154] for the bands associated with the SRR loading. An open circuit in the dipole arms can also be obtained by means of series connected OCSRRs. By using these particles, broadband responses can be achieved (as compared to SRRs), due to the relative values of capacitance and inductance in OCSRRs.

To illustrate the potential of OCSRR-loaded printed antennas, a dual-band dipole [156] and a tri-band monopole [157] are reported. The layout of the printed dipole (an antipodal structure) and the details of the OCSRR are depicted in Figure 4.55 (the photograph of the antenna, compared to the conventional mono-band dipole, is also shown in Fig. 4.55). The parameters of each dipole strip are the length L and the width W (which must be engineered to optimize matching). This antipodal configuration was chosen in Ref. [156] because it avoids the use of a balun to feed the antenna. The dimensions of the feeding line are the length L_f and the width W_f. An OCSRR is connected in series to each dipole strip at a distance d_{OCSRR} from the center of the antenna. The different dimensions of the proposed antenna were optimized to simultaneously operate at the L1-GPS frequency (1.575 GHz) and the WiFi band of 2.4–2.48 GHz, namely, $L = 22.00$ mm, $W = 2.5$ mm, $L_f = 25$ mm, $W_f = 1.15$ mm, $d_{OCSRR} = 17$ mm, $l_{ext} = 4$ mm, and $c = d = 0.3$ mm. The used substrate is the *Rogers RO3010* with $\varepsilon_r = 10.2$ and $h = 1.27$ mm.

In the case of the conventional unloaded antenna, there is only one series resonance at 2.1 GHz. This resonance corresponds to the fundamental mode of the dipole antenna. In the vicinity of resonance, the value of the real part of the antenna impedance is close to 50 Ω (not shown), which produces proper matching, as it can be appreciated in Figure 4.56. OCSRR loading introduces a parallel resonance in the proposed dual-band antenna input impedance. The addition of this parallel resonance has a double effect on the input impedance of the proposed dual-band antenna. The first one is a slight shift of the series resonance of the dipole antenna toward higher frequencies. In this case, this resonance is found at 2.45 GHz. The second effect is the appearance of an additional series resonance below the parallel resonance of the OCSRRs. This additional series resonance is found at 1.6 GHz. The real part of the input impedance is around 50 Ω in the vicinity of this additional series resonance. This allows achieving an additional band with proper matching in the proposed antenna (Fig. 4.56). As it can be seen, this additional frequency is below the fundamental frequency of the unloaded dipole antenna.

Considering $|S_{11}|$ below −10 dB, the first working band is centered at 1.56 GHz with 5% bandwidth and the second one is centered at 2.46 GHz with 9% bandwidth. These bandwidths represent a considerable improvement with respect to the

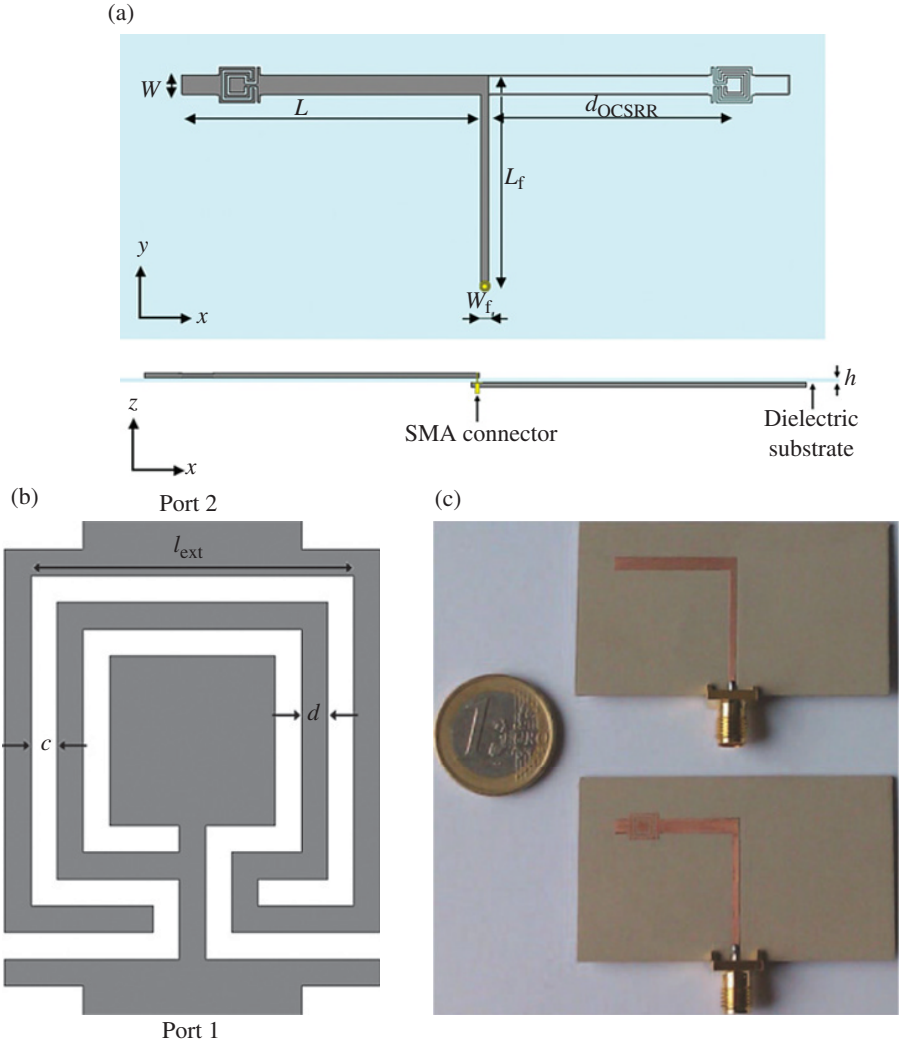

FIGURE 4.55 Antipodal dipole antenna loaded with OCSRRs. (a) Top and cross-sectional views; (b) detail of the OCSRR and relevant dimensions; and (c) comparative photographs of the unloaded (top) and loaded (bottom) printed dipole antenna. Reprinted with permission from Ref. [156]; copyright 2012 John Wiley.

implementations based on SRRs [154, 155]. The measured gain of the antenna (estimated in a TEM cell from the power received by the antenna and the incident field measured by a probe) is 0.85 dB at the GPS band (1.575 GHz) and 2 dB at the WiFi band (2.45 GHz). The radiation patterns inferred with *CST Microwave Studio* for the proposed dual-band antenna are shown in Figure 4.57. A dipolar-like radiation pattern is obtained at both working bands. The typical figure of eight is obtained

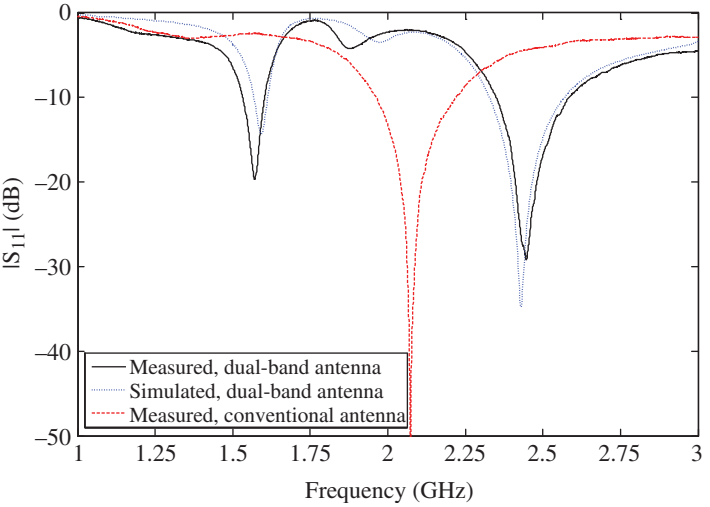

FIGURE 4.56 Measured and simulated reflection coefficient of dual-band printed dipole antenna compared to the unloaded antenna. Reprinted with permission from Ref. [156]; copyright 2012 John Wiley.

in the *xz*-plane and an omnidirectional pattern is obtained in the *yz*-plane at both frequencies (1.575 and 2.45 GHz). The only difference between both working bands is the cross-polarization level, which is around −10 dB in the first band while it is −20 dB in the second one.

OCSRR loading can also be applied to printed monopole antennas [157]. Figure 4.58 shows a photograph of two fabricated prototypes: a dual-band and a tri-band printed monopole antenna. The considered substrate in this case was the low-cost *FR4* ($\varepsilon_r = 4.5$ and $h = 1.5$ mm). The dual-band antenna covers the bands of 2.40–2.48 GHz (Bluetooth and WiFi) and 5.15–5.80 GHz (WiFi). The dimensions of the monopole are $L_m = 21$ mm and $W_m = 5.85$ mm. The parameters of the feeding line were set to obtain a 50 Ω CPW. Hence, $S = 2.44$ mm and $W = 0.30$ mm. The dimensions of each ground plane are $L_g = 16$ mm and $W_g = 13.48$ mm. The gap between the ground planes and the monopole is $g = 0.30$ mm. The OCSRR was placed at a distance $d_o = 12.50$ mm and its parameters are $l_{ext} = 2.30$ mm, $c = d = 0.25$ mm. The gap g_o was set to 0.50 mm.

The tri-band monopole antenna is an extension of the previous dual-band antenna, and it covers the previous bands and the IEEE 802.11y band of 3.65–3.70 GHz. According to the layout of the tri-band monopole (Fig. 4.58), the additional OCSRR was placed at a distance $d_{o2} = 18$ mm. Its dimensions are $l_{ext} = 2.70$ mm and $c = d =$ 0.25 mm. This corresponds to a resonance frequency of 3.65 GHz. The gap g_{o2} was set to 0.40 mm. These values were optimized to only cover the desired bandwidth and not interfere with other systems. The other parameters of the antenna remain unchanged with respect to the dual-band design, except the length of the monopole which is

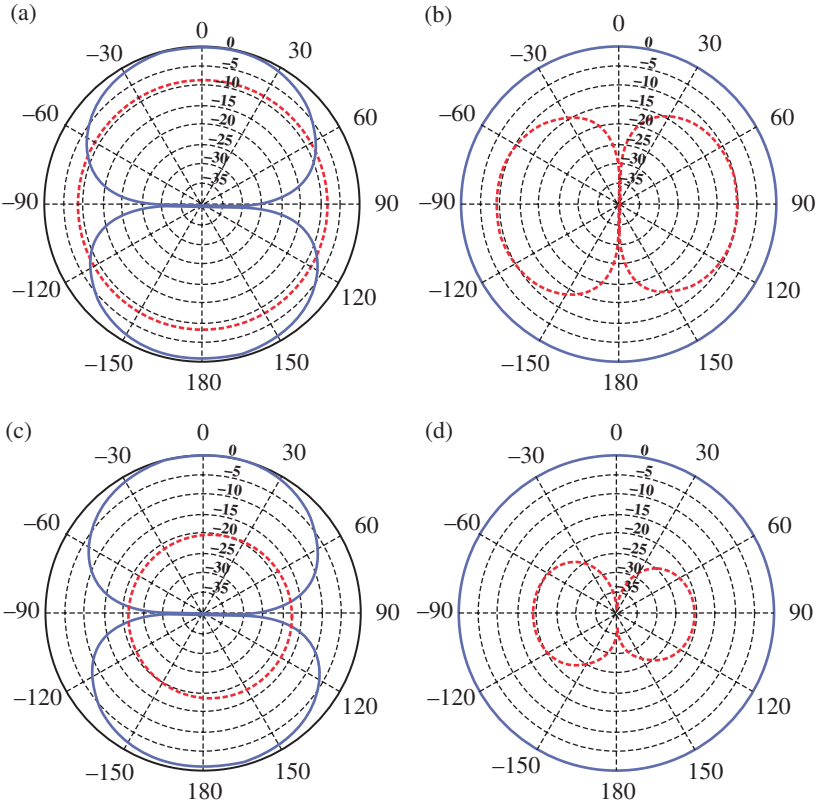

FIGURE 4.57 Simulated normalized radiation patterns for the proposed dual-band dipole antenna. Solid line: copolar component and dashed line: crosspolar component. (a) 1.575 GHz, *xz*-plane; (b) 1.575 GHz, *yz*-plane; (c) 2.45 GHz, *xz*-plane; and (d) 2.45 GHz, *yz*-plane. Reprinted with permission from Ref. [156]; copyright 2012 John Wiley.

reduced to $L_m = 19.75$ mm to compensate the inductive behavior of the OCSRRs below their resonance frequencies.

The simulated and measured reflection coefficients of the dual-band and tri-band monopoles are depicted in Figure 4.59. The dual-band printed monopole antenna exhibits good matching ($|S_{11}| < -10$ dB) from 2.29 GHz to 2.52 GHz at the lower frequency band. This corresponds to a 9.6% bandwidth. In the upper band, the antenna is well matched from 4.66 GHz to at least 7 GHz. Thus, the fabricated antenna satisfies the specifications of Bluetooth and WiFi (bands of 2.40–2.48 GHz and 5.15–5.80 GHz). The fabricated tri-band monopole antenna is well matched from 2.30 GHz to 2.52 GHz for the first band. Its reflection coefficient is below −10 dB between 3.56 GHz and 3.78 GHz for the second band, and between 5.06 GHz and 6.71 GHz for the third band. Hence, the fabricated prototype is well matched within the regulated bandwidths of Bluetooth and WiFi including IEEE 802.11y (3.65–3.70 GHz band).

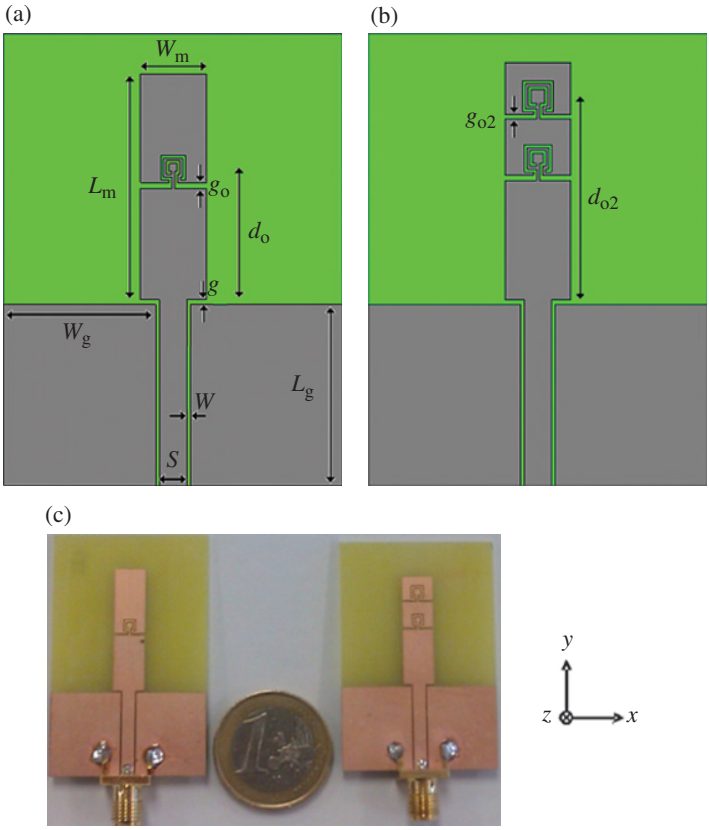

FIGURE 4.58 Sketch of the dual-band (a), and tri-band (b) printed monopole antenna loaded with OCSRRs, and respective photographs (c). Reprinted with permission from Ref. [157]; copyright 2011 IEEE.

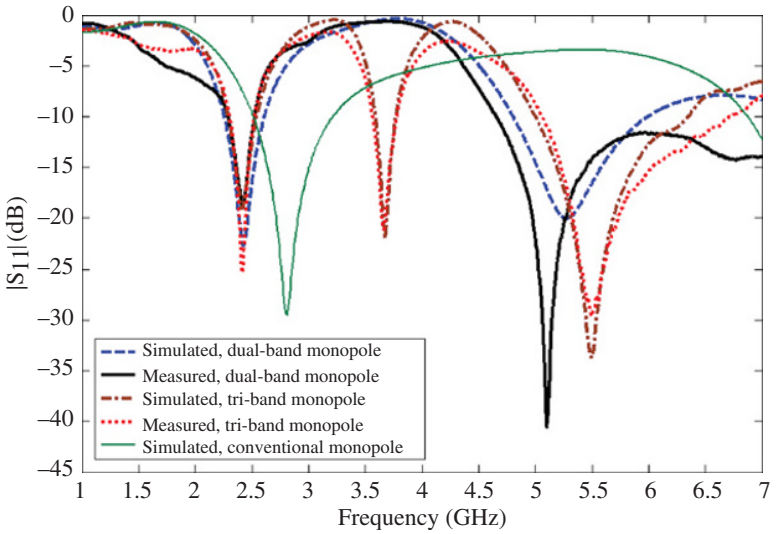

FIGURE 4.59 Simulated and measured reflection coefficient of the dual-band and tri-band printed monopole antennas. The simulated reflection coefficient of the conventional monopole antenna is also plotted. Reprinted with permission from Ref. [157]; copyright 2011 IEEE.

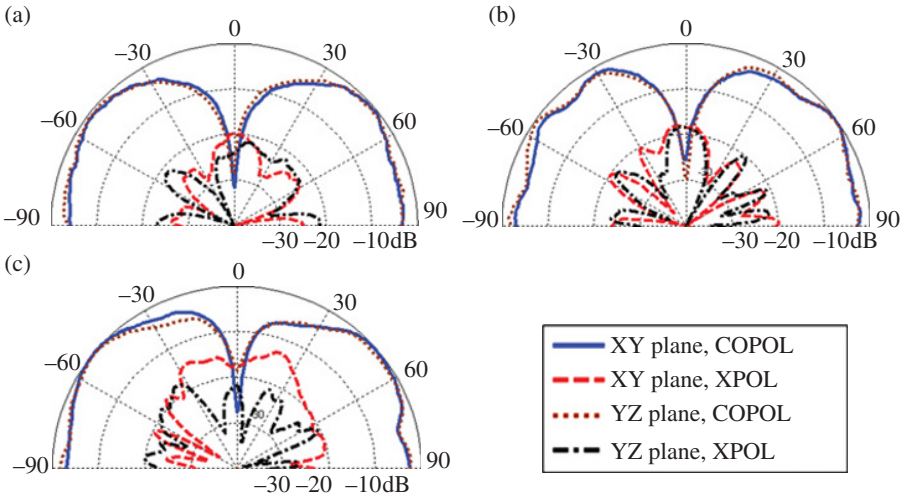

FIGURE 4.60 Measured radiation patterns of the tri-band printed monopole antenna. (a) 2.45 GHz, (b) 3.65 GHz, and (c) 5.40 GHz. Reprinted with permission from Ref. [157]; copyright 2011 IEEE.

The proposed antennas present monopolar radiation characteristics at all the bands. As an example, the normalized measured radiation patterns of the tri-band monopole antenna are shown in Figure 4.60. A monopolar radiation pattern is obtained at the three frequencies. The crosspolar component (XPOL) has low values (below −20 dB in all cases, except the *xy*-plane of the third frequency where is below −15 dB). The gains of this design are 1.4 dB, 1.2 dB, and 1.7 dB at the first, second, and third bands, respectively. These results are in good agreement with simulations, in which the radiation efficiency is 92%, 83%, and 94% and the overall efficiency is 91%, 82%, and 93% at the central frequency of each band.

4.3.1.2 Dual-Band UHF-RFID Tags Metamaterial loading is also interesting for the implementation of dual-band antennas with close frequency bands. This is the case of UHF-RFID, where the different regulated bands worldwide are contained in the spectral region comprised between 860 MHz and 960 MHz. Our aim in this subsection is to demonstrate that by loading tag antennas with electrically small resonators, it is possible to implement UHF-RFID tags operative at two of the regulated UHF-RFID bands. The dual-band functionality is achieved by applying a perturbation method similar to that reported in Ref. [158] for dual-band matching networks, properly adapted.

The key aspect in the implementation of long read-range UHF-RFID chip-based tags is to achieve conjugate matching between the antenna and the integrated circuit (or chip). The input impedance of the chip is provided by the manufacturer and varies with frequency. Therefore, the implementation of dual-band UHF-RFID tags means

to design the antenna (and the matching network, if it is present) so that the chip "sees" its conjugate impedance at the required frequencies. This can be done by cascading a dual-band impedance matching network between the antenna and the chip, consisting of a transmission line loaded with a metamaterial resonator [158]. The resonator produces a perturbation in both the characteristic impedance and the phase constant of the transmission line, and conjugate matching at two frequencies can be obtained (the details are given in Ref. [158]). However, it is possible to directly actuate on the impedance of the antenna, by loading it with metamaterial resonant particles [159] (avoiding thus the matching circuitry). The principle is very similar to that reported in Ref. [158] for matching networks.

Following the earlier cited perturbation approach, several dual-band UHF-RFID tag antennas have been implemented. One prototype device consists of a meander line antenna (MLA) loaded with a spiral resonator (SR) [159]. The layout of the antenna, compared to the one without the SR is depicted in Figure 4.61. The dual-band antenna was designed to be operative at the European (867 MHz) and USA (915 MHz) UHF-RFID regulated bands. The antenna was designed on the *Rogers RO3010* with dielectric constant $\varepsilon_r = 10.2$ and thickness $h = 0.127$ mm. The considered RFID chip was the *SL31001* from *NXP Semiconductors*.

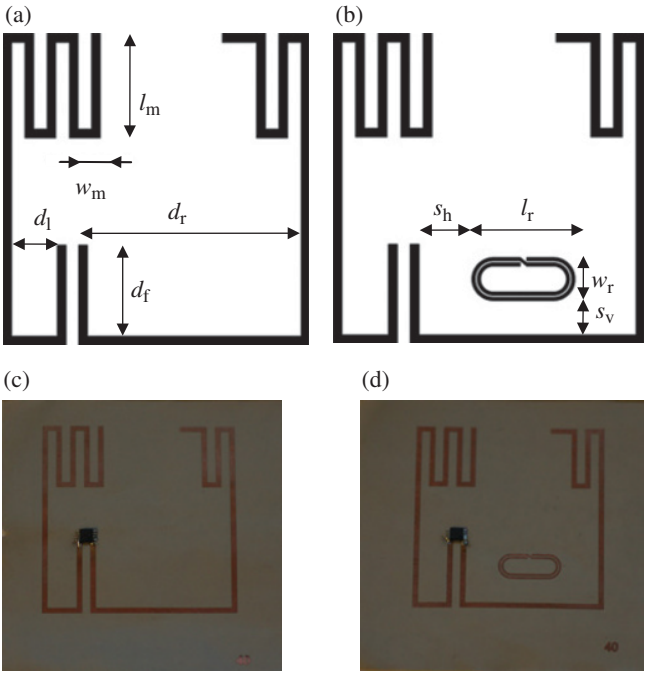

FIGURE 4.61 Layout of the unloaded (a) and SR-loaded (b) MLA, and relevant dimensions. The photographs of the fabricated prototypes are depicted in (c) and (d). The strip width of the SR is 0.5 mm, and the separation between strips is 0.3 mm. Reprinted with permission from Ref. [159]; copyright 2011 IEEE.

The impedance of the chip at the intermediate frequency (between 867 MHz and 915 MHz) is $Z_{chip} = 20 - j485\ \Omega$. This impedance was considered as reference impedance, so that the antenna was designed to roughly exhibit the conjugate impedance of the chip at the intermediate frequency (891 MHz), and then the perturbation (by means of the SR) was introduced in order to achieve conjugate matching at the required frequencies. The dimensions of the MLA are 48 mm × 48 mm, and the strip width is 1.4 mm. The other relevant dimensions (in reference to Fig. 4.61) are $l_m = 16.3$ mm, $w_m = 4.8$ mm, $d_l = 7.3$ mm, $d_r = 33.9$ mm, $d_f = 14.2$ mm, $l_r = 16.1$ mm, $w_r = 6.8$ mm, $s_h = 8.3$ mm, and $s_v = 5.4$ mm. The input impedance and matching of the dual-band SR-loaded MLA are depicted in Figure 4.62, where it can be appreciated that the dual-band functionality is achieved.

Both antennas were fabricated, and the read range, given by

$$r = \frac{\lambda}{4\pi}\sqrt{\frac{\text{EIRP}\, G_r \tau}{P_{chip}}} \tag{4.65}$$

was measured through the experimental setup sketched in Figure 4.63. In (4.65), λ is the wavelength, *EIRP* (equivalent isotropic radiated power), determined by local

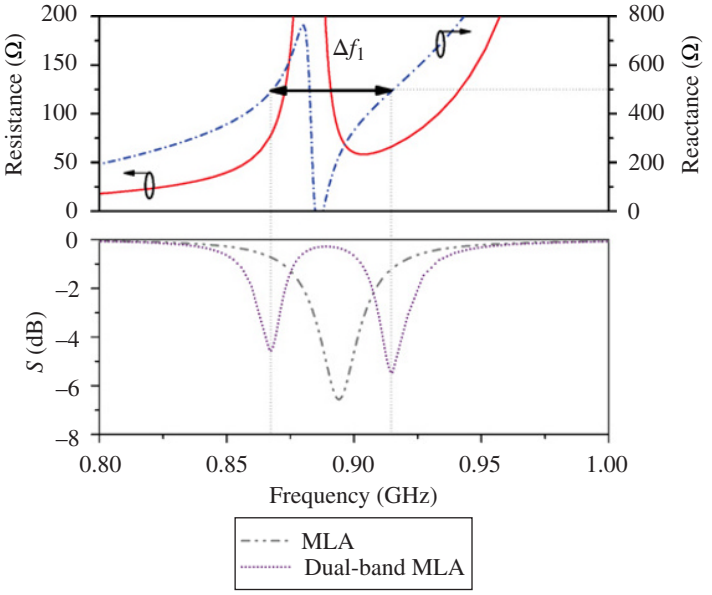

FIGURE 4.62 Input impedance of the dual-band MLA with coupled SR and power-wave reflection coefficient of the mono-band and dual-band meander line antenna. The frequencies where reactance matching is obtained, separated by Δf_1, are indicated and correspond to the resonance frequencies of the dual-band MLA. Reprinted with permission from Ref. [159]; copyright 2011 IEEE.

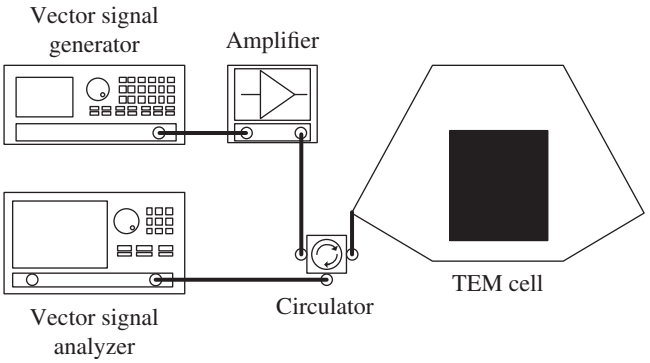

FIGURE 4.63 Bloch diagram of the experimental setup for UHF-RFID tag characterization.

country regulations, is the product of $P_t G_t$ which are the transmission power and the transmission gain, respectively, P_{chip} is the minimum threshold power necessary to activate the RFID chip, G_r is the gain of the receiving tag antenna, and τ is the power transmission coefficient. The value of *EIRP* in Europe is 3.3 W, whereas in the United States it is 4 W. The power transmission coefficient was inferred from the simulation of the return loss of the antenna, using as port impedance that of the chip. The tag gain was also obtained from simulation. Using (4.65), the theoretical read range was calculated.

The experimental setup for read-range measurement consists of a *N5182A* vector signal generator which creates RFID frames. Such generator was connected to a TEM cell by means of a circulator. The tag under test was located inside the TEM cell, and it was excited by the frame created by the generator, generating a backscatter signal to a *N9020A* signal analyzer through the circulator. The RFID frame frequency was swept with a specific power. Once the operation frequencies were identified, the output power was decreased until the tag stopped working. Finally, a probe was placed into the TEM cell in order to determine the incident electric field intensity E_0 at each frequency, which is related to the received power by the chip according to

$$P_{chip} = SA_{ef}\tau = \frac{|E_0|^2}{2\eta}\frac{\lambda^2 G_r}{4\pi}\tau \tag{4.66}$$

where S is the incident power density, A_{ef} is the effective area of the tag antenna, and η is the free-space wave impedance ($120\pi\ \Omega$). The measured read range can be inferred by introducing (4.66) in (4.65), resulting

$$r = \frac{\sqrt{60\ \text{EIRP}}}{E_0} \tag{4.67}$$

As indicated before, the *EIRP* in Europe is lower than the *EIRP* in the United States, so the read range in Europe is expected to be reduced for the same incident

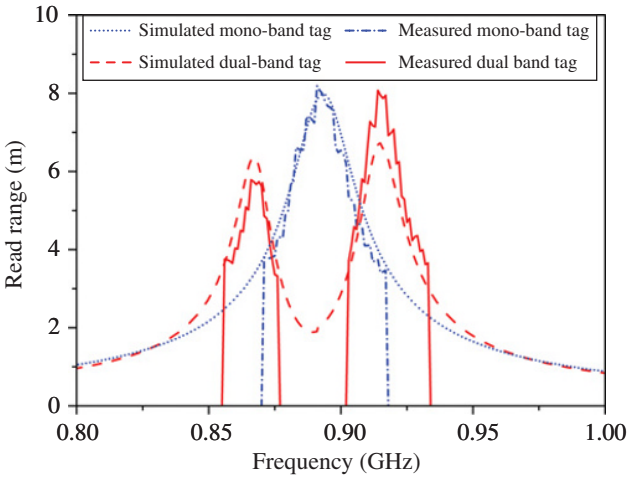

FIGURE 4.64 Simulated and measured read ranges of the mono-band and dual-band MLA RFID tags. Reprinted with permission from Ref. [159]; copyright 2011 IEEE.

electric field intensity. The simulated and measured read ranges of both tags are depicted in Figure 4.64. The read range obtained in the dual-band tag (at the frequencies of interest) is superior to that of the mono-band tag. The read range of the single-band MLA tag is roughly 4 m at the frequencies of interest, whereas almost 6 m and 8 m at the European and USA frequency bands, respectively, are achieved by means of the designed dual-band MLA.

The perturbation method based on loading the antenna with SRs can also be applied to other planar antennas, such as folded dipole antennas [160], for the implementation of dual-band UHF-RFID tags. It was also shown in Ref. [160] that detuning caused by the object or material to which the tag is attached can be corrected by tailoring the distance between the antenna and the SR (see Ref. [160] for more details).

4.3.2 Transmission Lines Loaded with Symmetric Resonators and Applications

Along this chapter, several microwave devices based on transmission lines loaded with symmetric resonators (SRRs, CSRRs, etc.) have been studied. However, the symmetry properties of transmission lines loaded with symmetric resonators have not been analyzed so far. Such symmetry properties are very interesting and can be exploited for the implementation of microwave sensors and RF bar codes. In both cases, the working principle is the truncation of symmetry. In the next subsection, this working principle is analyzed in detail, whereas the applications are left for the following subsections.

4.3.2.1 Symmetry Properties: Working Principle for Sensors and RF Bar Codes Let us consider a transmission line, such as a CPW, loaded with a single SRR, rather than with a pair of SRRs. In absence of loading elements, the symmetry plane of the line is a magnetic wall for the fundamental CPW mode. Let us now consider that the symmetry plane of the SRR, etched in the back substrate side of the CPW, is aligned with the symmetry plane of the line. Under these conditions, there is not a net axial magnetic field able to inductively drive the particle, and the SRR is not excited, that is, the line is transparent (see Fig. 4.65). However, if symmetry is truncated, for instance by laterally displacing or rotating the SRR, or by any other means causing asymmetry (i.e., dielectric loading), the resonator is excited, causing a notch in the transmission coefficient. The magnitude of this notch increases with the level of asymmetry. Therefore, the notch magnitude can provide a measure of the variable responsible for symmetry truncation (displacement, rotation angle, etc.) [161, 162]. Indeed, with perfectly aligned CPW and SRR symmetry planes, the resonator is not excited because such symmetry planes are of distinct EM nature (the symmetry plane of the SRR is an electric wall at the fundamental resonance). However, a slight misalignment between these symmetry planes suffices to drive the particle, causing a notch in the transmission coefficient. According to these words, any planar resonator exhibiting an electric wall at resonance can potentially be useful as sensing element loading a transmission line excited with an even mode (necessary to generate a magnetic wall in the symmetry plane of the line).

Symmetric resonators exhibiting a magnetic wall at resonance, such as the CSRR, can also be used for sensing purposes. However, in this case the host line must be chosen to exhibit an electric wall, rather than a magnetic wall, at its symmetry plane. Under these conditions, the symmetry planes of the line and resonator are also of

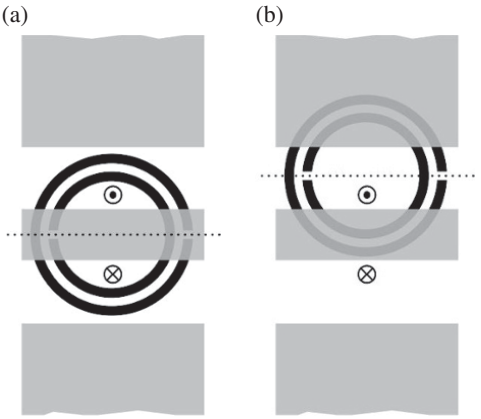

FIGURE 4.65 CPW loaded with an aligned (a) and misaligned (b) SRR. Due to symmetry, there is not a net axial magnetic field in (a) able to excite the SRR, contrary to the situation depicted in (b).

different EM nature, and the loaded line is transparent if such planes are perfectly aligned. For instance, a differential microstrip line loaded with a CSRR (etched in the ground plane) in a symmetric configuration is transparent for the differential mode.[36] However, the CSRR causes a strong notch for the common mode because for this mode the symmetry planes (line and CSRR) are both a magnetic wall (common-mode filters based on CSRRs will be discussed in the Section devoted to differential lines in the last chapter [163]). Obviously, the CSRR acts as a notch filter for the differential mode as well if symmetry is truncated.

Symmetric resonators can also be used for the implementation of RF bar codes, also known as spectral signatures codes [164].[37] In RF bar codes, a transmission line is loaded with multiple resonators, each tuned at a different frequency. Each resonance frequency corresponds to a different bit, and the logic '1' and '0' states are given by the presence or absence, respectively, of a transmission zero in the spectrum for that frequency. For the implementation of RF bar codes, symmetric resonators are not a due. Indeed, in Ref. [165] SRs are used as loading elements of a microstrip line based 35-bit bar code. Encoding can be achieved by etching (close to the microstrip line) only those SRs with resonance frequency corresponding to the required logic '1' states. The coupling between the line and the spiral inhibits transmission at the resonance frequency, with the result of as many notches as spirals. An alternative for line encoding is to etch the whole set of spirals close to the line and short-circuit those spirals with resonance frequency corresponding to the required "0" states. By short-circuiting the spiral, the corresponding resonance frequency is moved away, providing the same effect as removing the spiral.

By using symmetric resonators as loading elements in RF bar codes, writing the '1' state is as simple as truncating symmetry, for instance by rotating or laterally displacing the resonant element [164]. This opens the possibility to implement mechanically reconfigurable bar codes, or bar codes where encoding can be achieved by any other means of truncating symmetry. Moreover, since the level of asymmetry determines the notch magnitude, it is potentially possible to increase the stored information by simply providing more than two logic states to each resonant element.

4.3.2.2 Rotation, Displacement, and Alignment Sensors Most microwave sensors that make use of resonators as sensing elements are based on the variation of the resonance frequency, phase, or quality factor caused by the physical magnitude under measurement. Split rings, including SRRs, CSRRs or other related resonators, have been widely used as sensors [161, 162, 166–176]. Among them, there are several

[36] This configuration is roughly the dual of the CPW loaded with an SRR, and hence a similar behavior is expected.

[37] RF bar codes are chipless RFID tags, where the information can be stored in a set of resonant elements causing a specific spectral response. Typically, such resonant elements are coupled to a host transmission line, which is equipped with cross-polarized receiver and transmitter antennas for wireless identification. As compared to other chipless RFID tags based on time domain reflectometry (TDR) [164], RF bar codes need a relatively large bandwidth for high data capacity, since each resonant element is tuned at a different frequency and contributes with a single bit to the whole code.

implementations where a host line is loaded with such metamaterial resonators. For instance, sensors able to spatially resolve the dielectric properties of a material were achieved in Ref. [172] by loading a line with an array of SRRs tuned at different frequencies. In such sensors, a frequency shift of one individual resonant peak indicates the dielectric properties of the material under test and its location within the array. Two-dimensional displacement sensors consisting of a bended microstrip line loaded with a pair of triangular and orthogonally oriented CSRRs (etched on the ground plane of an independent and movable substrate) were also proposed [173]. The working principle is based on detuning the CSRR by a change in the line-to-CSRR coupling capacitance. The triangular shape of the CSRR was considered in order to enhance the sensitivity of the sensor. Moreover, two orthogonally polarized receiving and transmitting antennas were cascaded to the input and output ports of the host line in order to provide a wireless connection to the reader. The scheme of the wireless link and the photograph of the designed displacement sensor are depicted in Figure 4.66a and b, respectively. Figure 4.66c shows the variation of the frequency response that is obtained by laterally displacing one of the rings with regard to the line axis.

Alternatively to the frequency shift caused by the variable under measurement, symmetry truncation can be used for sensing and detection purposes in transmission lines loaded with symmetric resonant particles. One advantage of this strategy is a major robustness in front of changing ambient conditions. Such environmental variations may cause frequency detuning, but have little effect on the notch magnitude. Moreover, notice that sensors based on symmetry properties can be used as detectors, able to "detect" the lack of symmetry. For instance, SRR-loaded CPWs can be used as alignment sensors, where the lack of alignment between two surfaces is detected by the presence of a notch in the transmission spectrum. Under perfect alignment, such notch is not present, regardless of the environmental conditions. The first sensors based on the symmetry properties of SRR loaded lines were reported in Ref. [161]. Both one-dimensional displacement and rotation sensors based on rectangular-shaped SRRs and CPWs were reported. The rectangular shape of the SRRs was chosen in order to optimize the sensitivity. Namely, if circularly shaped SRR with an internal diameter much larger than the distance between the CPW slots is considered, the magnetic field lines within the SRR region do not exactly cancel if symmetry is broken, but the effects of asymmetry are not significant. Conversely, if the SRR does not extend beyond the slots of the CPW, the effects of the asymmetry on the frequency response of the structure (notch magnitude) are more pronounced. Indeed, it was found that the magnitude of the notch increases by etching the SRR just below the central strip of the CPW [161]. Another important parameter regarding sensitivity is the vertical distance between the CPW metallic layer and the resonator. Sensitivity increases by reducing such distance because the coupling between the line and the resonator also increases. Thus, by using rectangular SRRs, it was found in Ref. [161] that high sensitive sensors with good linearity and dynamic range can be implemented for both linear displacement and rotation.

In Ref. [174], a proof of concept of a two-dimensional displacement sensor was proposed by combining the symmetry properties of the one-dimensional displacement

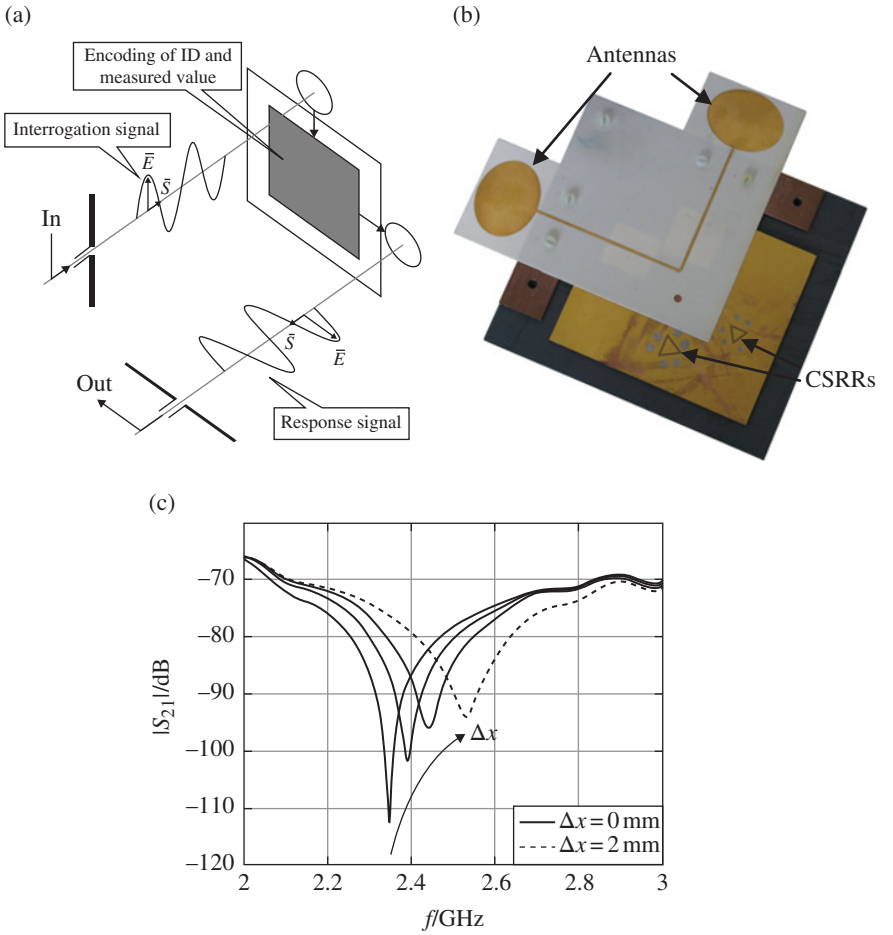

FIGURE 4.66 Two-dimensional wireless displacement sensor based on detuning of triangular shaped CSRRs. (a) Scheme showing the polarization decoupling of interrogation and response signals, (b) photograph, and (c) frequency response for various displacements. For better visualization in (b), the movable sensitive plate was rotated 180°. Reprinted with permission from Ref. [173]; copyright 2011 EuMA.

sensor of Ref. [161], and the bending scheme proposed in Ref. [173].[38] Like in Ref. [173], a right-angle bended CPW loaded with a pair of rectangular-shaped SRRs tuned at different frequencies and orthogonally oriented was proposed in Ref. [174]. The structure with the SRRs aligned with the line axis is depicted in Figure 4.67. This structure is able to detect lack of alignment and linear displacement in two

[38] In this proof of concept, rather than etching the SRRs in a movable substrate, these resonators were etched in the back substrate side, and different samples with different displacements were considered for characterization.

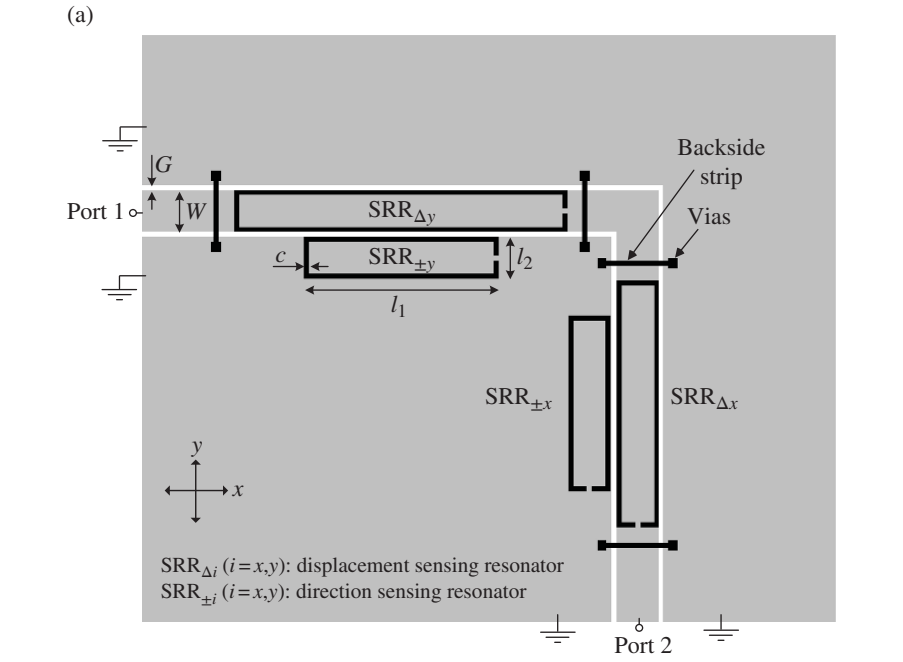

FIGURE 4.67 Layout (a) and top (b) and bottom (c) photographs of the two-dimensional displacement sensing device for the aligned position (i.e., the CPW and the displacement sensing SRRs are aligned). The CPW strip and slot widths are $W = 1.67$ mm and $G = 0.2$ mm, respectively; the vias have a 0.2 mm radius; and the narrow strips between vias have a width of 0.2 mm. The dimensions of the SRRs are $l_1(\text{SRR}_{\Delta x}) = 9.95$ mm, $l_1(\text{SRR}_{\pm x}) = 7.05$ mm, $l_1(\text{SRR}_{\Delta y}) = 13.4$ mm, $l_1(\text{SRR}_{\pm y}) = 7.8$ mm, $l_2 = 1.67$ mm, and $c = 0.2$ mm. The vias and backside strip metals are used to connect the CPW ground plane regions, and thus prevent the appearance of the parasitic slot mode. The considered substrate is the *Rogers RO3010* with dielectric constant $\varepsilon_r = 10.2$, thickness $h = 127$ μm, and loss tangent $\tan\delta = 0.0023$. Reprinted with permission from Ref. [174]; copyright 2012 MDPI.

dimensions. In order to distinguish the displacement direction, two additional resonators (also tuned at different frequencies) are used. One of these resonators is etched in the x-oriented CPW section and the other one in the y-oriented section, and both are situated beneath one of the CPW ground planes, near a CPW slot. If the displacement direction drives such additional resonators toward the slot of the CPW, this will be detected by a notch at the resonance frequency of these resonators. Conversely, by shifting the SRRs in the opposite direction such notch will not appear. Since it is necessary that the four required SRRs are tuned at different frequencies, the resonator dimensions must be different. Notice that these two additional resonators are introduced to simply detect the displacement direction (they do not provide information on the displacement magnitude). Therefore, these SRRs can be designated as direction sensing resonators, to differentiate them from the displacement sensing resonators, that is, those which measure the linear displacement magnitude.

For a better comprehension of the principle of operation of the proposed sensor, let us consider the four different displacements indicated in Figure 4.68, that is, right, left, up, and down displacements. The resonance frequencies of the four SRRs are denoted as $f_{\Delta y}, f_{\Delta x}, f_{\pm y}$, and $f_{\pm x}$ (see Fig. 4.68). It can be seen that displacement in the $\pm x$- and $\pm y$-direction can be detected (by means of the resonators $\mathrm{SRR}_{\pm x}$ and $\mathrm{SRR}_{\pm y}$) and measured (by the resonators $\mathrm{SRR}_{\Delta x}$ and $\mathrm{SRR}_{\Delta y}$). Any other linear displacement is a combination of the previous ones, and hence it can also be detected and measured. In order to validate the proposed approach, positive and negative displacement in the $x = y$ direction (diagonal shift) was considered. Figure 4.69 depicts the dependence of the notch magnitude (simulated and measured) with displacement. As expected, for positive displacements, the $\mathrm{SRR}_{\pm x}$ and $\mathrm{SRR}_{\pm y}$ are activated as it is manifested by a clear increase in the notch at $f_{\pm x}$ and $f_{\pm y}$, whereas the specified -3 dB threshold level is not exceeded for negative displacements (indicating that the shift is in the negative direction). The dependence of the notch magnitude for $f_{\Delta x}$ is similar and roughly linear in both directions, with a measured value of approximately -20 dB for $\Delta x = \pm 0.3$ mm, which is indicative of a significant sensitivity of roughly 65 dB/mm (average value). The same occurs for the dependence of the notch magnitude for $f_{\Delta y}$. However, the notch magnitude associated to a displacement sensing resonator depends not only on the displacement, but also on resonator dimensions. This causes that, for the same displacement, the notch magnitude of the y-axis displacement sensing resonator produces a deeper notch than that of the x-axis.

Rotation sensors with enhanced dynamic range and linearity (as compared to those reported in Ref. [161]) can be implemented by coupling circular resonators to a non-uniform (circularly shaped) CPW. Specifically, a circular ELC resonator was proposed as sensing element in Ref. [175] (see Fig. 4.70). As it was pointed out in Section 3.3.1.6, the ELC is a bisymmetric resonator with two orthogonal symmetry planes, one being a magnetic wall and the other one an electric wall at the fundamental resonance. If the electric wall is perfectly aligned with the symmetry plane of the line (a magnetic wall), the line is transparent. However, by rotating the particle 90°, the two magnetic walls (the one of the line and the

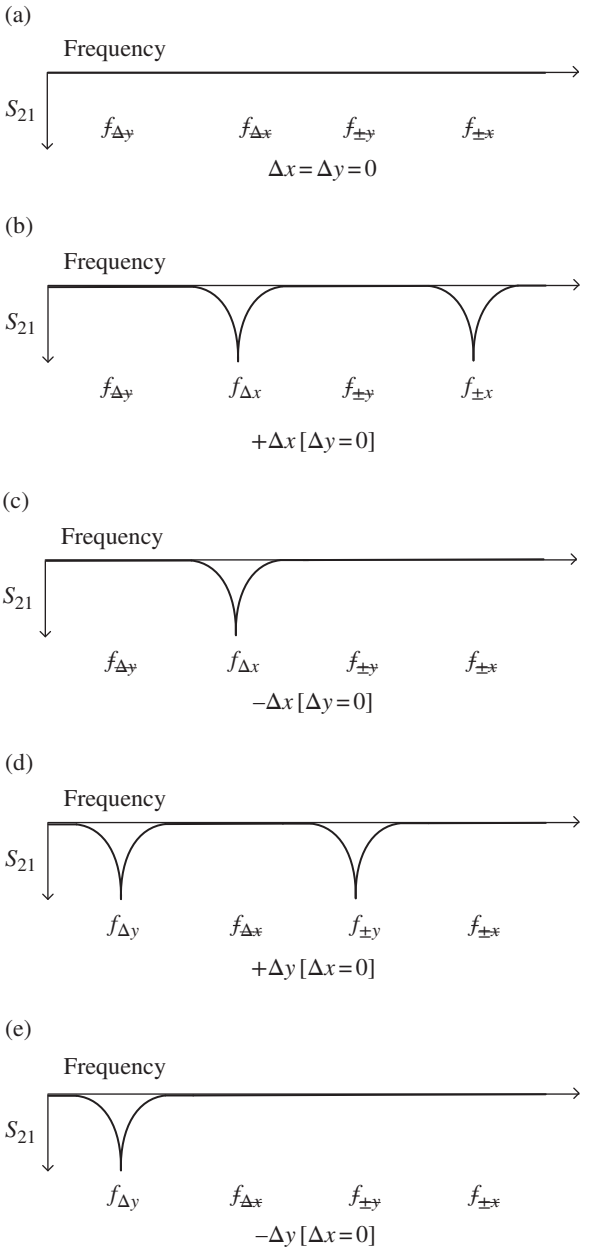

FIGURE 4.68 Scheme indicating the primitive shifting operations (a–e) and the resulting transmission coefficient S_{21}. A notch is indicative of an SRR excitation. A linear displacement in the x- and y-orientation is indicated as Δx and Δy, respectively, relative to the aligned position (i.e., $\Delta x = \Delta y = 0$). Reprinted with permission from Ref. [174]; copyright 2012 MDPI.

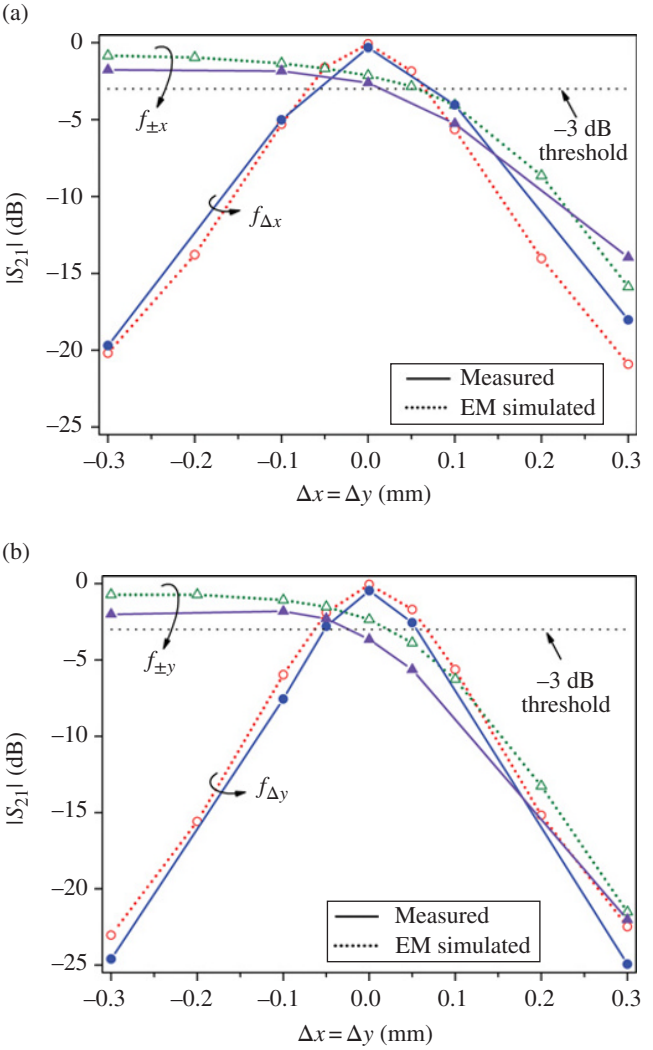

FIGURE 4.69 Notch magnitude of the transmission coefficient S_{21} at the indicated frequencies for $x = y$ displacement; results for (a) x- and (b) y-axis position sensing. Reprinted with permission from Ref. [174]; copyright 2012 MDPI.

one of the ELC) become aligned, and a strong notch in the transmission coefficient is expected. This explains that the dynamic range can be improved as compared to the rotation sensor based on a rectangular-shaped SRR. Linearity is improved thanks to optimization of resonator and line shape (the key aspect is that the external contour of the resonator roughly coincides with the slots of the nonuniform CPW host line).

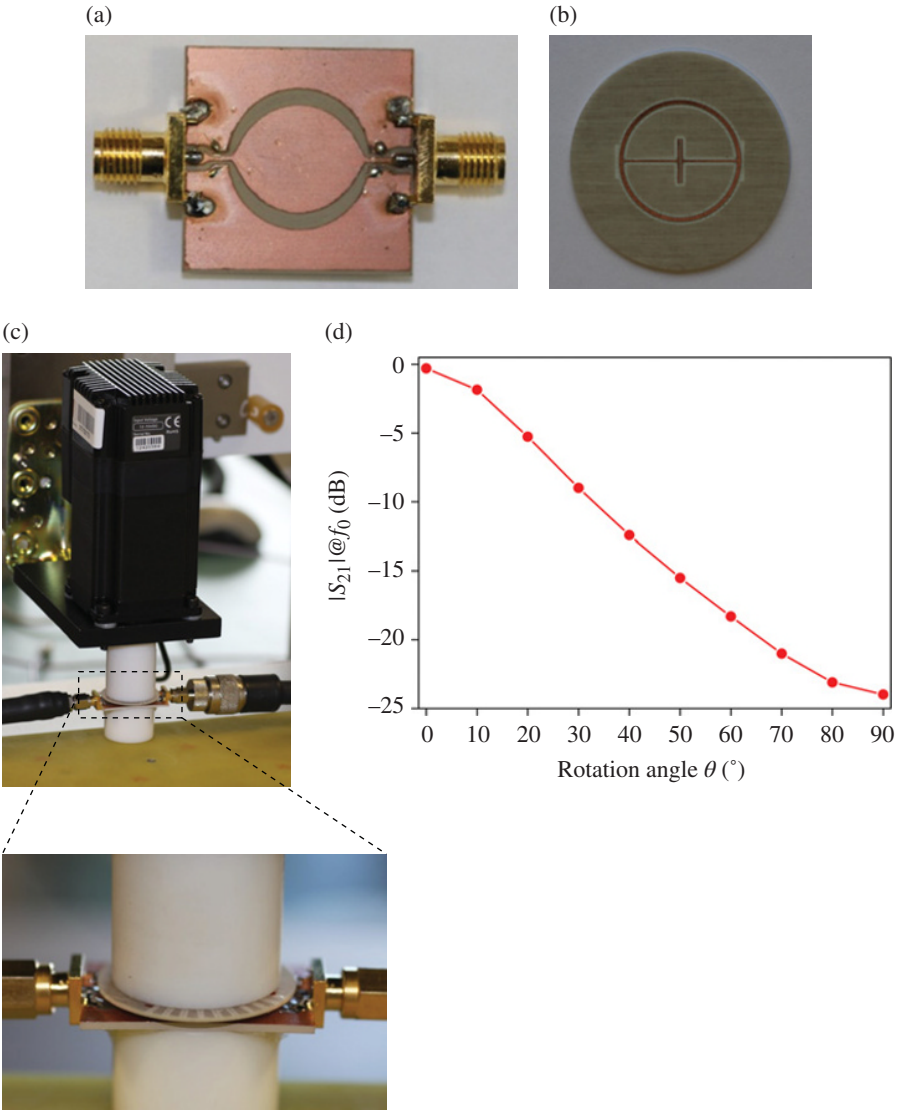

FIGURE 4.70 Photograph of the circular CPW (a) and ELC (b) used for sensing rotation angles through the setup shown in (c). The notch magnitude as a function of the rotation angle is depicted in (d). The ELC is attached to a rotating cylinder made of Teflon. The CPW and the ELC were etched on the *Rogers RO3010* substrate with thickness $h = 1.27$ mm, dielectric constant $\varepsilon_r = 11.2$, and loss tangent $\tan\delta = 0.0023$. Dimensions are: for the CPW, W and G are tapered such that the characteristic impedance is 50 Ω; for the ELC resonator, the diameter is 16.6 mm. Vias and backside strips are used to eliminate the slot mode.

The proof of concept of this rotation sensor was demonstrated in Ref. [175] by considering two different scenarios: (1) different CPW-loaded structures, each with the ELC etched in the back substrate side and rotated a different angle and (2) a single CPW with the ELC etched on a movable substrate. An experimental setup, where the ELC resonator is attached to a cylinder made of Teflon which can rotate through the action a step motor, was then implemented in order to perform angle and angular velocity measurements in rotating elements (Fig. 4.70). The notch depth in the transmission coefficient as a function of the rotation angle for the structure of Figure 4.70 is also depicted in the figure. Good linearity, dynamic range, and sensitivity can be appreciated.

The setup of Figure 4.70 was used for the measurement of angular velocities. The idea is very simple: the CPW transmission line is fed by a harmonic signal (carrier) tuned at the notch frequency of the ELC resonator.[39] At the output port of the CPW the amplitude of the carrier signal is modulated by the effect of the rotating ELC, that is, the amplitude is a maximum each time the electric wall of the ELC is aligned with the symmetry plane of the line (this occurs twice per cycle). Therefore, by rectifying the modulated signal through an envelope detector, the distance between adjacent peaks gives the rotation speed. In order to avoid unwanted reflections caused by the envelope detector, a circulator is cascaded between the output port of the CPW transmission line and the input of the envelope detector, as depicted in Figure 4.71a. The typical waveform obtained through an oscilloscope in the envelope detector, for a rotation speed of 10 cycles per second, is depicted in Figure 4.71b. The pronounced peaks allow for the measurement of angular velocities with high accuracy. Since the carrier frequency is very high, it is obvious that very high angular velocities can be measured with this approach. Further details on the design of this rotation speed sensor are given in Ref. [177]; an alternative version of the rotation speed sensor in microstrip technology is reported in Ref. [178].

4.3.2.3 RF Bar Codes As an example of a RF bar code implemented by symmetric resonators, a 3-bit structure is reported here. The structure is a CPW loaded with folded SIRs. Such resonators exhibit an electric wall in its symmetry plane at the fundamental resonance. By aligning them with the line, the structure is transparent for the corresponding resonance (logic '0' state). The logic '1' state is achieved by laterally displacing the folded SIR. Folded SIRs loading a CPW are interesting since they are electrically small at resonance. The reason is that line-to-resonator coupling is dominated by the large capacitance between the SIR and the line. The basic cell (for the symmetric configuration) and the circuit model are depicted in Figure 4.72 [162]. Coupling between the line and resonator is represented by the capacitances C_{sci} and C_{sgi} $(i = 1, 2)$. Such capacitances depend on the relative position between the SIR and the CPW. Thus, any symmetry truncation can be modeled by adjusting these capacitances. If the structure

[39] Actually, the notch frequency slightly depends on the orientation (angle) of the ELC resonator. Therefore, the carrier frequency is chosen as the average value.

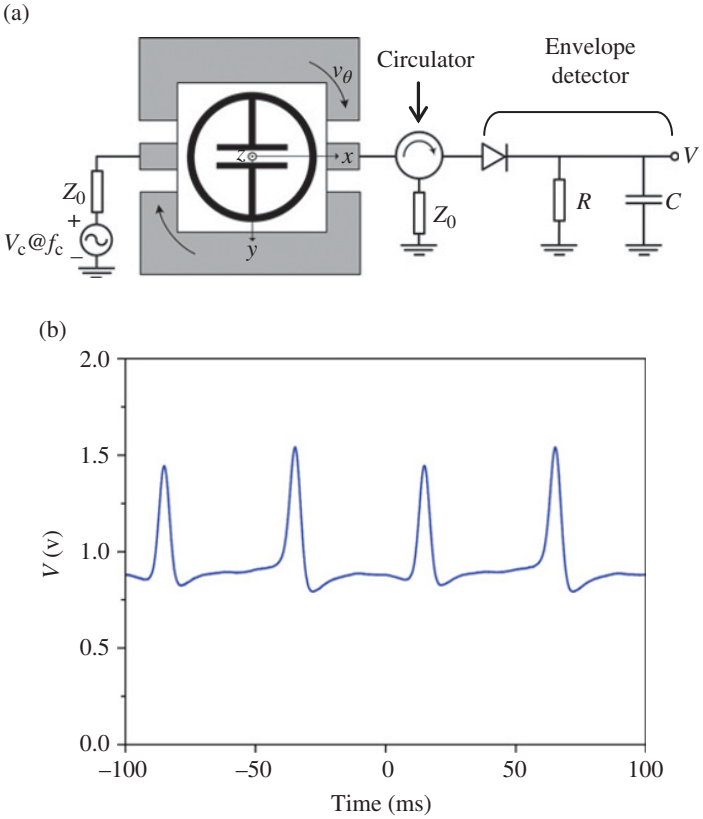

FIGURE 4.71 Schematic of the proposed system for measuring angular velocities in time domain, including the sensing line, circulator and envelope detector (a) and output waveform for a rotating speed of 10 cycles per second (b).

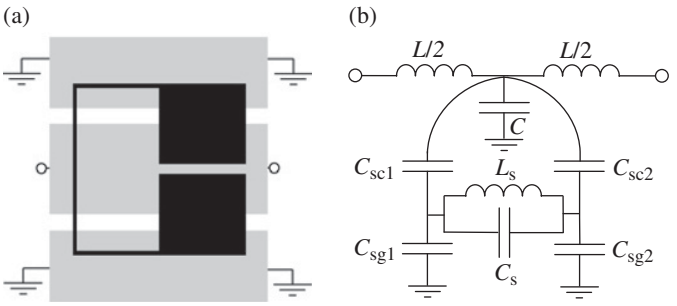

FIGURE 4.72 Typical layout of a CPW loaded with a folded SIR (a) and lumped-element equivalent circuit model (b). The metallization in the back substrate side is indicated in black.

is symmetric (i.e., $C_{sc1} = C_{sc2}$ and $C_{sg1} = C_{sg2}$), the resonator L_s–C_s is opened due to the presence of the magnetic wall at the symmetry plane, and the resulting model is the one of a conventional transmission line. By contrast, if the symmetry is broken, the capacitances are unbalanced and a transmission zero appears. In the simplest case in which $C_{sc1} = C_{sg2} = 0$ (or $C_{sc2} = C_{sg1} = 0$), the model is equivalent to that of a transmission line loaded with a grounded series resonator (the capacitance C_s can be neglected). The model parameters were extracted for the two cases indicated in Figure 4.73. In both cases, the circuit simulations are in good agreement with the EM simulations. For comparison purposes, the response of a CPW loaded with an SRR of the same dimensions is also included. It can be appreciated the interest of folded SIRs in this application, not only because the particles are electrically smaller, but also because the balance between notch depth and width is good. Narrow notches occupy less bandwidth, but at the expense of small notch depth due to losses.

A 3-bit RF bar code consisting of a CPW loaded with three different folded SIRs with the code '111' is depicted in Figure 4.74a [162]. In order to prevent the presence of the slot mode, the ground planes are connected through backside strips and vias. In view of the transmission coefficients of this structure and those corresponding to other bit configurations (Fig. 4.74b), the principle is validated. Although somehow

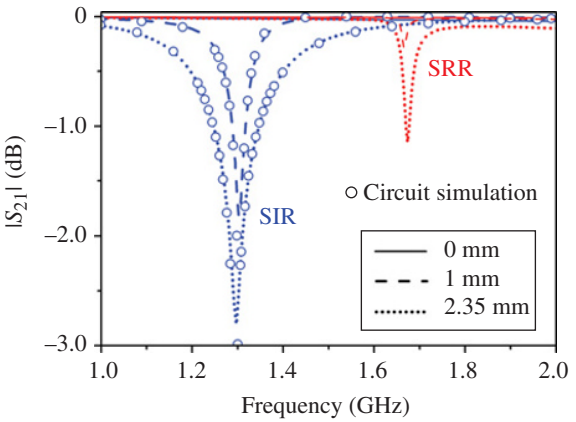

FIGURE 4.73 Simulated transmission coefficient of the structure of Figure 4.72a and those corresponding to the same structure with the resonators laterally displaced. The substrate is the *Rogers RO3010* with dielectric constant $\varepsilon_r = 10.2$, thickness $h = 0.635$ mm, and $\tan\delta = 0.0023$. CPW dimensions are $L_{CPW} = 9.6$ mm, $W = 4$ mm, and $G = 0.7$ mm; SIR dimensions are (in reference to Fig. 3.13): $l_1 = l_2 = 7.6$ mm, $W_1 = 3.8$ mm, $W_2 = 0.2$ mm, and $S = 0.4$ mm. Circuit parameters are $L = 2.4$ nH, $C = 0.97$ pF, $L_s = 13.8$ nH, $C_s = 0$pF; for 1 mm, $C_{sc1} = 0.57$ pF, $C_{sc2} = 1.8$ pF, $C_{sg1} = 1.6$ pF, and $C_{sg2} = 0.4$ pF; for 2.35 mm, $C_{sc1} = 0$ pF, and $C_{sc2} = 2.2$ pF, $C_{sg1} = 2.2$ pF, and $C_{sg2} = 0$pF. Reprinted with permission from Ref. [162]; copyright 2012 IEEE.

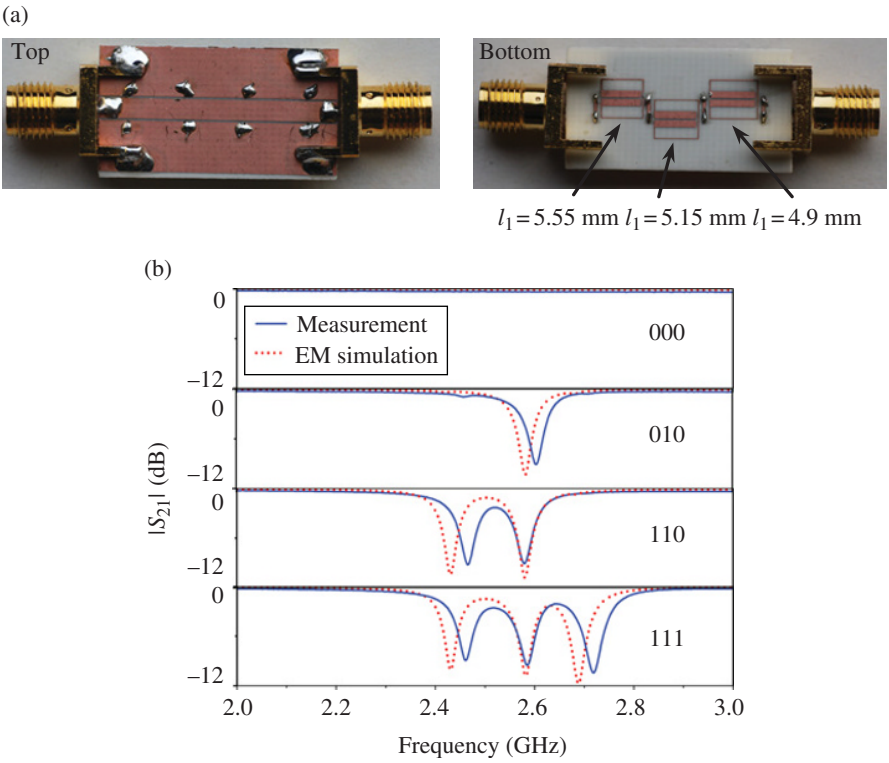

FIGURE 4.74 Fabricated CPW with three folded SIRs corresponding to the binary code '111' of a 3-bit RF bar code (a) and simulated and measured transmission coefficient of the structure corresponding to the indicated codes (b). The substrate is the *Rogers RO4003C* with $\varepsilon_r = 3.55$, $h = 0.8128$ mm, and $\tan\delta = 0.0021$. CPW dimensions are $L_{CPW} = 23.9$ mm, $W = 2.16$ mm, and $G = 0.15$ mm; SIR dimensions are (in reference to Fig. 3.13): $W_1 = 0.825$ mm, $W_2 = 0.15$ mm, $S = 0.15$ mm, $l_2 = 4.47$ mm, and l_1 is shown in the photograph. Reprinted with permission from Ref. [162]; copyright 2012 IEEE.

degraded, the bar code functionality (not shown) is still preserved if the backside strip and vias are removed.

RF-bar codes implemented with symmetric resonators in microstrip technology (thus avoiding the use of vias) have been also reported [179].

REFERENCES

1. G. V. Eleftheriades and K. G. Balmain, Ed., *Negative-Refraction Metamaterials: Fundamental Principles and Applications*, Wiley-Interscience, Hoboken, NJ, 2005.
2. C. Caloz and T. Itoh, *Electromagnetic Metamaterials: Transmission Line Theory and Microwave Applications*, John Wiley & Sons, Hoboken, NJ, 2006.

3. N. Engheta and R. W. Ziolkowski, *Metamaterials: Physics and Engineering Explorations*, Wiley-Interscience, Hoboken, NJ, 2006.
4. R. Marqués, F. Martín, and M. Sorolla, *Metamaterials with Negative Parameters: Theory, Design and Microwave Applications*, Wiley-Interscience, Hoboken, NJ, 2007.
5. F. Capolino, Ed., *Metamaterials Handbook*, CRC Press, Boca Raton, FL, 2009.
6. L. Solymar and E. Shamonina, *Waves in Metamaterials*, Oxford University Press, Oxford, 2009.
7. G. Sisó, M. Gil, J. Bonache, and F. Martín, "On the dispersion characteristics of metamaterial transmission lines," *J. Appl. Phys.*, vol. **102**, paper 074911, 2007.
8. R. A. Foster, "A reactance theorem," *Bell System Tech. J.*, vol. **3**, pp. 259–267,1924.
9. M. Gil, J. Bonache, I. Gil, J. García-García, and F. Martín, "Miniaturization of planar microwave circuits by using resonant-type left handed transmission lines," *IET Microw. Antennas Propag.*, vol. **1**, pp. 73–79, 2007.
10. M. A. Antoniades and G. V. Eleftheriades, "A broadband series power divider using zero-degree metamaterial phase shifting lines," *IEEE Microw. Wireless Compon. Lett.*, vol. **15**, pp. 808–810, 2005.
11. H. Okabe, C. Caloz, and T. Itoh, "A compact enhanced bandwidth hybrid ring using an artificial lumped element left handed transmission line section," *IEEE Trans. Microw. Theory Tech.*, vol. **52**, pp. 798–804, 2004.
12. G. Sisó, J. Bonache, M. Gil, J. García-García, and F. Martín, "Compact rat-race hybrid coupler implemented through artificial left handed and right handed lines," *IEEE MTT-S Int. Microwave Symp. Dig.*, Honolulu, HI, June 2007, pp. 25–28.
13. G. Sisó, J. Bonache, M. Gil, and F. Martín, "Application of resonant-type metamaterial transmission lines to the design of enhanced bandwidth components with compact dimensions," *Microw. Opt. Technol. Lett.*, vol. **50**, pp. 127–134, 2008.
14. R. K. Settaluri, G. Sundberg, A. Weisshaar, and V. K. Tripathi, "Compact folded line rat race hybrid couplers," *IEEE Microw. Guided Wave Lett.*, vol. **10**, pp. 61–63, 2000.
15. K. W. Eccleston and S. H. M. Ong, "Compact planar microstripline branch-line and rat race couplers," *IEEE Trans. Microw. Theory Tech.*, vol. **51**, pp. 2119–2125, 2003.
16. C.-C. Chen and C.-K. C. Tzuang, "Synthetic quasi-TEM meandered transmission lines for compacted microwave integrated circuits," *IEEE Trans. Microw. Theory Tech.*, vol. **52**, pp. 1637–1647, 2004.
17. J.-T. Kuo, J.-S. Wu, and Y.-C. Chiou, "Miniaturized rat race coupler with suppression of spurious passband," *IEEE Microw. Wireless Compon. Lett.*, vol. **17**, pp. 46–48, 2007.
18. T. T. Mo, Q. Xue, and C. H. Chan, "A broadband compact microstrip rat-race hybrid using a novel CPW inverter," *IEEE Trans. Microw. Theory Tech.*, vol. **55**, pp. 161–167, 2007.
19. I. B. Vendik, O. G. Vendik, D. V. Kholodnyak, E. V. Serebryakova, and P. V. Kapitanova, "Digital phase shifters based on right- and left-handed transmission lines," *Proc. Eur. Microw. Assoc.*, vol. **2**, pp. 30–37, 2006.
20. I. T. Nassar, A. A. Gheethan, T. M. Weller, and G. Mumcu, "A Miniature, broadband, non-dispersive phase shifter based on CRLH TL unit cells," *IEEE Int. Symp. Antennas Propag. (APS-URSI)*, Chicago, IL, 2012.
21. M. A. Antoniades and G. V. Eleftheriades, "A broadband Wilkinson balun using microstrip metamaterial lines," *IEEE Antennas Wireless Propag. Lett.*, vol. **4**, pp. 209–212, 2005.

22. S.-G. Mao and Y.-Z. Chueh, "Broadband composite right/left-handed coplanar waveguide power splitters with arbitrary phase responses and balun and antenna applications," *IEEE Trans. Antennas Propag.*, vol. **54**, pp. 243–250, 2006.
23. G. Sisó, M. Gil, J. Bonache, and F. Martín, "Application of metamaterial transmission lines to the design of quadrature phase shifters," *Electron. Lett.*, vol. **43**, pp. 1098–1100, 2007.
24. I.-H. Lin, M. DeVincentis, C. Caloz, and T. Itoh, "Arbitrary dual-band components using composite right/left-handed transmission lines," *IEEE Trans. Microw. Theory Tech.*, vol. **52**, pp. 1142–1149, 2004.
25. I.-H. Lin, K. M. K. H. Leong, C. Caloz, and T. Itoh, "Dual-band sub-harmonic quadrature mixer using composite right/left-handed transmission lines," *IEE Proc. Microw. Antennas Propag.*, vol. **153**, pp. 365–375, 2006.
26. C.-H. Tseng and T. Itoh, "Dual-band bandpass and bandstop filters using composite right/left-handed metamaterial transmission lines," *IEEE MTT-S Int. Microwave Symp. Dig.*, San Francisco, CA, June 2006, pp. 931–934.
27. S. H. Ji, C. S. Cho, J. W. Lee, and J. Kim, "Concurrent dual-band class-E power amplifier using composite right/left-handed transmission lines," *IEEE Trans. Microw. Theory Tech.*, vol. **55**, pp. 1341–1347, 2007.
28. M. Durán-Sindreu, A. Vélez, F. Aznar, G. Sisó, J. Bonache, and F. Martín, "Application of open split ring resonators and open complementary split ring resonators to the synthesis of artificial transmission lines and microwave passive components," *IEEE Trans. Microw. Theory Tech.*, vol. **57**, pp. 3395–3403, 2009.
29. J. Selga, A. Rodríguez, V. E. Boria, and F. Martín, "Synthesis of split rings based artificial transmission lines through a new two-step, fast converging, and robust aggressive space mapping (ASM) algorithm," *IEEE Trans. Microw. Theory Tech.*, vol. **61**, pp. 2295–2308, 2013.
30. G. Sisó, J. Bonache, and F. Martín, "Dual-band Y-junction power dividers implemented through artificial lines based on complementary resonators," *IEEE MTT-S Int. Microwave Symp. Dig.*, Atlanta, GA, June 2008, pp. 663–666.
31. J. Bonache, G. Sisó, M. Gil, A. Iniesta, J. García-Rincón, and F. Martín, "Application of composite right/left handed (CRLH) transmission lines based on complementary split ring resonators (CSRRs) to the design of dual band microwave components," *IEEE Microw. Wireless Compon. Lett.*, vol. **18**, pp. 524–526, 2008.
32. A. Vélez, G. Sisó, A. Campo, M. Durán-Sindreu, J. Bonache, and F. Martín, "Dual-band microwave duplexer based on spiral resonators (SR) and complementary split ring resonators (CSRRs)," *Appl. Phys. A Mater. Sci. Proc.*, vol. **103**, pp. 911–914, 2011.
33. J.-S. Hong and M. J. Lancaster, *Microstrip Filters for RF/Microwave Applications*, Wiley, Hoboken, NJ, 2001.
34. M. Durán-Sindreu, G. Sisó, J. Bonache, and F. Martín, "Fully planar implementation of generalized composite right/left handed transmission lines for quad-band applications," *IEEE-MTT-S Int. Microwave Symp. Dig.*, Anaheim, CA, May 2010.
35. M. Durán-Sindreu, G. Sisó, J. Bonache, and F. Martín, "Planar multi-band microwave components based on the generalized composite right/left handed transmission line concept," *IEEE Trans. Microw. Theory Tech.*, vol. **58**, pp. 3882–3891, 2010.
36. B. H. Chen, Y. N. Zhang, D. Wu, and K. Seo, "A novel composite right/left-handed transmission line for quad-band applications," *11th IEEE Singapore International Conference on Communication Systems (ICCS)*, Guangzhou, November 2008, pp. 617–620.

37. A. C. Papanastasiou, G. E. Georghiou, and G. V. Eleftheriades, "A quad-band wilkinson power divider using generalized NRI transmission lines," *IEEE Microw. Wireless Compon. Lett.*, vol. **18**, pp. 521–523, 2008.

38. A. Rennings, T. Liebig, C. Caloz, and I. Wolff, "Double-Lorentz transmission line metamaterials and its applications to tri-band devices," *IEEE MTT-S Int. Microwave Symp. Dig.*, Honolulu, HA, June 2007, pp. 1427–1430.

39. K.-K. M. Cheng and C. Law, "A novel approach to the design and implementation of dual-band power divider," *IEEE Trans. Microw. Theory Tech.*, vol. **56**, pp. 487–492, 2008.

40. K.-S. Chin, K.-M. Lin, Y.-H. Wei, T.-H. Tseng, and Y.-J. Yang, "Compact dual-band branch-line and rat-race couplers with stepped-impedance-stub lines," *IEEE Trans. Microw. Theory Tech.*, vol. **58**, pp. 1213–1221, 2010.

41. M. Gil, J. Bonache, and F. Martín, "Metamaterial filters: a review," *Metamaterials*, vol. **2**, pp. 186–197, 2008.

42. F. Martín, F. Falcone, J. Bonache, R. Marqués, and M. Sorolla, "Miniaturized CPW stop band filters based on multiple tuned split ring resonators," *IEEE Microw. Wireless Compon. Lett.*, vol. **13**, pp. 511–513, 2003.

43. J. García-García, J. Bonache, I. Gil, F. Martín, R. Marqués, F. Falcone, T. Lopetegi, M. A. G. Laso, and M. Sorolla, "Comparison of electromagnetic bandgap and split rings resonator microstrip lines as stop band structures," *Microw. Opt. Technol. Lett.*, vol. **44**, pp. 376–379, 2005.

44. J. García-García, F. Martín, F. Falcone, J. Bonache, J. D. Baena, I. Gil, E. Amat, T. Lopetegi, M. A. G. Laso, J. A. Marcotegui-Iturmendi, M. Sorolla, and R. Marqués, "Microwave filters with improved stop band based on sub-wavelength resonators," *IEEE Trans. Microw. Theory Tech.*, vol. **53**, pp. 1997–2006, 2005.

45. M. Gil, J. Bonache, and F. Martín, "Synthesis and applications of new left handed microstrip lines with complementary split rings resonators (CSRRs) etched in the signal strip," *IET Microw. Antennas Propag.*, vol. **2**, pp. 324–330, 2008.

46. C. Person, A. Sheta, J. Ocupes, and S. Toutain, "Design of high performance band pass filters by using multilayer thick film technology," *Proc. 24th Eur. Microw. Conf.*, Cannes, France, September 1994, vol. **1**, pp. 446–471.

47. J. T. Kuo and M. Jiang, "Suppression of spurious resonance for microstrip band pass filters via substrate suppression," *Asia Pac. Microw. Conf.*, Kyoto, Japan, 2002, pp. 497–500.

48. M. Le Roy, A. Perennec, S. Toutain, and L. C. Calvez, "Continously varying coupled transmission lines applied to design band pass filters," *Int. J. RF Microw. Comput. Aided Eng.*, vol. **12**, pp. 288–295, 2002.

49. J. T. Kuo and W. Hsu, "Parallel coupled microstrip filters with suppression of harmonic response," *IEEE Microw. Wireless Compon. Lett.*, vol. **12**, pp. 383–385, 2002.

50. J. García-García, F. Martín, F. Falcone, J. Bonache, I. Gil, T. Lopetegi, M. A. G. Laso, M. Sorolla, and R. Marqués, "Spurious passband suppression in microstrip coupled line band pass filters by means of split ring resonators," *IEEE Microw. Wireless Compon. Lett.*, vol. **14**, pp. 416–418, 2004.

51. J. García-García, J. Bonache, F. Falcone, J. D. Baena, F. Martín , I. Gil, T. Lopetegi, M. A. G. Laso, A. Marcotegui, R. Marqués, and M. Sorolla, "Stepped-impedance low pass filters with spurious passband suppression," *Electron. Lett.*, vol. **40**, pp. 881–883, 2004.

52. J. Bonache, F. Martín, F. Falcone, J. García, I. Gil, T. Lopetegi, M. A. G. Laso, R. Marqués, F. Medina, and M. Sorolla, "Super compact split ring resonators CPW band pass filters," *IEEE-MTT-S Int. Microw. Symp. Dig.*, Fort Worth, TX, June 2004, pp. 1483–1486.

53. J. Bonache, F. Martín, F. Falcone, J. D. Baena, T. Lopetegi, J. García-García, M. A. G. Laso, I. Gil, A. Marcotegui, R. Marqués, and M. Sorolla, "Application of complementary split rings resonators to the design of compact narrow band pass structures in microstrip technology," *Microw. Opt. Technol. Lett.*, vol. **46**, pp. 508–512, 2005.

54. P. Mondal, M. K. Mandal, A. Chaktabarty, and S. Sanyal, "Compact bandpass filters with wide controllable fractional bandwidth," *IEEE Microw. Wireless Compon. Lett.*, vol. **16**, pp. 540–542, 2006.

55. J. Bonache, F. Martín, F. Falcone, J. García-García, I. Gil, T. Lopetegi, M. A. G. Laso, R. Marqués, F. Medina, M. Sorolla, "Compact coplanar waveguide band pass filter at S-band," *Microw. Opt. Technol. Lett.*, vol. **46**, pp. 33–35, 2005.

56. J. Bonache, I. Gil, J. García-García, and F. Martín, "Complementary split rings resonator for microstrip diplexer design," *Electron. Lett.*, vol. **41**, pp. 810–811, 2005.

57. J. Bonache, I. Gil, J. García-García, and F. Martín, "Novel microstrip band pass filters based on complementary split rings resonators," *IEEE Trans. Microw. Theory Tech.*, vol. **54**, pp. 265–271, 2006.

58. G. L. Matthaei, L. Young, and E. M. T. Jones, *Microwave Filters, Impedance-Matching Networks, and Coupling Structures*, Artech House, Norwood, MA, 1980.

59. D. M. Pozar, *Microwave Engineering*, Addison Wesley, Reading, MA 1990.

60. J. D. Baena, J. Bonache, F. Martín, R. Marqués, F. Falcone, T. Lopetegi, M. A. G. Laso, J. García, I. Gil and M. Sorolla, "Equivalent circuit models for split ring resonators and complementary split rings resonators coupled to planar transmission lines," *IEEE Trans. Microw. Theory Tech.*, vol. **53**, pp. 1451–1461, 2005.

61. J. Bonache, G. Posada, G. Garchon, W. De Raedt, and F. Martín, "Compact ($<0.5\text{mm}^2$) K-band metamaterial band pass filter in MCM-D technology," *Electron. Lett.*, vol. **43**, pp. 45–46, 2007.

62. J. Bonache, F. Martín, J. García-García, I. Gil, R. Marqués, and M. Sorolla, "Ultra wide band pass filtres (UWBPF) based on complementary split rings resonators," *Microw. Opt. Technol. Lett.*, vol. **46**, pp. 283–286, 2005.

63. J. Bonache, F. Martín, I. Gil, J. García-García, R. Marqués, and M. Sorolla, "Microstrip bandpass filters with wide bandwidth and compact dimensions," *Microw. Opt. Technol. Lett.*, vol. **46**, pp. 343–346, 2005.

64. J. Bonache, I. Gil, J. García-García, and F. Martín, "Complementary split rings resonators (CSRRs): towards the miniaturization of microwave device design," *J. Comput. Electron.*, vol. **5**, pp. 193–197, 2006.

65. J. Bonache, J. Martel, I. Gil, M. Gil, J. García-García, F. Martín, I. Cairó, and M. Ikeda, "Super compact ($<1\text{cm}^2$) band pass filters with wide bandwidth and high selectivity at C-band," *Proc. Eur. Microw. Conf.*, Manchester, UK, September 2006, pp. 599–602.

66. M. Gil, J. Bonache, J. García-García, J. Martel, and F. Martín, "Composite right/left handed (CRLH) metamaterial transmission lines based on complementary split rings resonators (CSRRs) and their applications to very wide band and compact filter design," *IEEE Trans. Microw. Theory Tech.*, vol. **55**, pp. 1296–1304, 2007.

67. A. Vélez, P. Vélez, J. Bonache, and F. Martín, "Compact power dividers with filtering capability for ground penetrating radar (GPR) applications," *Microw. Opt. Technol. Lett.*, vol. **54**, pp. 608–611, 2012.

68. M. Durán-Sindreu, A. Vélez, G. Sisó, J. Selga, P. Vélez, J. Bonache, and F. Martín, "Recent advances in metamaterial transmission lines based on split rings," *Proc. IEEE*, vol. **99**, pp. 1701–1710, 2011.

69. D.-J. Woo, T.-K. Lee, "Suppression of harmonics in Wilkinson power divider using dual-band rejection by asymmetric DGS," *IEEE Trans. Microw. Theory Tech.*, vol. **53**, pp. 2139–2144, 2005.

70. C.-M. Lin, H.-H. Su, J.-C. Chiu, and Y.-H. Wang, "Wilkinson power divider using microstrip EBG cells for the suppression of harmonics," *IEEE Microw. Wireless Compon. Lett.*, vol. **17**, pp. 700–702, 2007.

71. J. Selga, M. Gil, J. Bonache, and F. Martín, "Composite right/left handed coplanar waveguides loaded with split ring resonators and their application to high pass filters," *IET Microw. Antennas Propag.*, vol. **4**, pp. 822–827, 2010.

72. M. Gil, J. Bonache, J. García-García, and F. Martín, "Metamaterial filters with attenuation poles in the pass band for ultra wide band (UWB) applications," *Microw. Opt. Technol. Lett.*, vol. **49**, pp. 2909–2913, 2007.

73. J. Martel, R. Marqués, F. Falcone, J. D. Baena, F. Medina, F. Martín, and M. Sorolla, "A new LC series element for compact band pass filter design," *IEEE Microw. Wireless Compon. Lett.*, vol. **14**, pp. 210–212, 2004.

74. J. Martel, J. Bonache, R. Marqués, F. Martín, and F. Medina, "Design of wide-band semi-lumped bandpass filters using open split ring resonators," *IEEE Microw. Wireless Compon. Lett.*, vol. **17**, pp. 28–30, 2007.

75. A. Velez, F. Aznar, J. Bonache, M. C. Velázquez-Ahumada, J. Martel, and F. Martín, "Open complementary split ring resonators (OCSRRs) and their application to wideband CPW band pass filters," *IEEE Microw. Wireless Compon. Lett.*, vol. **19**, pp. 197–199, 2009.

76. M. Durán-Sindreu, *Miniaturization of planar microwave components based on semi-lumped elements and artificial transmission lines: application to multi-band devices and filters*, PhD dissertation, Universitat Autònoma de Barcelona, Barcelona, 2011.

77. M. Durán-Sindreu, P. Vélez, J. Bonache, and F. Martín, "High-order coplanar waveguide (CPW) filters implemented by means of open split ring resonators (OSRRs) and open complementary split ring resonators (OCSRRs)," *Metamaterials*, vol. **5**, pp. 51–55, 2011.

78. M. Durán-Sindreu, P. Vélez, J. Bonache, and F. Martín, "Broadband microwave filters based on open split ring resonators (OSRRs) and open complementary split ring resonators (OCSRRs): improved models and design optimization," *Radioengineering*, vol. **20**, pp. 775–783, 2011.

79. X. Guan, Z. Ma, P. Cai, Y. Kobayashi, T. Anada, and G. Hagiwara, "Synthesis of dual-band bandpass filters using successive frequency transformations and circuit conversions," *IEEE Microw. Wireless Compon. Lett.*, vol. **16**, pp. 110–112, 2006.

80. F. Aznar, A. Vélez, M. Durán-Sindreu, J. Bonache, and F. Martín, "Elliptic-function CPW low-pass filters implemented by means of open complementary split ring resonators (OCSRRs)," *IEEE Microw. Wireless Compon. Lett.*, vol. **19**, pp. 689–691, 2009.

81. F. Giannini, M. Salerno, and R. Sorrentino, "Effects of parasitics in lowpass elliptic filters for MIC," *Electron. Lett.*, vol. **18**, pp. 284–285, 1982.

82. F. Giannini, M. Salerno, and R. Sorrentino, "Design of low-pass elliptic filters by means of cascaded microstrip rectangular elements," *IEEE Trans. Microw. Theory Tech.*, vol. **MTT-30**, pp. 1348–1353, 1982.
83. L. H. Hsieh and K. Chang, "Compact elliptic-function low-pass filters using microstrip stepped-impedance hairpin resonators," *IEEE Trans. Microw. Theory Tech.*, vol. **51**, pp. 193–199, 2001.
84. N. Yang, Z. N. Chen, Y. Y. Wang, and M. Y. W. Chia, "An elliptic low-pass filter with shorted cross-over and broadside-coupled microstrip lines," *IEEE-MTT-S Int. Microw. Symp. Dig.*, Philadelphia, PA, June 2003, vol. **1**, pp. 535–538.
85. W. Tu and K. Chang, "Compact microstrip low-pass filter with sharp rejection," *IEEE Microw. Wireless Compon. Lett.*, vol. **15**, pp. 404–406, 2005.
86. W. Tu and K. Chang, "Microstrip elliptic-function low-pass filters using distributed elements or slotted ground structure," *IEEE Trans. Microw. Theory Tech.*, vol. **54**, pp. 3786–3792, 2006.
87. M. C. Velazquez-Ahumada, J. Martel, and F. Medina, "Design of compact low-pass elliptic filters using double-sided MIC technology," *IEEE Trans. Microw. Theory Tech.*, vol. **55**, pp. 121–127, 2007.
88. A. Balalem, A. R. Ali, J. Machac, and A. Omar, "Quasi-elliptic microstrip low-pass filters using an interdigital DGS slot," *IEEE Microw. Wireless Compon. Lett.*, vol. **17**, pp. 586–588, 2007.
89. B. Wu, B. Li, and C. Liang, "Design of lowpass filter using a novel split-ring resonator defected ground structure," *Microw. Opt. Technol. Lett.*, vol. **49**, pp. 288–291, 2007.
90. X. Chen, L. Weng, and X. Shi, "Novel complementary split ring resonator DGS for low-pass filter design," *Microw. Opt. Technol. Lett.*, vol. **51**, pp. 1748–1751, 2009.
91. F. Aznar, A. Vélez, J. Bonache, J. Menés, and F. Martín, "Compact low pass filters with very sharp transition bands based on open complementary split ring resonators (OCSRRs)," *Electron. Lett.*, vol. **45**, pp. 316–317, 2009.
92. A. A. Oliner, "Leaky-wave antennas," in *Antenna Engineering Handbook*, R. C. Johnson, Ed. McGraw-Hill, New York, pp. 10-1–10-59, 1993.
93. F. B. Gross, Ed., *Frontiers in Antennas: Next Generation Design & Engineering*, McGraw Hill, New York, 2011.
94. J. L. Volakis, Ed., *Antenna Engineering Handbook*, 4th Edition, McGraw Hill, London, 2007.
95. C. A. Balanis, Ed., *Modern Antenna Handbook*, Wiley, Hoboken, NJ, 2008.
96. D. R. Jackson, C. Caloz, and T. Itoh, "Leaky wave antennas," *Proc. IEEE*, vol. **100**, pp. 2194–2206, 2012.
97. L. Liu, C. Caloz, and T. Itoh, "Dominant mode leaky-wave antenna with backfire to endfire scanning capability," *Electron. Lett.*, vol **38**, pp. 1414–1416, 2002.
98. A. Grbic and G. V. Eleftheriades, "Experimental verification of backward wave radiation from a negative refractive index metamaterial," *J. Appl. Phys.*, vol. **92**, pp. 5930–5935, 2002.
99. A. Grbic and G. V. Eleftheriades, "Leaky CPW-based slot antenna arrays for millimeter-wave applications," *IEEE Trans. Antennas Propag.*, vol. **50**, pp. 1494–1504, 2002.
100. W. Menzel, "A new travelling-wave antenna in microstrip," *Arch. Elek. Ubertragung.*, vol. **33**, pp. 137–140, 1979.

101. A. Oliner and K. Lee, "Microstrip leaky wave strip antennas," *Proc. IEEE Int. Symp. Antennas Propag. Symp.*, Philadelphia, PA, June 1986, pp. 443–446.

102. Y. Lin, J. Sheen, and C. Tzuang, "Analysis and design of feeding structures for microstrip leaky wave antenna," *IEEE Trans. Microw. Theory Tech.*, vol. **44**, pp. 1540–1547, 1996.

103. P. Burghignoli, G. Lovat, and D. R. Jackson, "Analysis and optimization of leaky-wave radiation at broadside from a class of 1-D periodic structures," *IEEE Trans. Antennas Propag.*, vol. **54**, pp. 2593–2603, 2006.

104. S. Paulotto, P. Baccarelli, F. Frezza, and D. R. Jackson, "A novel technique for open-stopband suppression in 1-D periodic printed leaky-wave antennas," *IEEE Trans. Antennas Propag.*, vol. **57**, pp. 1894–1906, 2009.

105. I. Arnedo, J. Illescas, M. Flores, M. A. G. Laso, F. Falcone, J. Bonache, J. García-García, F. Martín, J. A. Marcotegui, R. Marques, and M. Sorolla, "Forward and backward leaky wave radiation in split-ring-resonator-based metamaterials," *IET Microw. Antennas Propag.*, vol. **1**, pp. 65–68, 2007.

106. G. Zamora, S. Zuffanelli, F. Paredes, F. J. Herraiz Martínez, F. Martín, and J. Bonache, "Fundamental mode leaky-wave antenna (LWA) using slot line and split-ring-resonator (SRR)-based metamaterials," *IEEE Antennas Wireless Propag. Lett.*, vol. **12**, pp. 1424–1427, 2013.

107. T. Kokkinos, C. D. Sarris, and G. V. Eleftheriades, "Periodic FDTD analysis of leaky-wave structures and applications to the analysis of negative-refractive-index leaky-wave antennas," *IEEE Trans. Microw. Theory Tech.*, vol. **54**, pp. 1619–1630, 2006.

108. S. Eggermont and I. Huynen, "Leaky wave radiation phenomena in metamaterial transmission line based on complementary split ring resonators," *Microw. Opt. Technol. Lett.*, vol. **53**, pp. 2025–2029, 2011.

109. M. A. Antoniades and G. V. Eleftheriades, "A CPS leaky-wave antenna with reduced beam squinting using NRI-TL metamaterials," *IEEE Trans. Antennas Propag.*, vol. **56**, pp. 708–721, 2008.

110. J. Machac and M. Polivka, "A dual band SIW leaky wave antenna," *IEEE-MTT Int. Microwave Symp. Dig.*, Montréal, Canada, June 2012.

111. M. Durán-Sindreu, J. Choi, J. Bonache, F. Martín, and T. Itoh, "Dual-band leaky wave antenna with filtering capability based on extended-composite right/left-handed transmission lines," *IEEE MTT-S Int. Microw. Symp. Dig.*, Seattle, WA, June 2013.

112. S. Lim, C. Caloz, and T. Itoh, "Electronically scanned composite right/left handed microstrip leaky-wave antenna," *IEEE Microw. Wireless Compon. Lett.*, vol. **14**, pp. 277–279, 2004.

113. S. Lim, C. Caloz, and T. Itoh, "Metamaterial-based electronically-controlled transmission line structure as a novel leaky-wave antenna with tunable angle and beamwidth," *IEEE Trans. Microw. Theory Tech.*, vol. **52**, pp. 2678–2690, 2004.

114. C. G. M. Ryan and G. V. Eleftheriades, "A dual-band leaky-wave antenna based on generalized negative-refractive-index transmission-lines," *IEEE Int. Symp. Antennas Propag. (APS-URSI)*, Toronto, Canada, July 2010.

115. F. P. Casares-Miranda, C. Camacho-Peñalosa, and C. Caloz, "High-gain active composite right/left-handed leaky-wave antenna," *IEEE Trans. Antennas Propag.*, vol. **54**, pp. 2292–2300, 2006.

116. P. de Paco, R. Villarino, G. Junkin, O. Menéndez, E. Corrales, and J. Parrón, "Dual-band mixer using composite right/left-handed transmission lines," *IEEE Microw. Wireless Compon. Lett.*, vol. **17**, pp. 607–609, 2007.

117. S. H. Ji, G. S. Hwang, C. S. Cho, J. W. Lee, and J. Kim, "836 MHz/1 .95GHz dual-band class-E power amplifier using composite right/left-handed transmission lines," *Proc. 36th Eur. Microw. Conf.*, Manchester, UK, September 2006, pp. 356–359.

118. E. L. Ginzton, W. R. Hewlett, J. H. Jasberg, and J. D. Noe, "Distributed amplification," *IRE*, vol. **36**, pp. 956–969, 1948.

119. T. Wong, *Fundamental of Distributed Amplification*, Artech House, Boston, MA, 1993.

120. G. W. McIver, "A travelling wave transistor," *IRE*, vol. **53**, pp. 1747–1748, 1965.

121. W. Jutzi, "A MESFET distributed amplifier with 2GHz bandwidth," *Proc. IEEE*, vol. **57**, pp. 1195–1196, 1969.

122. Y. Ayasli, J. L. Vorhaus, R. Mozzi, and L. Reynolds, "Monolithic GaAs travelling-wave amplifier," *Electron. Lett.*, vol. **17**, pp. 12–13, 1981.

123. J. A. Archer, F. A. Petz, H. P. Weidlich, "GaAs FET distributed amplifier," *Electron. Lett.*, vol. **17**, p. 433, 1981.

124. E. W. Strid, K. R. Gleason, "A DC-12 GHz monolithic GaAs FET distributed amplifier," *IEEE Trans. Microw. Theory Tech.*, vol. **30**, pp. 969–975, 1982.

125. C. S. Aitchison, N. Bukhari, C. Law, and N. Nazoa-Ruiz, "The dual-fed distributed amplifier," *IEEE MTT-S Int. Microwave Symp. Dig.*, New York, May 1988, vol. **2**, pp. 911–914.

126. P. N. Shastry and A. S. Ibrahim, "Design guidelines for a novel tapered drain line distributed power amplifier," *Proc. 36th Eur. Microw. Conf.*, Manchester, UK, September 2006, pp. 1274–1277.

127. J. Gassmann, P. Watson, L. Kehias, and G. Henry, "Wideband, high-efficiency GaN power amplifiers utilizing a non-uniform distributed topology," *IEEE MTT-S Int. Microwave Symp. Dig.*, Honolulu, HI, June 2007, vol. **1**, pp. 615–618.

128. P. N. Shastry and E. W. Cullerton, "A novel wideband GaAs FET source injected distributed mixer," *Proc. 36th Eur. Microw. Conf.*, Manchester, UK, September 2006, pp. 1533–1536.

129. F.-C. Chang, P.-S. Wu, M.-F. Lei, and H. Wang, "A 4–41 GHz singly balanced distributed mixer using GaAs pHEMT technology," *IEEE Microw. Wireless Compon. Lett.*, vol. **17**, pp. 136–138, 2007.

130. O. S. A. Tang and C. S. Atchison, "A practical microwave travelling-wave MESFET gate mixer," *IEEE MTT-S Int. Microwave Symp. Dig.*, Sant Louis, MO, June 1985, pp. 605–608.

131. O. S. A. Tang and C. S. Atchison, "Very wide-band microwave MESFET mixer using the distributed mixing principle," *IEEE Trans. Microw. Theory Tech.*, vol. **33**, pp. 1470–1478, 1985.

132. W. K. Eccleston, "Application of left-handed media in distributed amplifiers," *Microw. Opt. Tech. Lett.*, vol.**44**, pp. 527–530, 2005.

133. J. Mata-Contreras, T. M. Martín-Guerrero, and C. Camacho-Peñalosa, "Distributed amplifiers with composite left/right-handed transmission lines," *Microw. Opt. Technol. Lett.*, vol.**48**, pp. 609–613, 2006.

134. J. Mata-Contreras, C. Camacho-Peñalosa, and T. M. Martín-Guerrero, "Active distributed mixers based on composite right/left-handed transmission lines," *IEEE Trans. Microw. Theory Tech.*, vol. **57**, pp. 1091–1101, 2009.

135. J. Mata-Contreras, *Amplificadores y Mezcladores Distribuidos con Líneas de Transmision basadas en Metamateriales*, PhD dissertation, University of Málaga, Málaga, Spain, 2010.

136. J. Mata-Contreras, T. M. Martín-Guerrero, and C. Camacho-Peñalosa, "Experimental performance of a meta-distributed amplifier," *Proc. 37th Eur Microw Conf*, Munich, Germany, October 2007, pp. 743–746.

137. C. Xie, "Directional dual band distributed power amplifier with composite left/right-handed transmission lines," *IEEE MTT-S Int. Microw. Symp. Dig.*, Atlanta, GA, June 2008, pp. 1135–1138.

138. K. Mori and T. Itoh, "Distributed amplifier with CRLH-transmission line leaky wave antenna," *Proc. 38th Eur. Microw. Conf.*, Amsterdam, The Netherlands, October 2008, pp. 686–689.

139. J. Mata-Contreras, C. Camacho-Penalosa, and T. M. Martin-Guerrero, "Diplexing distributed amplifier with improved isolation," *Electron. Lett.*, vol. **47**, pp. 922–924, 2011.

140. J. Mata-Contreras, C. Camacho-Penalosa, and T. M. Martin-Guerrero, "Diplexing dual-gate FET distributed mixer," *Electron. Lett.*, vol. **47**, pp. 381–382, 2012.

141. C.-T. Michael-Wu, Y. Dong, J. S. Sun, and T. Itoh, "Ring-resonator-inspired power recycling scheme for gain-enhanced distributed amplifier-based CRLH-transmission line leaky wave antennas," *IEEE Trans. Microw. Theory Tech.*, vol. **60**, pp. 1027-1037, 2012.

142. J. Mata-Contreras, D. Palombini, T. M. Martín-Guerrero, A. Bentini, C. Camacho-Peñalosa, and E. Limiti, "Active GaN MMIC diplexer based on distributed amplification concept," *Microw. Opt. Technol. Lett.*, vol.**55**, pp. 1041–1045, 2013.

143. C. Rauscher, "Microwave active filters based on transversal and recursive principles," *IEEE Trans. Microw. Theory Tech.*, vol. **MTT-33**, pp. 1350–1360, 1985.

144. O. García-Pérez, A. García-Lampérez, V. González-Posadas, M. Salazar-Palma, and D. Segovia-Vargas, "Dual-band recursive active filters with composite right/left-handed transmission lines," *IEEE Trans. Microw. Theory Tech.*, vol. **57**, pp. 1180–1187, 2009.

145. L. Billonnet, B. Jarry, and P. Guillon, "Stability diagnosis of microwave recursive structures using the NDF methodology," *IEEE MTT-S Int. Microw. Symp. Dig.*, Orlando, FL, May 1995, vol. **3**, pp. 1419–1422.

146. O. García-Pérez, L. E. García-Muñoz, D. Segovia-Vargas, and V. González-posadas, "Multiple order dual-band active ring filters with composite right/left-handed cells," *Prog. Electromag. Res. (PIER)*, vol. **104**, pp. 201–219, 2010.

147. D. Segovia-Vargas, O. García-Pérez, V. González-Posadas, and F. Aznar-Ballesta, "Dual-band tunable recursive active filter," *IEEE Microw. Wireless Compon. Lett.*, vol. **21**, pp. 92–94, 2011.

148. M. Schüßler, C. Mandel, M. Puentes, and R. Jakoby, "Metamaterial inspired microwave sensors," *IEEE Microw. Mag.*, vol. **13**, pp. 57–67, 2012.

149. M. Puentes, B. Stelling, M. Schüßler, A. Penirschke, and R. Jakoby, "Planar sensor for permittivity and velocity detection based on metamaterial transmission line resonator," *Proc. 39th Eur. Microw. Conf.*, Rome, Italy, 2009, pp. 57–60.

150. C. Damm, M. Schüßler, M. Puentes, H. Maune, M. Maasch, and R. Jakoby, "Artificial transmission lines for high sensitive microwave sensors," *Proc. IEEE Sens. Conf.*, Christchurch, New Zealand, 2009, pp. 755–758.

151. C. Mandel, M. Schüßler, M. Maasch, and R. Jakoby, "A novel passive phase modulator based on LH delay lines for chipless microwave RFID applications," *Proc. IEEE MTT-S Int. Microw. Workshop Wireless Sens., Local Positioning RFID*, Cavtat, Croatia, 2009.

152. M. Schüßler, C. Mandel, M. Puentes, and R. Jakoby, "Capacitive level monitoring of layered fillings in vessels using composite right/left-handed transmission lines," *IEEE MTT-S Int. Microw. Symp. Dig.*, Baltimore, MD, June 2011.

153. J. Zhu and G. V. Eleftheriades, "Dual-band metamaterial-inspired small monopole antenna for WiFi applications," *Electron. Lett.*, vol. **45**, pp. 1104–1106, 2009.

154. F. J. Herraiz-Martínez, L. E. García-Muñoz, D. González-Ovejero, V. González-Posadas, and D. Segovia-Vargas, "Dual-frequency printed dipole loaded with split ring resonators," *IEEE Antennas Wireless Propag. Lett.* vol. **8**, pp. 137–140, 2009.

155. J. Montero-de-Paz, E. Ugarte-Muñoz, F. J. Herraiz-Martínez, V. González-Posadas, L. E. García-Muñoz, and D. Segovia-Vargas, "Multifrequency self-diplexed single patch antennas loaded with split ring resonators," *Prog. Electromag. Res.*, vol. **113**, pp. 47–66, 2011.

156. F. J. Herraiz-Martínez, F. Paredes, G. Zamora, F. Martín, and J. Bonache, "Dual-band printed dipole antenna loaded with open complementary split-ring resonators (OCSRRs) for wireless applications," *Microw. Opt. Technol. Lett.*, vol. **54**, pp. 1014–1017, 2012.

157. F. J. Herraiz-Martínez, G. Zamora, F. Paredes, F. Martín, and J. Bonache, "Multiband printed monopole antennas loaded with open complementary split ring resonators for PANs and WLANs," *IEEE Antennas Wireless Propag. Lett.*, vol. **10**, pp. 1528–1531, 2011.

158. F. Paredes, G. Zamora, J. Bonache, and F. Martín, "Dual-band impedance matching networks based on split ring resonators for applications in radiofrequency identification (RFID)," *IEEE Trans. Microw. Theory Tech.*, vol. **58**, pp. 1159–1166, 2010.

159. F. Paredes, G. Zamora, F. J. Herraiz-Martínez, F. Martín, and J. Bonache, "Dual-band UHF-RFID tags based on meander line antennas loaded with spiral resonators," *IEEE Antennas Wireless Propag. Lett.*, vol. **10**, pp. 768–771, 2011.

160. F. Paredes, G. Zamora, F. J. Herraiz-Martínez, F. Martín, and J. Bonache, "Dual-band RFID tags based on folded dipole antennas loaded with spiral resonators," *IEEE Int. Workshop Antennas Technol. Small Antennas Unconven. Appl. (IWAT 2012)*, Tucson, AZ, March 2012.

161. J. Naqui, M. Durán-Sindreu, and F. Martín, "Novel sensors based on the symmetry properties of split ring resonators (SRRs)," *Sensors*, vol **11**, pp. 7545–7553, 2011.

162. J. Naqui, M. Durán-Sindreu, and F. Martín, "On the symmetry properties of coplanar waveguides loaded with symmetric resonators: analysis and potential applications," *IEEE MTT-S Int. Microw. Symp. Dig.*, Montreal, Canada, June 2012.

163. J. Naqui, A. Fernández-Prieto, M. Durán-Sindreu, F. Mesa, J. Martel, F. Medina, and F. Martín, "Common mode suppression in microstrip differential lines by means of complementary split ring resonators: theory and applications," *IEEE Trans. Microw. Theory Tech.*, vol. **60**, pp. 3023–3034, 2012.

164. S. Preradovic, N. C. Karmakar, "Chipless RFID: bar code of the future," *IEEE Microw. Mag.*, vol. **11**, pp. 87–97, 2010.

165. S. Preradovic, I. Balbin, N. C. Karmakar, and G. F. Swiegers, "Multiresonator-based chipless RFID system for low-cost item tracking," *IEEE Trans. Microw. Theory Tech.*, vol. **57**, pp. 1411–1419, 2009.

166. T. Driscoll, G. O. Andreev, D. N. Basov, S. Palit, S. Y. Cho, N. M. Jokerst, and D. R. Smith, "Tuned permeability in terahertz split ring resonators for devices and sensors," *Appl. Phys. Lett.*, vol. **91**, paper 062511, 2007.

167. H.-J. Lee and J.-G. Yook, "Biosensing using split-ring resonators at microwave regime," *Appl. Phys. Lett.*, vol. **92**, paper 254103, 2008.

168. R. Melik, E. Unal, N. K. Perkgoz, C. Puttlitz, and H. V. Demir, "Metamaterial-based wireless strain sensors," *Appl. Phys. Lett.*, vol. **95**, paper 011106, 2009.

169. E. Cubukcu, S. Zhang, Y. S. Park, G. Bartal, and X. Zhang, "Split ring resonator sensors for infrared detection of single molecular monolayers," *Appl. Phys. Lett.*, vol. **95**, paper 043113, 2009.

170. X.-J. He, Y. Wang, J.-M. Wang, and T.-L. Gui, "Thin film sensor based tip-shaped splits ring resonator metamaterial for microwave applications," *Microsyst. Technol.*, vol. **16**, pp. 1735–1739, 2010.

171. E. Ekmekci and G. Turhan-Sayan, "Metamaterial sensor applications based on broadside-coupled SRR and V-shaped resonator structures," *Proc. Int. Symp. Antennas Propag.*, Jeju, South Korea, 2011, pp. 1170–1172.

172. M. Puentes, C. Weiss, M. Schüßler, and R. Jakoby, "Sensor array based on split ring resonators for analysis of organic tissues," *IEEE MTT-S Int. Microw. Symp. Dig.*, Baltimore, MD, June 2011.

173. C. Mandel, B. Kubina, M. Schüßler, and R. Jakoby, "Passive chipless wireless sensor for two-dimensional displacement measurement," *Proc. 41st Eur. Microw. Conf.*, Manchester, UK, 2011, pp. 79–82.

174. J. Naqui, M. Durán-Sindreu, and F. Martín, "Alignment and position sensors based on split ring resonators," *Sensors*, vol. **12**, pp. 11790–11797, 2012.

175. J. Naqui, M. Durán-Sindreu, and F. Martín, "Transmission lines loaded with bisymmetric resonators and applications," *Proc. IEEE MTT-S Int. Microw. Symp.*, Seattle, WA, June 2013.

176. A. Karami-Horestani, C. Fumeaux, S. F. Al-Sarawi, and D. Abbott, "Displacement sensor based on diamond-shaped tapered split ring resonator," *IEEE Sensors J.*, vol. **13**, pp. 1153–1160, 2013.

177. J. Naqui and F. Martín, "Transmission lines loaded with bisymmetric resonators and their application to angular displacement and velocity sensors," *IEEE Trans. Microw. Theory Tech.*, vol. **61**, pp. 4700–4713, 2013.

178. J. Naqui and F. Martín, "Angular displacement and velocity sensors based on electric-LC (ELC) loaded microstrip lines," *IEEE Sens. J.*, vol. **14**, pp. 939–940, 2014.

179. J. Naqui, M. Durán-Sindreu, and F. Martín, "Strategies for the implementation of sensors and RF barcodes based on transmission lines loaded with symmetric resonators," *21st Int. Conf. Appl. Electromag. Comm. (ICECom 2013)*, Dubrovnic, Croatia, October 2013.